

DIPLOMARBEIT

Numerical Analysis of Optical Multi-Core Waveguides

ausgeführt am
Institut für Nachrichtentechnik und Hochfrequenztechnik der
Technischen Universität Wien
von

Jörg Reitterer

Birkengasse 29
2384 Breitenfurt

Matrikelnummer: 0425645

Wien, im Juni 2010

Supervisors: Prof. Dr. Walter R. Leeb
Dipl.-Ing. Gerhard Schmid

Abstract

This diploma thesis investigates light propagation in optical waveguides which are used in opto-electronic printed circuit boards. In the boards under investigation, optical multi-core waveguides are used in order to increase the laser-to-waveguide and waveguide-to-photodiode misalignment tolerance. The individual cores have an approximately Gaussian refractive index profile due to the manufacturing process. In this work different characteristics of such multi-core waveguides are investigated. The main parameter of interest is the so-called throughput, which is defined as the ratio of waveguide output power to input power.

Due to the complexity of the multi-core waveguide structures, numerical analysis methods have to be used. The major part of this thesis was to develop a computer program which is capable of simulating light propagation in arbitrary waveguide structures. A software suite called BEAMLAB has been developed, which implements a *Beam Propagation Method*, a waveguide eigenmode solver, as well as the novel *Eigenmode Decomposition Method* using the high-level programming language MATLAB.

The throughput of different lateral and angular laser misalignments, as well as the throughput of different laser modes is computed. Simulations have shown that the average throughput of a multi-core waveguide with a stochastically modelled lateral laser misalignment is between 20% and 30%, which is only 10% to 15% larger than the average throughput of a single-core waveguide. Angular laser misalignments can also significantly reduce the throughput. The angle between the waveguide axis and the emitted laser beam should not be larger than 5° .

Multi-core structures, which are not invariant with respect to the propagation direction, are also investigated in this work. Such structures include bent waveguides, splitters, Mach-Zehnder interferometers, tapered waveguides, as well as waveguides crossing each other. Simulations have shown that bent waveguides should not have a bend angle larger than 5° and that the crosstalk between multi-core waveguides crossing each other is negligible. Splitters, Mach-Zehnder interferometers, and tapered multi-core waveguides are difficult to implement using multi-core waveguides due to the large number of waveguide eigenmodes.

It has also been shown that the throughput of multi-core waveguides can be influenced by applying pressure onto the waveguide. The pressure applied causes a deformation which induces additional losses and hence, reduces the photocurrent.

There certainly is potential for optimization of the multi-core waveguides investigated in this work. By adjusting parameters like the refractive index difference between waveguide core and cladding or number and spatial placement of the cores, the throughput could be increased.

Zusammenfassung

Diese Diplomarbeit beschäftigt sich mit der Ausbreitung von Licht in optischen Wellenleitern, welche in opto-elektronischen Leiterplatten zum Einsatz kommen. In diesen Leiterplatten werden optische Multi-Kern Wellenleiter verwendet um die Fehljustierungstoleranz von Laser zu Wellenleiter, sowie von Wellenleiter zu Photodiode, zu erhöhen. Die einzelnen Kerne haben ein annähernd gaußförmiges Brechungsindexprofil. In dieser Arbeit werden diverse Charakteristiken dieser Wellenleiter untersucht. Der wichtigste Parameter der Untersuchungen ist der sogenannte Durchsatz, welcher als Verhältnis von Ausgangsleistung zu Eingangsleistung definiert ist.

Aufgrund der Komplexität der Multi-Kern Wellenleiterstrukturen müssen numerische Berechnungsmethoden verwendet werden. Der Großteil dieser Arbeit ist der Entwicklung einer Computer Software gewidmet, welche es ermöglicht, die Ausbreitung von Licht in beliebigen Wellenleiterstrukturen zu simulieren. Im Rahmen dieser Arbeit wurde die Software BEAMLAB entwickelt, welche eine *Beam Propagation Method*, ein Modul zur Berechnung der Eigenmoden von Wellenleitern, sowie die neue *Eigenmode Decomposition Method* in der Programmiersprache MATLAB implementiert.

Mit Hilfe von Simulationen wird der Durchsatz bei unterschiedlichen lateralen und angularen Fehlpositionierungen des Lasers ermittelt. Weiters wird der Durchsatz diverser Lasermoden berechnet. Es wird gezeigt, dass der durchschnittliche Durchsatz eines Multi-Kern Wellenleiters bei stochastischer Modellierung der lateraler Fehlpositionierung des Lasers zwischen 20% und 30% beträgt. Dies ist lediglich 10% bis 15% mehr als der durchschnittliche Durchsatz eines Einzel-Kern Wellenleiters. Eine angulare Fehlpositionierung des Lasers kann den Durchsatz ebenfalls signifikant verringern. Der Winkel zwischen der Achse des Wellenleiters und dem emittierten Laserstrahl sollte nicht größer als 5° sein.

Multi-Kern Strukturen, welche nicht invariant in Ausbreitungsrichtung sind, werden ebenfalls untersucht. Derartige Strukturen sind z.B. gebogene Wellenleiter, Splitter, Mach-Zehnder Interferometer, Einzel-Kern Wellenleiter mit Multi-Kern Taper, sowie Wellenleiter, welche sich gegenseitig kreuzen. Simulationen haben gezeigt, dass der maximal zulässige Biegewinkel von Multi-Kern Wellenleitern 5° beträgt. Das Übersprechen zwischen Multi-Kernwellenleitern, welche sich gegenseitig kreuzen, ist vernachlässigbar. Splitter, Mach-Zehnder Interferometer sowie Einzel-Kern Wellenleiter mit Multi-Kern Taper sind aufgrund der hohen Anzahl an Eigenmoden der Multi-Kern Wellenleiter schwierig zu implementieren.

Weiters wird der Einfluss einer Deformierung, welche entsteht wenn Druck auf den Multi-Kern Wellenleiter ausgeübt wird, auf den Durchsatz untersucht. Die Deformierung führt zu erhöhten Verlusten, welche den Durchsatz und somit den Photostrom verringern.

Die Simulationsergebnisse legen die Vermutung nahe, dass die in dieser Arbeit untersuchten Multi-Kern Wellenleiter Potenzial für Optimierungen aufweisen. Durch Modifikation von Parametern wie Brechungsindexunterschied zwischen Wellenleiterkern und -mantel sowie Anzahl und räumliche Platzierung der individuellen Kerne, ließe sich der Durchsatz erhöhen.

Acknowledgments

First of all, I want to thank Prof. Walter R. Leeb for many hours of weekly discussions which always helped to push this thesis in the right direction.

Deep appreciation goes to Gerhard Schmid for many helpful hints and for helping to improve this text.

Finally, and most importantly, I want to thank my mother and my father, for always being there and making it possible to fulfill all my study and non-study related desires.

Contents

1	Motivation	1
1.1	Opto-Electronic Printed Circuit Boards	1
1.2	The Software BEAMLAB	2
1.2.1	Advantages Over Existing Commercial Software	3
1.2.2	List of Features	4
2	Simulation Models	5
2.1	Introduction and Outline	5
2.2	Waveguides	5
2.2.1	Multi-Core Waveguides	5
2.2.2	Single-Core Waveguides	6
2.3	Laser Output Fields	8
2.3.1	Transversal VCSEL Modes	8
2.3.2	Gaussian LP ₀₁ Mode	8
3	Finite-Difference Beam Propagation Method	11
3.1	Introduction and Outline	11
3.2	Two-Dimensional Semivectorial Analysis	13
3.2.1	Wave Equation	13
3.2.2	FD-BPM Formulation	16
3.2.3	Non-Equidistant Discretization Scheme	18
3.2.4	Transparent Boundary Conditions	19
3.2.5	Implementation in MATLAB	20
3.3	Three-Dimensional Semivectorial Analysis	21
3.3.1	First ADI Step	24
3.3.2	Second ADI Step	25
3.3.3	Computational Complexity	25
3.4	Accuracy Estimation	25
3.4.1	Fresnel Approximation	25
3.4.2	Spatial Sampling Constraints	26
3.4.3	Boundary Reflections	28
3.5	Imaginary Distance Beam Propagation Method	28
4	Eigenmode Decomposition Method	31
4.1	Introduction and Outline	31
4.2	Waveguide Throughput	31
4.3	Waveguide Eigenmodes	32
4.3.1	Eigenmode Equation	33
4.3.2	Rotation of Eigenmodes	33
4.4	Linear Vector Spaces and Orthonormal Bases	34
4.5	Hilbert Space of Eigenmodes	35

4.6	Examples	36
4.6.1	Single-Mode Waveguide	36
4.6.2	Multi-Mode Waveguide	38
5	Throughput of Multi-Core Waveguides	43
5.1	Introduction and Outline	43
5.2	Lateral Laser Misalignment	43
5.2.1	Deterministic Lateral Misalignment	43
5.2.2	Stochastic Lateral Misalignment	44
5.3	Angular Laser Misalignment	48
5.4	Dependence of Throughput on Core Refractive Index	51
5.5	Throughput of Different VCSEL Modes	54
6	Complex Multi-Core Structures	55
6.1	Introduction and Outline	55
6.2	Bent Multi-Core Waveguides	55
6.3	Multi-Core Waveguide Splitters	59
6.4	Crossing Multi-Core Waveguides	62
6.5	Multi-Core Mach-Zehnder Interferometers	65
6.6	Multi-Core Taper Waveguides	68
6.7	Deformation of Multi-Core Waveguides	72
6.8	Periodic Refractive Index Variation in Propagation Direction	76
7	Conclusions and Outlook	78
A	Multi-Core Waveguide Eigenmodes	80
B	VCSEL Eigenmodes	85
C	BeamLab Examples	86
C.1	Beam Propagation Computation Using BEAMLABBPM	86
C.2	Eigenmode Computation Using BEAMLABEIG	89
C.3	Throughput Computation Using BEAMLABEDM	92

List of Tables

2.1	Locations of the centers of the waveguide cores.	6
2.2	Default values of the multi-core waveguide simulation model parameters. . .	6
2.3	Mode radii $w_0(l, p)$ of different Laguerre Gaussian modes LP_{01} MMSE-matched to the corresponding Bessel modes from VISTAS.	9
4.1	Numerical values of inner products $\langle \Phi_{\text{in}}, V_1 \rangle$ and overlap integrals $\mathcal{O}(\Phi_{\text{in}}, V_1)$ with the only eigenmode V_1 , as well as numerical throughput values $\eta(\Phi_{\text{in}})$ of the fields $\Phi_{\text{in}} = \Phi_0$, $\Phi_{\text{in}} = \Phi_{\mathcal{H}}$, and $\Phi_{\text{in}} = \Phi_{\mathcal{H}^\perp}$	37
4.2	Numerical values of inner products $\langle \Phi_{\text{in}}, V_n \rangle$ and overlap integrals $\mathcal{O}(\Phi_{\text{in}}, V_n)$ with all $N = 6$ eigenmodes V_1, \dots, V_6 , as well as numerical throughput values $\eta(\Phi_{\text{in}})$ of the fields $\Phi_{\text{in}} = \Phi_0$, $\Phi_{\text{in}} = \Phi_{\mathcal{H}}$, and $\Phi_{\text{in}} = \Phi_{\mathcal{H}^\perp}$	42

List of Figures

1.1	Schematic of an opto-electronic printed circuit board.	2
1.2	Schematic of the refractive index profile $n(x, y)$ of (a) a single-core waveguide and (b) a multi-core waveguide.	3
1.3	BEAMLAB logo.	3
2.1	Refractive index profile $n(x, y)$ of the multi-core waveguide model.	7
2.2	Normalized radial intensity distributions of some Laguerre Gaussian modes at $z = 0$	9
2.3	Definitions of the angles (a) θ_x and (b) θ_y with respect to the propagation direction z	10
3.1	The main principle of the Beam Propagation Method: The propagating field at $z + \Delta z$ is calculated from the previous field at z	12
3.2	Lateral spatial discretization of the analysis area. Here, equidistant discretization is shown, but non-equidistant discretization is also possible in x and y direction.	12
3.3	One-dimensional non-equidistant discretization.	18
3.4	Location of the nodes $p = 0$ and $p = M_x + 1$ outside of the actual analysis area.	19
3.5	Two-dimensional non-equidistant discretization.	22
3.6	Relation between wave number k , z -directed wave number β (propagation constant), x -directed wave number k_x , and propagation angle θ_x with respect to the z direction in the plane $y = 0$	26
3.7	$\Re\{\Phi_0(x, y)\}$ for different values of θ_x . The spatial period with respect to x is $1/f_x = \lambda/\sin(\theta_x)$	27
3.8	Setpoint angles θ_x vs. actual angles $\hat{\theta}_x$ for different oversampling factors γ	27
3.9	Intensity I in the plane $y = 0$ of an incident Gaussian beam ($\theta_x = -10^\circ$, $w_0 = 15 \mu\text{m}$) and the reflected beam.	28
3.10	Power P in the whole transversal simulation region vs. propagation distance z	28
3.11	Intensity I in the plane $y = 0$ vs. propagation step number n for a step-index circular waveguide using the Imaginary Distance BPM. The input field is a plane wave, i.e. $\Phi_0(x, y) = A_0 = 1$, the initial value of the normalized propagation constant is $B_0 = 0$, and the propagation step size is $\Delta z = 10 \mu\text{m}$	29
3.12	Calculated value of the normalized propagation constant B of the fundamental mode at each iteration for the starting conditions $\Phi_0(x, y) = A_0 = 1$ and $B_0 = 0$. The propagation step size is $\Delta z = 10 \mu\text{m}$	30
4.1	Schematic representation of the <i>spatial transient</i> and the <i>spatial steady state</i>	32
4.2	Schematic representation of the decomposition $\Phi_0 = \Phi_{\mathcal{H}} + \Phi_{\mathcal{H}^\perp}$	36

4.3	Illustration of the decomposition $\Phi_0 = \Phi_{\mathcal{H}} + \Phi_{\mathcal{H}^\perp}$ for a single-mode waveguide with core radius $a = 4.5 \mu\text{m}$ and a Gaussian input field with lateral offset $x_{\text{offset}} = 2.5 \mu\text{m}$. The abscissas and ordinates are all in μm and show x and y coordinates, respectively.	38
4.4	Intensity I in the plane $y = 0$ of the beams propagating in a single-mode waveguide for the input fields Φ_0 , $\Phi_{\mathcal{H}}$, and $\Phi_{\mathcal{H}^\perp}$. Here, $x_{\text{offset}} = 2.5 \mu\text{m}$. . .	39
4.5	Normalized power P in a circular area with radius $20 \mu\text{m}$ vs. propagation distance z for the input fields Φ_0 , $\Phi_{\mathcal{H}}$, and $\Phi_{\mathcal{H}^\perp}$ and a single-mode waveguide. . .	40
4.6	The dark blue bar represents the power $\mathcal{O}(\Phi_z, V_1)$ carried in the only waveguide eigenmode V_1 at propagation distance z . Since there is only $N = 1$ eigenmode, this is equal to the throughput, i.e. $\eta(\Phi_0) = \mathcal{O}(\Phi_0, V_n)$ due to Equation (4.27).	40
4.7	Illustration of the decomposition $\Phi_0 = \Phi_{\mathcal{H}} + \Phi_{\mathcal{H}^\perp}$ for a multi-mode waveguide with core radius $a = 4.5 \mu\text{m}$ and a Gaussian input field with lateral offset $x_{\text{offset}} = 4.5 \mu\text{m}$. The abscissas and ordinates are all in μm and show x and y coordinates, respectively.	40
4.8	Intensity I in the plane $y = 0$ of the beams propagating in a multi-mode waveguide for the input fields Φ_0 , $\Phi_{\mathcal{H}}$, and $\Phi_{\mathcal{H}^\perp}$. Here, $x_{\text{offset}} = 2.5 \mu\text{m}$. . .	41
4.9	Normalized power P in a circular area with radius $20 \mu\text{m}$ vs. propagation distance z for the input fields Φ_0 , $\Phi_{\mathcal{H}}$, and $\Phi_{\mathcal{H}^\perp}$ and a multi-mode waveguide. . .	42
4.10	Each color represents the power $\mathcal{O}(\Phi_z, V_n)$ carried in one of the $N = 6$ waveguide eigenmodes V_n at propagation distance z . The sum of these powers is the throughput, i.e. $\eta(\Phi_0) = \sum_{n=1}^N \mathcal{O}(\Phi_0, V_n)$ due to Equation (4.27). . . .	42
5.1	Definition of lateral offsets x_{offset} and y_{offset} with respect to the x and y direction, respectively.	44
5.2	Intensity I in the plane $y = 0$ of beams propagating in a multi-core waveguide for different values lateral laser misalignment x_{offset}	45
5.3	Normalized power $P(z)/P(0)$ in a circular area of radius $50 \mu\text{m}$ vs. propagation distance z for different values of lateral laser misalignment x_{offset} . . .	46
5.4	Throughput η vs. lateral laser misalignment in x direction ($y_{\text{offset}} = 0$) and in y direction ($x_{\text{offset}} = 0$).	46
5.5	Throughput η vs. lateral laser misalignment x_{offset} and y_{offset} in <i>both</i> lateral directions x and y for a multi-core waveguide.	46
5.6	Throughput η vs. lateral laser misalignment x_{offset} and y_{offset} in <i>both</i> lateral directions x and y for a single-core waveguide.	47
5.7	Average throughput $\bar{\eta}$ vs. standard deviation σ of the jointly Gaussian random variable (X, Y)	48
5.8	Definition of angular offset θ_x with respect to the z direction in the plane $y = 0$	48
5.9	Intensity I in the plane $y = 0$ of beams propagating in a multi-core waveguide with $x_{\text{offset}} = 0 \mu\text{m}$ and different values of the misalignment angle θ_x . (c) and (d) show details of (a) and (b), respectively.	49
5.10	Normalized power $P(z)/P(0)$ in a circular area of diameter $50 \mu\text{m}$ vs. propagation distance z for different values of angular laser misalignment θ_x . . .	50
5.11	Throughput η vs. angular laser misalignment θ_x	50
5.12	Refractive index profile of the multi-core waveguide for different values of the relative refractive index difference Δ	51
5.13	Intensity I in the plane $y = 0$ of beams propagating in a multi-core waveguide for different values of the refractive index difference Δ	52

5.14	Normalized power $P(z)/P(0)$ in a circular area of diameter $50\ \mu\text{m}$ vs. propagation distance z for different values of the refractive index difference Δ	53
5.15	Throughput η vs. relative refractive index difference Δ for different lateral laser misalignments x_{offset} and y_{offset}	53
5.16	Number of multi-core waveguide eigenmodes N vs. relative refractive index difference Δ	53
5.17	Throughput η of different Laguerre Gaussian VCSEL modes.	54
6.1	Definition of the bend angle α_B	56
6.2	Three-dimensional refractive index profile of a bent multi-core waveguide. Here, the bend angle is $\alpha_B = 2^\circ$. The surface shows all points with equal refractive index $n = n_2 + (n_1 - n_2)/e = 1.5161$	56
6.3	Intensity I in the plane $y = 0$ of beams propagating in bent multi-core waveguides for different values of the bend angle α_B	58
6.4	Throughput η of a bent multi-core waveguide vs. bend angle α_B . Here, the lateral laser misalignment is $x_{\text{offset}} = y_{\text{offset}} = 0\ \mu\text{m}$	59
6.5	Three-dimensional refractive index profile of a multi-core waveguide splitter. The surface shows all points with equal refractive index $n = n_2 + (n_1 - n_2)/e = 1.5161$	59
6.6	Intensity I in the plane $y = 0$ of beams propagating in a multi-core waveguide splitter for different values of the lateral laser misalignment x_{offset}	61
6.7	Throughputs η_1 and η_2 from the input at $z = 0$ to the upper and lower splitter arm, respectively, as a function of the lateral laser misalignment x_{offset} . $\eta_1 + \eta_2$ is the total throughput.	62
6.8	Three-dimensional refractive index profile of a two multi-core waveguides crossing each other. The surface shows all points with equal refractive index $n = n_2 + (n_1 - n_2)/e = 1.5161$	62
6.9	Intensity I in the plane $y = 0$ of beams propagating in crossing multi-core waveguides for different values of the lateral laser misalignment x_{offset}	64
6.10	Crosstalk $\chi = \eta_1$ between two multi-core waveguides crossing each other as a function of the lateral laser misalignment x_{offset} . η_2 is the throughput from the top left input to the bottom right output in Figure 6.9.	65
6.11	Three-dimensional refractive index profile of a multi-core Mach-Zehnder interferometer. The surface shows all points with equal refractive index $n = n_2 + (n_1 - n_2)/e = 1.5161$	65
6.12	Intensity I in the plane $y = 0$ of beams propagating in a multi-core Mach-Zehnder interferometer for different values of the lateral laser misalignment x_{offset}	67
6.13	Throughput η of a multi-core Mach-Zehnder interferometer vs. lateral laser misalignment x_{offset}	68
6.14	Three-dimensional refractive index profile of a single-core waveguide with a multi-core taper. Here, the taper length is $L_T = 3\ \text{mm}$. The surface shows all points with equal refractive index $n = n_2 + (n_1 - n_2)/e = 1.5161$	68
6.15	Intensity I in the plane $y = 0$ of beams propagating in a multi-core taper waveguide for different values of the taper length L_T and the lateral laser misalignment x_{offset}	70
6.16	Throughput η of a multi-core taper waveguide vs. lateral laser misalignment x_{offset} for different values of the taper length L_T	71
6.17	Comparison of the throughputs η of a multi-core taper waveguide, a single-core waveguide with no taper, and a multi-core waveguide with no taper.	71

6.18	Schematic representation of the waveguide deformation model. The pressure p is applied onto the waveguide which causes a reduction of $w_{0,n,y}$ and changes the center of the waveguide to $(\tilde{x}_k, \tilde{y}_k)$	72
6.19	Three-dimensional refractive index profile of a multi-core waveguide deformed by applying pressure onto it (compression factor $\zeta = 4$). The surface shows all points with equal refractive index $n = n_2 + (n_1 - n_2)/e = 1.5161$	73
6.20	Intensity I in (a) the plane $y = 0$ and (b) the plane $x = 0$ of beams propagating in the deformed multi-core waveguide from Figure 6.19. The solid white lines indicate the locations of the cores of the <i>undeformed</i> waveguide.	74
6.21	Throughput $\sum_{n=1}^N \mathcal{O}(\Phi_z, V_n)$ for different values of the waveguide compression factor ζ and lateral offset x_{offset} . Each color represents the power $\mathcal{O}(\Phi_z, V_n)$ carried in one of the waveguide eigenmodes V_n at propagation distance z	75
6.22	Simulated relative photocurrent change $\Delta I_{\text{PD,rel}}$ vs. waveguide compression factor ζ	76
6.23	Periodic refractive index profile $n(x, y, z)$ (a) in the plane $y = 0$ and (b) in the plane $x = y = 0$. \bar{n}_1 is the average refractive index with respect to the z direction.	77
6.24	Throughput of a multi-core waveguide with periodic refractive index variation according to the model from Equations (6.7)–(6.8) (“ n periodic”). “ \bar{n}_1 ” designates that the waveguide is invariant with respect to the z direction according to the model from Equations (6.10)–(6.11).	77
A.1	Dispersion relation $B(V)$ of the multi-core waveguide. The dashed vertical line indicates the normalized frequency V corresponding to the wavelength $\lambda = 850$ nm.	80
A.2	Number of eigenmodes N vs. normalized frequency V of the multi-core waveguide. The dashed vertical line indicates the normalized frequency V corresponding to the wavelength $\lambda = 850$ nm.	81
A.3	Eigenmodes 1–18 of the multi-core waveguide. The abscissas and ordinates are all in μm and show x and y coordinates, respectively.	82
A.4	Eigenmodes 19–36 of the multi-core waveguide. The abscissas and ordinates are all in μm and show x and y coordinates, respectively.	83
A.5	Eigenmodes 37–51 of the multi-core waveguide. The abscissas and ordinates are all in μm and show x and y coordinates, respectively.	84
B.1	VCSEL eigenmodes from Equation (2.6). The abscissas and ordinates are all in μm and show x and y coordinates, respectively.	85
C.1	First output plot of the BEAMLABBPM example showing the intensity I in the plane $y = 0$ of a beam propagating in a circular step-index waveguide.	88
C.2	Second output plot of the BEAMLABBPM example showing the power in a circular area of radius $20 \mu\text{m}$ vs. propagation distance z	88
C.3	First output plot of the BEAMLABEIG example showing the six eigenmodes V_1, \dots, V_6 of the circular step-index waveguides at $V = 5$. The abscissas and ordinates are all in μm and show x and y coordinates, respectively.	91
C.4	Second output plot of the BEAMLABEIG example showing the dispersion relation $B(V)$ of a circular step-index waveguide.	91

Nomenclature

$\langle \Phi_1, \Phi_2 \rangle$	Inner product of two functions $\Phi_1(x, y)$ and $\Phi_2(x, y)$
$\ \Phi\ $	Norm of a function $\Phi(x, y)$
a	Waveguide core radius
A_0	Beam amplitude
A_B	Waveguide bend offset
ABC	Absorbing Boundary Condition
ADI	Alternate Direction Implicit
α_B	Waveguide bend angle
B	Normalized propagation constant
\vec{B}	Magnetic flux density
β	Propagation constant
BPM	Beam Propagation Method
CAD	Computer Aided Design
χ	Crosstalk
CPU	Central Processing Unit
\vec{D}	Electric flux density
Δ	Relative refractive index difference
$\Delta I_{PD,rel}$	Relative photocurrent change
Δz	Propagation step distance
\vec{E}	Electric field
EDM	Eigenmode Decomposition Method
ε	Permittivity
ε_r	Relative permittivity
η	Throughput
$\bar{\eta}$	Average throughput

f_s	Spatial sampling frequency
$f_{X,Y}$	Probability density function of the 2-D random variable (X, Y)
FD	Finite Difference
FE	Finite Element
FFT	Fast Fourier Transform
γ	Spatial oversampling factor
\mathcal{H}	Hilbert space of waveguide eigenmodes
\mathcal{H}^\perp	Orthogonal complement of Hilbert space of waveguide eigenmodes
\vec{H}	Magnetic field
I	Intensity
ID	Imaginary Distance
\vec{J}	Current density
k_0	Wave number in a vacuum
L_B	Waveguide bend length
$L_{p-1}^{(l)}$	Generalized Laguerre polynomial of kind l and order $p - 1$
L_T	Waveguide taper length
Λ	Refractive index period with respect to the propagation direction
λ	Wavelength
λ_0	Wavelength in a vacuum
M_x	Number of mesh grid points in the x direction
M_y	Number of mesh grid points in the y direction
MMSE	Minimum Mean Square Error
μ	Permeability
μ_r	Relative permeability
μ_X	Mean of the random variable X
N	Number of waveguide eigenmodes
n	Refractive index
\bar{n}	Average refractive index
n_1	Refractive index of waveguide core
n_2	Refractive index of waveguide cladding
n_{eff}	Effective refractive index

NA	Numerical aperture
$\mathcal{O}(\Phi_1, \Phi_2)$	Overlap integral of two functions $\Phi_1(x, y)$ and $\Phi_2(x, y)$
ω	Angular frequency
P	Power
p	Pressure
PCB	Printed Circuit Board
Φ_0	Input field under investigation
$\Phi_{\mathcal{H}}$	Component of Φ_0 in Hilbert space \mathcal{H}
$\Phi_{\mathcal{H}^\perp}$	Component of Φ_0 in \mathcal{H}^\perp , the orthogonal complement of Hilbert space \mathcal{H}
Φ_{in}	Input field of actual BPM simulation
Φ_{lp}	Laguerre Gaussian mode LP_{lp}
Φ_{out}	Output field
R	Curvature of the beam wave front
ρ	Density of volume charge
$\rho_{X,Y}$	Correlation coefficient of the random variables X and Y
σ_X^2	Variance of the random variable X
TBC	Transparent Boundary Condition
θ_x	Angular laser misalignment with respect to the z direction in the plane $y = 0$
θ_y	Angular laser misalignment with respect to the z direction in the plane $x = 0$
TPA	Two Photon Absorption
V	Normalized frequency
V_n	n -th waveguide eigenmode number
VCSEL	Vertical Cavity Surface Emitting Laser
VISTAS	VCSEL Integrated Spatio Temporal Device Simulator
w	Mode field radius
w_0	Radius of the beam waist
$w_{0,n}$	Core radius of a waveguide with Gaussian refractive index profile
x, y	Lateral coordinates
x_{offset}	Lateral laser misalignment in x direction
ξ	Gouy phase
y_{offset}	Lateral laser misalignment in y direction
z	Longitudinal coordinate, propagation direction
z_0	Confocal parameter
ζ	Waveguide compression factor

Chapter 1

Motivation

1.1 Opto-Electronic Printed Circuit Boards

Conventional electronic printed circuit boards (PCB) use copper tracks to transport data from an information source to an information sink within the board. They have the advantages of being inexpensive and highly reliable but generally have a relatively limited bandwidth.

Optical data transmission uses *optical waveguides* which have many advantages over their electronic AI counterparts such as:

- larger bandwidth,
- lower losses,
- larger possible transmission distances,
- no electromagnetic interference, and
- lower power consumption above a certain threshold of the bandwidth-distance product.

On the other hand, optical data transmission has the disadvantage of requiring additional electrical-to-optical conversion at the transmitter and optical-to-electrical conversion at the receiver. Furthermore, the tight alignment tolerances of laser and waveguide, as well as waveguide and photodiode, make optical data transmission systems generally more expensive.

With today's ever increasing demands on bandwidth it becomes increasingly difficult to transmit high data rates, even over the relatively short distances within printed circuit boards. In opto-electronic PCBs the copper tracks are replaced by optical waveguides in order to make use of the aforementioned advantages of optical data transmission. Above a certain threshold of the bandwidth-distance product, opto-electronic PCBs have a lower power consumption than pure electronic PCBs. The inherent immunity to electromagnetic interference and negligible crosstalk between adjacent waveguides are also important reasons for using optical waveguides in PCBs.

Figure 1.1 shows a schematic of an opto-electronic PCB. The light source is a vertical cavity surface emitting laser (VCSEL) and the light sink is a photo diode, both of which are mounted on top of the PCB. In order to optically connect VCSEL and photo diode, the whole PCB is covered with a polymer coating (ORMOCER[®] [1] cladding) where the actual waveguide is inscribed into. VCSEL and photo diode are electrically connected to PCB tracks by bond wires.

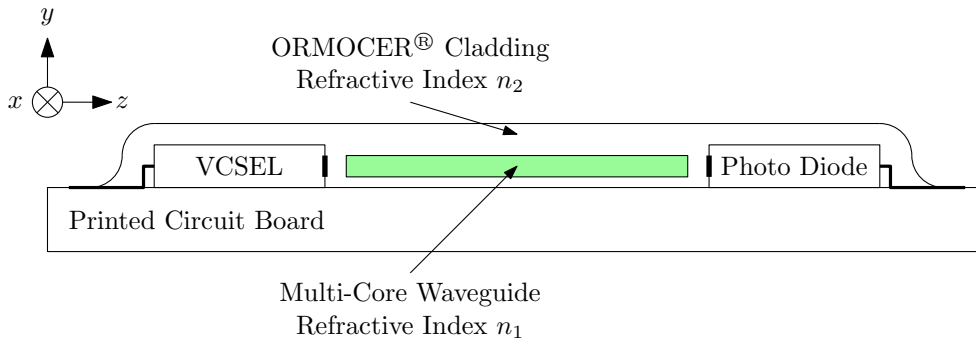


Figure 1.1: Schematic of an opto-electronic printed circuit board.

ORMOCER® Cladding Material. The ORMOCER® cladding material was developed at *Fraunhofer-Institut für Silicatforschung ISC* in Germany. It allows to laser-write waveguide cores into the cladding material using a non-linear optical process called two-photon absorption (TPA) [2]. This process requires very high intensities which can be created only by using pulsed femtosecond lasers. The TPA process slightly increases the refractive index of the ORMOCER® in the laser focus which allows virtually any three-dimensional waveguide structure to be written into the substrate. As already indicated in Figure 1.1, there is a small gap between the waveguide and the VCSEL/photo diode. This gap has a size of about $15 \mu\text{m}$ and is necessary because the waveguide cannot be written arbitrarily close to the opto-electronic devices without harming them.

Multi-Core Waveguide. Figures 1.2(a) and 1.2(b) and show the lateral refractive index profiles of a single-core waveguide and a multi-core waveguide, respectively¹. A single-core waveguide consists of a single core region which has a slightly larger refractive index than the surrounding cladding material while a multi-core waveguide has multiple core regions. In the context of opto-electronic PCBs, the reason to use such multi-core structures is to somewhat relax the constraints of perfectly aligning the VCSEL to the waveguide. Because of the much larger overall waveguide diameter a larger misalignment is tolerable. These multi-core waveguide structures do not show any advantage with respect to their “waveguiding properties” but rather are used as a necessity for coupling enough light power into the waveguide in order to enable a reliable data transmission. The actual refractive index profile of each core has a Gaussian shape which will be discussed in more detail in Section 2.2.

1.2 The Software BeamLab

The major part of this diploma thesis was to develop a software suite which is capable of simulating light propagation in arbitrary waveguide structures in order to analyze various properties of multi-core waveguides from Figure 1.2(b). This software called BEAMLAB [3] is a comprehensive set of simulation tools for photonic devices and optical waveguides written in MATLAB. It consists of three different modules:

- BEAMLABBPM implements a *Beam Propagation Method*,
- BEAMLABEIG implements a waveguide eigenmode solver, and
- BEAMLABEDM implements a novel *Eigenmode Decomposition Method*.

¹For simplicity the schematic in Figure 1.2 shows step-index waveguides. The actual refractive index profile of the waveguides investigated in this work will be discussed in 2.2.

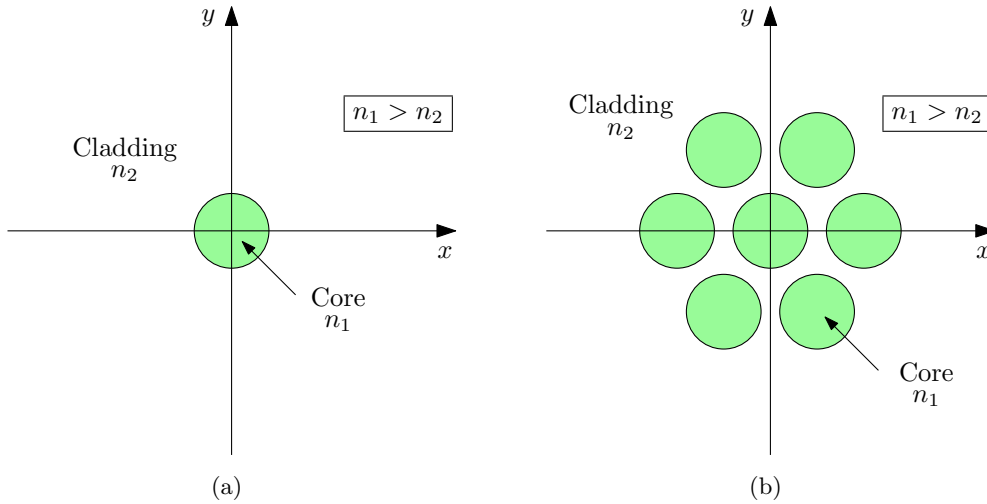


Figure 1.2: Schematic of the refractive index profile $n(x, y)$ of (a) a single-core waveguide and (b) a multi-core waveguide.



Figure 1.3: BEAMLAB logo.

Figure 1.3 shows the BEAMLAB logo.

1.2.1 Advantages Over Existing Commercial Software

Most of BEAMLAB’s advantages arise from the fact that it is implemented using the high-level programming language MATLAB.

Flexibility. In BEAMLAB all simulations models are “programmed” using MATLAB code (see Appendix C for some examples). Thus, virtually any waveguide models, i.e. spatially refractive index distributions, as well as simulation input fields can be realized. On the other hand, most commercially available software packages use some kind of graphical computer aided design (CAD) interface to “draw” waveguide geometries. This generally results in a better usability but also imposes some limitations on the models which actually can be realized. With BEAMLAB complex waveguide structures like the ones in Chapter 6 can be realized using only a few lines of MATLAB code.

Scalability. With BEAMLAB it is very easy to implement parameter sweeps of all kinds. For example, if one wants to analyze waveguide throughput vs. refractive index difference between waveguide core and cladding (see Section 5.4), just a single `for` loop in the MATLAB code is necessary. Furthermore the computations of such sweeps are very often independent of each other and can therefore be executed in parallel on multiple central processing unit (CPU) cores or even on multiple computers simply by using a `parfor` loop².

Further Advantages. Some further advantages inherent to MATLAB are

²These features require MATLAB’s *Parallel Computing Toolbox* and *Distributed Computing Server*, respectively.

- Platform independence (Windows, Linux, Mac OS X, Solaris are supported)
- Support of 32 and 64 bit platforms
- Extensive plotting options

1.2.2 List of Features

In the following the most important features provided by the three BEAMLAB modules are listed. In Chapters 3 and 4 all of these features will be discussed in more detail.

BeamLabBPM.

- Implements an Alternate Direction Implicit Finite Difference Beam Propagation Method (3D-ADI-FD-BPM) in MATLAB
- Semi-vectorial or scalar beam propagation analysis
- 3-D or 2-D analysis
- Transparent Boundary Conditions
- Non-equidistant or equidistant discretization in all three spatial directions
- Very high scalability of CPU and memory usage
- Video export of propagating fields
- Ultra-fast semi-vectorial or scalar eigenmode solver using the *Imaginary Distance Beam Propagation Method*

BeamLabEIG.

- Implements a waveguide eigenmode solver based on the Finite Difference method in MATLAB
- Semi-vectorial or scalar analysis
- Non-equidistant or equidistant discretization meshes

BeamLabEDM.

- Implements a novel Eigenmode Decomposition Method (see Chapter 4) in MATLAB
- Ultra-fast calculation of waveguide throughput for given input fields

Chapter 2

Simulation Models

2.1 Introduction and Outline

This chapter describes the simulation models of the waveguides, i.e. the spatial refractive index distributions, as well as the laser output fields which constitute the “input parameters” of the BEAMLAB simulations carried out in Chapters 4–6.

This chapter is organized as follows.

- In Section 2.2 the simulation model of the multi-core waveguides introduced in Chapter 1 are discussed in detail. Furthermore, the simulation model of single-core waveguides is presented which will be used in Chapters 5 and 6 to compare multi-core and single-core waveguides.
- In Section 2.3 the transversal modes of a VCSEL are presented. The most important Gaussian LP₀₁ mode is discussed in more detail.

2.2 Waveguides

2.2.1 Multi-Core Waveguides

The simulation model of multi-core waveguides used in opto-electronic PCBs is shown in Figure 2.1. It is matched to refractive index measurements carried out by *Fraunhofer-Institut für Silicatforschung ISC*. The waveguide consists of seven separate cores which are arranged in a hexagonal structure. The main parameters are given as follows.

- n_1 is the (maximum) core refractive index.
- n_2 is the cladding refractive index.
- $n_{c,xy}$ is the local minimum of the refractive index between two adjacent cores.
- r is the radius of the circle with center $x = y = 0$ on which all outer cores are located.
- $h = \sqrt{3}/2 \cdot r$ is the height of the hexagon and follows from simple geometrical considerations.
- $w_{0,n}$ is the radius¹ of a single core.

¹Here, the radius of a single core with a Gaussian profile is defined as the radius where the refractive index has decayed to the value $n = n_2 + (n_1 - n_2)/e$.

Table 2.1: Locations of the centers of the waveguide cores.

k	x_k	y_k
1	0	0
2	$-r$	0
3	$+r$	0
4	$-r/2$	$+h$
5	$+r/2$	$+h$
6	$-r/2$	$-h$
7	$+r/2$	$-h$

Table 2.2: Default values of the multi-core waveguide simulation model parameters.

Parameter	Default value
n_1	1.5180
n_2	1.5150
$n_{c,xy}$	1.5154
r	25 μm
$w_{0,n}$	7.6 μm

With these parameters the simulation model of the multi-core waveguide is given by

$$n(x, y) = n_2 + n_d \cdot f(x, y), \quad (2.1)$$

where

$$n_d = n_1 - n_2, \quad (2.2)$$

$$f(x, y) = \sum_{k=1}^K \exp \left[- \left(\frac{x - x_k}{w_{0,n}} \right)^2 - \left(\frac{y - y_k}{w_{0,n}} \right)^2 \right], \quad (2.3)$$

$$w_{0,n} = \frac{r}{2 \sqrt{\ln \left(\frac{2}{n_{c,xy}} \right)}}, \quad (2.4)$$

$$n_{c,xy} = n(r/2, 0). \quad (2.5)$$

Here, $f(x, y) \in [0, 1]$ in a very good approximation. Figure 2.1 shows this spatial refractive index distribution. The red dots show the centers of the cores which are located at the coordinates from Table 2.1. Evidently $K = 7$ for this multi-core waveguide structure.

Default Parameters. The numerical default values of the parameters used throughout this document—unless explicitly stated otherwise—are shown in Table 2.2. The value of $w_{0,n}$ follows directly from Equation (2.4).

2.2.2 Single-Core Waveguides

In Chapters 5 and 6 single-core waveguides are also investigated in order to compare their properties to multi-core waveguides. We will also use Equations (2.1), (2.2), and (2.3), only this time with $K = 1$ and $x_1 = y_1 = 0$. The same core radius $w_{0,n}$ (see footnote on page 5) will be used.

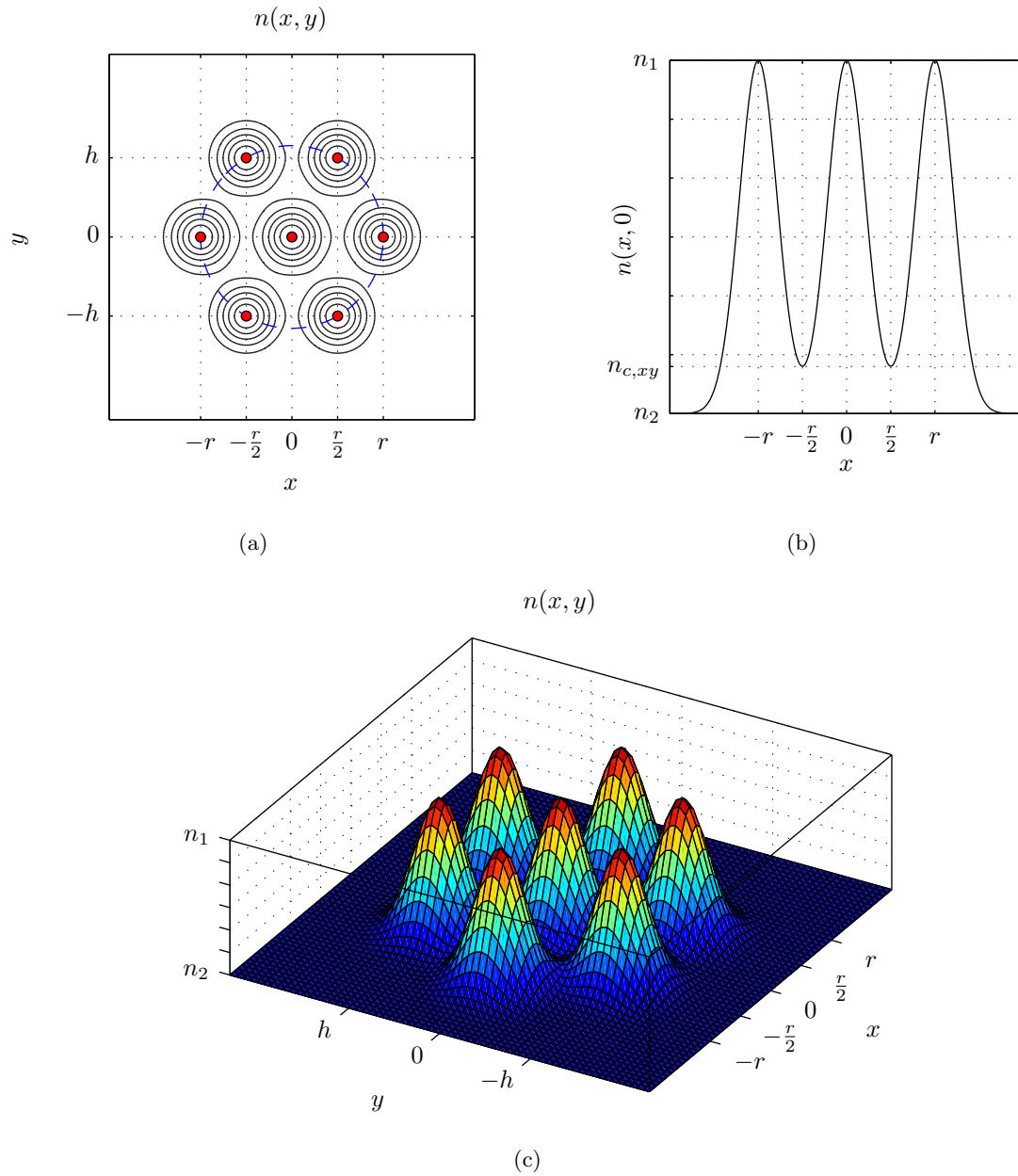


Figure 2.1: Refractive index profile $n(x, y)$ of the multi-core waveguide model.

2.3 Laser Output Fields

2.3.1 Transversal VCSEL Modes

In literature there exist two different models for the transversal modes of a VCSEL: *Bessel modes* [4], which are also the eigenmodes of step-index cylindrical waveguides, and *Laguerre Gaussian modes* [5, 6], which are the eigenmodes of graded-index circularly symmetric waveguides with a parabolic refractive index profile. The Laguerre Gaussian model has the advantage that it provides a closed form expressions of all modes for arbitrary distances from the VCSEL.

The spatial field distribution of the Laguerre Gaussian modes LP_{lp} in cylindrical coordinates is given by [7]

$$\Phi_{lp}(r, \varphi, z) = A_0 \frac{w_0(l, p)}{w(z)} \left[\frac{\sqrt{2}r}{w(z)} \right]^l L_{p-1}^{(l)} \left[\frac{2r^2}{w^2(z)} \right] \exp \left\{ \frac{-r^2}{w^2(z)} + jl\varphi + \frac{jkr^2}{2R^2(z)} - jkz + j[2(p-1) + l + 1]\xi(z) \right\}, \quad (2.6)$$

where $L_{p-1}^{(l)}(x)$ is the generalized Laguerre polynomial of kind l and order $p-1$. Here l, p describe the azimuthal and radial mode order, $w(z)$ is the mode field radius, $w_0(l, p)$ is the radius of the beam waist of the mode LP_{lp} , $R(z)$ is the curvature of the beam wave front, $\xi(z)$ is the so-called Gouy phase², and $z_0(l, p)$ is the confocal parameter. These parameters are related to each other by the following equations:

$$z_0(l, p) = \frac{\pi w_0^2(l, p)}{\lambda}, \quad (2.7)$$

$$R(z) = z \left[1 + \left(\frac{z_0(l, p)}{z} \right)^2 \right], \quad (2.8)$$

$$w(z) = w_0(l, p) \sqrt{1 + \left(\frac{z_0(l, p)}{z} \right)^2}, \quad (2.9)$$

$$\xi(z) = \arctan \frac{z}{z_0(l, p)}. \quad (2.10)$$

In [7] the transversal modes of the VCSEL under investigation, the ULM Photonics multi-mode 5 Gbit/s device *ULM 850-05-TN-U46FOP* with center wavelength $\lambda = 850$ nm, are computed numerically using the software VISTAS (VCSEL Integrated Spatio Temporal Device Simulator). Since VISTAS uses the aforementioned Bessel modes, they are matched to corresponding Laguerre Gaussian modes using a minimum mean square error (MMSE) approximation. This approximation leads to different mode radii $w_0(l, p)$ for different modes LP_{lp} which are summarized in Table 2.3. These different mode radii destroy the orthogonality inherent to the Laguerre Gaussian modes (which is irrelevant for the investigations in this text). Figure B.1 shows the normalized intensity distributions of the VCSEL eigenmodes from Equation (2.6) with the mode radii from Table 2.3.

2.3.2 Gaussian LP_{01} Mode

From Equation (2.6) it is evident that the fundamental LP_{01} mode equals the so-called *Gaussian mode* [8]

$$\Phi_{01}(r, \varphi, z) = A_0 \frac{w_0}{w(z)} \exp \left[\frac{-r^2}{w^2(z)} + \frac{jkr^2}{2R^2(z)} - jkz + j\xi(z) \right], \quad (2.11)$$

²The Gouy phase describes the fast change in phase at the beam waist.

Table 2.3: Mode radii $w_0(l, p)$ of different Laguerre Gaussian modes LP_{01} MMSE-matched to the corresponding Bessel modes from VISTAS.

Mode	$w_0(l, p)/\mu\text{m}$
LP_{01}	2.10
LP_{11}	1.73
LP_{21}	1.54
LP_{02}	1.62
LP_{31}	1.41
LP_{12}	1.46
LP_{41}	1.32
LP_{22}	1.37
LP_{03}	1.41

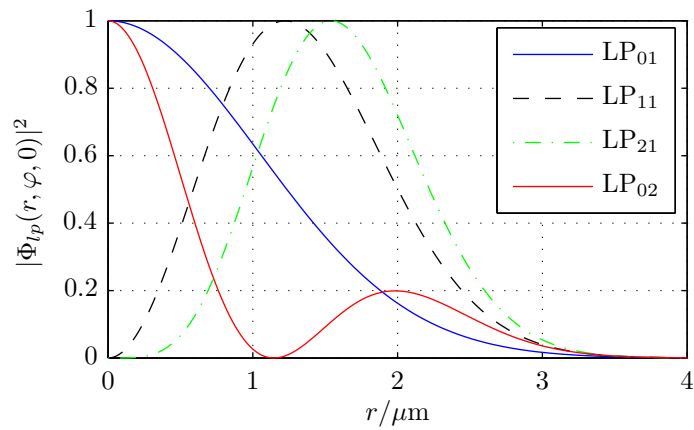


Figure 2.2: Normalized radial intensity distributions of some Laguerre Gaussian modes at $z = 0$.

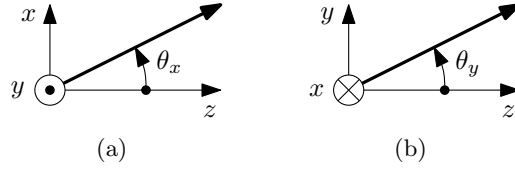


Figure 2.3: Definitions of the angles (a) θ_x and (b) θ_y with respect to the propagation direction z .

or using $r^2 = x^2 + y^2$ in Cartesian coordinates

$$\Phi_{01}(x, y, z) = A_0 \frac{w_0}{w(z)} \exp \left[-\frac{x^2 + y^2}{w^2(z)} + jk \frac{x^2 + y^2}{2R^2(z)} + jkz - j\xi(z) \right]. \quad (2.12)$$

For simplicity, offsets with respect to the x and y direction as well an angle of the beam are not taken into account in Equations (2.12) and (2.11). Offsets are realized by replacing x by $x - x_{\text{offset}}$ and y by $y - y_{\text{offset}}$, respectively, in Equation (2.12).

Gaussian beams which have an angle with respect to the propagation direction z are modelled as³

$$\Phi_{01}(x, y, 0) = |\Phi_{01}(x, y, 0)| \exp [j \arg\{\Phi_{01}(x, y, 0)\}], \quad (2.13)$$

with

$$|\Phi_{01}(x, y, 0)| = A_0 \exp \left[-\left(\frac{x}{w_0 / \cos(\theta_x)} \right)^2 - \left(\frac{y}{w_0 / \cos(\theta_y)} \right)^2 \right] \quad (2.14)$$

and

$$\arg\{\Phi_{01}(x, y, 0)\} = \frac{2\pi}{\lambda} [x \sin(\theta_x) + y \sin(\theta_y)]. \quad (2.15)$$

where θ_x designates the angle in the plane $y = 0$ and θ_y designates the angle in the plane $x = 0$, respectively. (see Figure 2.3).

³Here, $z = 0$ is assumed for the sake of simplicity.

Chapter 3

Finite-Difference Beam Propagation Method

3.1 Introduction and Outline

In this chapter the so-called Beam Propagation Method implemented in BEAMLABBPM is discussed. The main principle of this method is shown in Figure 3.1. The input parameter is the field $\Phi_{\text{in}}(x, y) = \Phi_0(x, y) = \Phi(x, y, 0)^1$ at $z = 0$. In each propagation step the field at $z + \Delta z$ is calculated until the output field $\Phi_{\text{out}}(x, y) = \Phi_L(x, y) = \Phi(x, y, L)$ at $z = L$ is obtained. Here, the propagation step distance Δz can be different for each propagation step, but in general we will use equidistant discretization with respect to the z direction. Figure 3.2 shows the lateral spatial discretization of the analysis area with $M_x \times M_y$ mesh grid points. Here, equidistant discretization is shown. BEAMLABBPM also supports non-equidistant discretization which, depending on the waveguide under consideration, can reduce the number of required mesh grid points and hence, the required computation time significantly.

There are various kinds of BPMs which use different approximations of the derivatives with respect to the lateral directions in the wave equation [9]:

- Fast Fourier Transform (FFT) BPM uses the fast Fourier transform [10],
- Finite Difference (FD) BPM uses a finite-difference approximation [11], and
- Finite Element (FE) BPM uses a finite-element approximation [12].

FFT-BPM. The FFT-BPM has been widely used in simulation software until the FD BPM was developed. It has the following major disadvantages mainly due to the nature of the FFT:

- It requires a long computation time compared to the other methods,
- only equidistant discretization with respect to the lateral directions can be implemented,
- the very efficient and practical Transparent Boundary Conditions (see Section 3.2.4) cannot be used,
- the propagation step distance Δz has to be very small, and
- very small discretization widths cannot be used in the lateral directions.

¹In Chapters 4 and 6 sometimes the fields $\Phi_{\text{in}}(x, y)$ and $\Phi_0(x, y)$ are not equal— $\Phi_{\text{in}}(x, y)$ is always the input field of the BEAMLABBPM simulations, while $\Phi_0(x, y)$ can be a different field under investigation. If not mentioned otherwise, $\Phi_{\text{in}}(x, y) = \Phi_0(x, y)$.

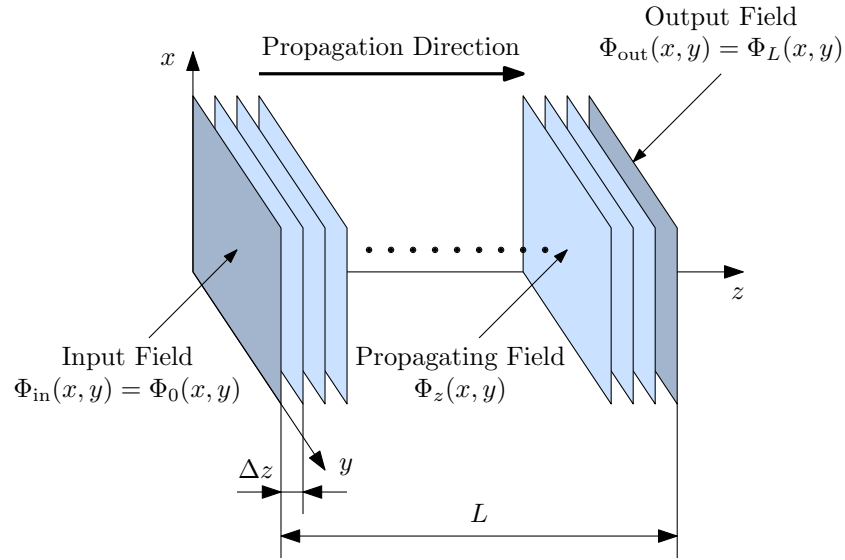


Figure 3.1: The main principle of the Beam Propagation Method: The propagating field at $z + \Delta z$ is calculated from the previous field at z .

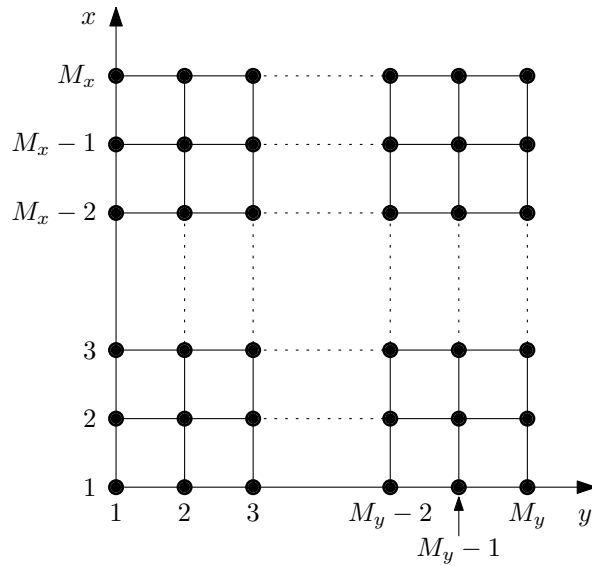


Figure 3.2: Lateral spatial discretization of the analysis area. Here, equidistant discretization is shown, but non-equidistant discretization is also possible in x and y direction.

FD-BPM. BEAMLABBPM implements the much more powerful FD-BPM using the an *implicit scheme* from [11] which is very accurate, numerically efficient, and unconditional stable². This unconditional stability is very useful because it allows the propagation step distance Δz to be relatively large compared to the FFT-BPM which in turn significantly reduces the computation time. Additionally, Transparent Boundary Conditions (see Section 3.2.4) can be used, which employ no adjustable parameters, and are thus problem independent. BEAMLABBPM uses a paraxial approximation which imposes an upper limit on the angles of the propagating beams. There also exist wide-angle schemes using Padé approximant operators [13] which will not be discussed here.

Most of the derivations of the discretized FD-BPM formulations presented here is very similar to the derivations from [9]. There are two major reasons why they are included in this work:

- In order to understand the limitations of the Beam Propagation Method, it is mandatory to know which approximations are used in the derivations of the FD-BPM formulations.
- Unfortunately, in [9] there are some mistakes which would make it impossible to implement the Beam Propagation Method.

This chapter is organized as follows.

- In Section 3.2 the derivation of the two-dimensional semivectorial FD-BPM is presented. Starting with the well-known Maxwell equations the spatially discretized FD-BPM formulations, which can be solved efficiently using MATLAB, are developed. A non-equidistant discretization scheme, as well as Transparent Boundary Conditions are also discussed.
- In Section 3.3 we discuss the three-dimensional semivectorial analysis using the numerically very efficient Alternate Direction Implicit (ADI) method.
- In Section 3.4 the different approximations used in Section 3.2 and their implications on the simulation results' accuracy are analyzed in detail.
- Section 3.5 presents the so-called Imaginary Distance BPM which allows to calculate the fundamental eigenmode of a waveguide in only a few BPM propagation steps.

3.2 Two-Dimensional Semivectorial Analysis

3.2.1 Wave Equation

The electromagnetic fields satisfy the following well-known *Maxwell equations*³:

$$\vec{\nabla} \times \vec{E} = -\partial_t \vec{B}, \quad (3.1)$$

$$\vec{\nabla} \times \vec{H} = \vec{J} + \partial_t \vec{D}, \quad (3.2)$$

$$\vec{\nabla} \cdot \vec{D} = \rho, \quad (3.3)$$

$$\vec{\nabla} \cdot \vec{B} = 0, \quad (3.4)$$

²A simulation method is called *unconditional stable* if propagating fields cannot diverge for *any* input field. Oscillations, however, are possible.

³Following the nomenclature from [14] we will use $\partial_t = \partial/\partial t$ for the partial derivative with respect to time and $\partial_x = \partial/\partial x$, $\partial_y = \partial/\partial y$, and $\partial_z = \partial/\partial z$ for the partial derivatives with respect to the direction x , y , and z , respectively.

where \vec{E} is the electric field, \vec{H} is the magnetic field, \vec{D} is the electric flux density, \vec{B} is the magnetic flux density, \vec{J} is the current density, and ϱ is the density of volume charge. Furthermore in a linear and isotropic—but not necessarily homogeneous—material these electromagnetic fields are related to each other through the equations

$$\vec{D} = \varepsilon \vec{E}, \quad (3.5)$$

$$\vec{B} = \mu \vec{H}, \quad (3.6)$$

where the permittivity ε and permeability μ are defined as

$$\varepsilon = \varepsilon_0 \varepsilon_r, \quad (3.7)$$

$$\mu = \mu_0 \mu_r. \quad (3.8)$$

Here, $\varepsilon_0 = (\mu_0 c_0^2)^{-1}$ and $\mu_0 = 4\pi \cdot 10^{-7} \text{ Vs}/(\text{Am})$ are the permittivity and permeability of a vacuum, and ε_r and μ_r are the relative permittivity and permeability of the material, respectively. Since $\mu_r = 1$ for materials other than magnetic materials, it is assumed to be 1 in the following. In general, $\varepsilon_r = \varepsilon_r' - j\varepsilon_r''$ is a complex number with $\varepsilon_r'' = -\Im\{\varepsilon_r\} \neq 0$ for lossy materials. [15] The optical waveguides investigated in this work are assumed to be lossless, and therefore $\varepsilon_r'' = 0$ in the following. Nevertheless, BEAMLAB is also capable of simulating light propagation in lossy materials.

If a general vector field \vec{F} oscillates at a single angular frequency ω , it can be expressed as

$$\vec{F}(\vec{r}, t) = \Re \left\{ \vec{\mathcal{F}}(\vec{r}) \exp(j\omega t) \right\}. \quad (3.9)$$

Using this form of representation, the electromagnetic fields can be written as

$$\vec{E}(\vec{r}, t) = \Re \left\{ \vec{\mathcal{E}}(\vec{r}) \exp(j\omega t) \right\}, \quad (3.10)$$

$$\vec{H}(\vec{r}, t) = \Re \left\{ \vec{\mathcal{H}}(\vec{r}) \exp(j\omega t) \right\}, \quad (3.11)$$

$$\vec{D}(\vec{r}, t) = \Re \left\{ \vec{\mathcal{D}}(\vec{r}) \exp(j\omega t) \right\}, \quad (3.12)$$

$$\vec{B}(\vec{r}, t) = \Re \left\{ \vec{\mathcal{B}}(\vec{r}) \exp(j\omega t) \right\}. \quad (3.13)$$

If we plug these equations in Equations (3.1) to (3.4) we get with the slight abuse of notation using \vec{F} as $\vec{\mathcal{F}}$ ⁴

$$\vec{\nabla} \times \vec{E} = -j\omega \vec{B} = -j\omega \mu_0 \vec{H}, \quad (3.14)$$

$$\vec{\nabla} \times \vec{H} = j\omega \vec{D} = j\omega \varepsilon_0 \varepsilon_r \vec{E}, \quad (3.15)$$

$$\vec{\nabla} \cdot \vec{H} = 0, \quad (3.16)$$

$$\vec{\nabla} \cdot (\varepsilon_r \vec{E}) = 0. \quad (3.17)$$

where $\mu_r = 1$, $\varrho = 0$, and $\vec{J} = 0$ is assumed. The component representations of these equations are

$$\partial_y E_z - \partial_z E_y = -j\omega \mu_0 H_x, \quad (3.18)$$

$$\partial_z E_x - \partial_x E_z = -j\omega \mu_0 H_y, \quad (3.19)$$

$$\partial_x E_y - \partial_y E_x = -j\omega \mu_0 H_z, \quad (3.20)$$

$$\partial_y H_z - \partial_z H_y = j\omega \varepsilon_0 \varepsilon_r E_x, \quad (3.21)$$

$$\partial_z H_x - \partial_x H_z = j\omega \varepsilon_0 \varepsilon_r E_y, \quad (3.22)$$

$$\partial_x H_y - \partial_y H_x = j\omega \varepsilon_0 \varepsilon_r E_z. \quad (3.23)$$

⁴In Equations (3.9)–(3.13) $\vec{F}(\vec{r}, t)$ is a function of \vec{r} and t , while from now on $\vec{F}(\vec{r}) = \vec{\mathcal{F}}(\vec{r})$ is a function only of \vec{r} .

In the two-dimensional semivectorial analysis we assume the structure of the waveguide to be uniform in the y direction. In this case the derivatives with respect to y can be set to zero, i.e.

$$-\partial_z E_y = -j\omega\mu_0 H_x, \quad (3.24)$$

$$\partial_z E_x - \partial_x E_z = -j\omega\mu_0 H_y, \quad (3.25)$$

$$\partial_x E_y = -j\omega\mu_0 H_z, \quad (3.26)$$

$$-\partial_z H_y = j\omega\varepsilon_0\varepsilon_r E_x, \quad (3.27)$$

$$\partial_z H_x - \partial_x H_z = j\omega\varepsilon_0\varepsilon_r E_y, \quad (3.28)$$

$$\partial_x H_y = j\omega\varepsilon_0\varepsilon_r E_z. \quad (3.29)$$

TE Mode. In the TE mode the electric field component in the longitudinal direction is zero, i.e. $E_z = 0$. Since here we assume $\partial_y = 0$, Equation (3.29) results in $\partial_x H_y = 0$. This means that H_y has to be constant and we can assume that $H_y = 0$. Furthermore, substitution of $E_z = H_y = 0$ into Equation (3.25) results in $\partial_z E_x$, which means that we can assume $E_x = 0$. We thus get

$$E_x = E_z = H_y = 0. \quad (3.30)$$

Substituting Equation (3.35) into Equations (3.24) to (3.29) we obtain the following wave equation for the principal electrical field component E_y :

$$\partial_z^2 E_y + \partial_x^2 E_y + k_0^2 \varepsilon_r E_y = 0, \quad (3.31)$$

where $k_0^2 = \omega^2 \varepsilon_0 \mu_0$. In a similar way the wave equation for the x -directed magnetic field component H_x can be derived:

$$\partial_z^2 H_x + \partial_x^2 H_x + k_0^2 \varepsilon_r H_x = 0. \quad (3.32)$$

It is important to note that here the approximation

$$\partial_z(\varepsilon_r E_y) = E_y \partial_z \varepsilon_r + \varepsilon_r \partial_z E_y \approx \varepsilon_r \partial_z E_y \quad (3.33)$$

was used. This means that the approximation

$$\boxed{\partial_z \varepsilon_r \approx 0} \quad (3.34)$$

is implicitly used in the BPM. In Section 6.8 we will see that this approximation can be problematic for specific use cases.

TM Mode. In the TM mode the magnetic field component in the longitudinal direction is zero, i.e. $H_z = 0$. Similar to the TE mode we now get $\partial_x E_y = 0$ from (3.26) when using the condition $\partial_y = 0$. This means that E_y has to be constant and we can assume $E_y = 0$. Furthermore, substitution of $H_z = E_y = 0$ into Equation (3.29) results in $\partial_z H_x$, which means that we can assume $H_x = 0$. We thus get

$$H_x = H_z = E_y = 0. \quad (3.35)$$

The wave equation for the x -directed electric field component E_x is

$$\partial_z^2 E_x + \partial_x \left[\frac{1}{\varepsilon_r} \partial_x (\varepsilon_r E_x) \right] + k_0^2 \varepsilon_r E_x = 0, \quad (3.36)$$

and the wave equation for H_y is

$$\partial_z^2 H_y + \varepsilon_r \partial_x \left(\frac{1}{\varepsilon_r} \partial_x H_y \right) + k_0^2 \varepsilon_r H_y = 0. \quad (3.37)$$

We now have derived a set of four wave equations which can be solved numerically using finite-difference expressions which will be discussed in the next section.

3.2.2 FD-BPM Formulation

BEAMLABBPM uses a FD-BPM formulation based on the implicit scheme from [11]. In this section we will derive the finite difference approximations of Equations (3.31), (3.32), (3.36), and (3.37).

Scalar Helmholtz equation. We will start with the general three-dimensional scalar Helmholtz equation

$$\nabla^2 \Psi(x, y, z) + k_0^2 n^2(x, y, z) \Psi(x, y, z) = 0, \quad (3.38)$$

where $\nabla^2 = \partial_x^2 + \partial_y^2 + \partial_z^2$ is the Laplacian and k_0 is the wave number in vacuum. Using the so-called *slowly varying envelope approximation* the wave function $\Psi(x, y, z)$ of the light propagating in the z direction is divided into the slowly varying envelope function $\Phi(x, y, z)$ and a spatially very fast oscillating phase term $\exp(-j\beta z)$ as follows:

$$\boxed{\Psi(x, y, z) = \Phi(x, y, z) \exp(-j\beta z)}. \quad (3.39)$$

Here,

$$\beta = n_{\text{eff}} k_0, \quad (3.40)$$

where n_{eff} is the *effective refractive index*. In actual calculations, this value is a-priori unknown and can be set to the refractive index of the substrate or cladding [9]. Substituting

$$\partial_z^2 \Psi = \exp(-j\beta z) \partial_z^2 \Phi - 2j\beta \exp(-j\beta z) \partial_z \Phi - \beta^2 \Phi \exp(-j\beta z), \quad (3.41)$$

which can be obtained from Equation (3.39), into Equation (3.38) and dividing both sides of the resultant equation by $\exp(-j\beta z)$, we get

$$\partial_z^2 \Phi - 2j\beta \partial_z \Phi + \nabla_{\perp}^2 \Phi + (k_0^2 n^2 - \beta^2) \Phi = 0, \quad (3.42)$$

where $\nabla_{\perp}^2 = \partial_x^2 + \partial_y^2$ is the Laplacian in the lateral directions and $\varepsilon_r = n^2$. Equation (3.42) can also be written as

$$2j\beta \partial_z \Phi - \partial_z^2 \Phi = \nabla_{\perp}^2 \Phi + k_0^2 (\varepsilon_r - n_{\text{eff}}^2) \Phi, \quad (3.43)$$

which is the so-called *wide-angle formulation* since the second derivative of the wave function Φ with respect to z is not neglected. If we neglect this second derivative, i.e.

$$\boxed{\partial_z^2 \Phi = 0}, \quad (3.44)$$

Equation (3.43) is reduced to

$$2j\beta \partial_z \Phi = \nabla_{\perp}^2 \Phi + k_0^2 (\varepsilon_r - n_{\text{eff}}^2) \Phi. \quad (3.45)$$

This approximation is called the *Fresnel approximation* or the *paraxial approximation*. When simulating light propagation in optical waveguides, neglecting the second derivative of the wave function Φ is justified in many cases. In Section 3.4 we will further investigate the implications of this approximation.

TE Mode. Here we will use a two-dimensional model of the principal field $E_y(x, y, z)$ which means that $\partial_y E_y = 0$. Using the slowly varying envelope approximation from Equation (3.39), i.e.

$$E_y(x, y, z) = \Phi(x, y, z) \exp(-j\beta z), \quad (3.46)$$

we get the Fresnel equation

$$2j\beta \partial_z \Phi = \partial_x^2 \Phi + k_0^2 (\varepsilon_r - n_{\text{eff}}^2) \Phi. \quad (3.47)$$

We now discretize the x and z coordinates according to

$$x = p \Delta x, \quad (3.48)$$

$$y = l \Delta z, \quad (3.49)$$

where p and l are integers. In the following, the spatially discretized versions of the wave function $\Phi(x, z)$ and the relative permittivity $\varepsilon_r(x, z)$ are notated as

$$\Phi(x, z) \rightarrow \Phi_p^{(l)}, \quad (3.50)$$

$$\varepsilon_r(x, z) \rightarrow \varepsilon_r^{(l)}(p). \quad (3.51)$$

First, we discretize Equation (3.47) in the x direction, i.e. the terms on the right-hand are expressed as (see [16] for more details about the FD discretization used here)

$$\partial_x^2 \Phi = \frac{1}{\Delta x} \left(\frac{\Phi_{p+1} - \Phi_p}{\Delta x} - \frac{\Phi_p - \Phi_{p-1}}{\Delta x} \right) = \frac{\Phi_{p+1} - 2\Phi_p + \Phi_{p-1}}{(\Delta x)^2}, \quad (3.52)$$

$$k_0^2(\varepsilon_r - n_{\text{eff}}^2)\Phi = k_0^2(\varepsilon_r(p) - n_{\text{eff}}^2)\Phi_p. \quad (3.53)$$

Discretizing the left-hand side of Equation (3.47) in the z direction, we get

$$2j\beta \frac{\Phi_p^{l+1} - \Phi_p^{(l)}}{\Delta z}. \quad (3.54)$$

Using the definitions

$$\alpha_w = \frac{1}{(\Delta x)^2}, \quad (3.55)$$

$$\alpha_e = \frac{1}{(\Delta x)^2}, \quad (3.56)$$

$$\alpha_x = -\frac{1}{(\Delta x)^2}, \quad (3.57)$$

we finally get the finite difference expression of the TE mode principal field $E_y(x, y, z)$:

$$\begin{aligned} & \underbrace{-\alpha_w^{(l+1)}}_{a_p} \Phi_{p-1}^{(l+1)} + \underbrace{\left\{ -\alpha_x^{(l+1)} + \frac{4j\beta}{\Delta z} - k_0^2 \left[\varepsilon_r^{(l+1)}(p) - n_{\text{eff}}^2 \right] \right\}}_{b_p} \Phi_p^{(l+1)} - \underbrace{\alpha_e^{(l+1)}}_{c_p} \Phi_{p+1}^{(l+1)} \\ & = \underbrace{\alpha_w^{(l)} \Phi_{p-1}^{(l)} + \left\{ \alpha_x^{(l)} + \frac{4j\beta}{\Delta z} + k_0^2 \left[\varepsilon_r^{(l)}(p) - n_{\text{eff}}^2 \right] \right\}}_{d_p} \Phi_p^{(l)} + \alpha_e^{(l)} \Phi_{p+1}^{(l)}. \end{aligned} \quad (3.58)$$

Since Equations (3.31) and (3.32) are equal, Equation (3.58) is also valid for the principal field $H_x(x, y, z)$.

TM Mode. Using the slowly varying envelope approximation from Equation (3.39) for the TM mode principal magnetic field component $H_y(x, y, z)$ and inserting it into Equation (3.37), we get the Fresnel wave equation

$$2j\beta \partial_z \Phi = \varepsilon_r \partial_x \left(\frac{1}{\varepsilon_r} \partial_x \Phi \right) + k_0^2(\varepsilon_r - n_{\text{eff}}^2)\Phi. \quad (3.59)$$

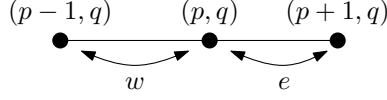


Figure 3.3: One-dimensional non-equidistant discretization.

Using the spatial discretizations from Equations (3.48)–(3.51) we get the the same finite difference expression as for the TE case, i.e. Equation (3.58), only with different definitions of

$$\alpha_w = \frac{1}{(\Delta x)^2} \frac{2\varepsilon_r(p)}{\varepsilon_r(p) + \varepsilon_r(p-1)}, \quad (3.60)$$

$$\alpha_e = \frac{1}{(\Delta x)^2} \frac{2\varepsilon_r(p)}{\varepsilon_r(p) + \varepsilon_r(p+1)}, \quad (3.61)$$

$$\alpha_x = -\alpha_e - \alpha_w. \quad (3.62)$$

The finite difference discretization of the TM mode principal electrical field $E_x(x, y, z)$ leads to

$$\alpha_w = \frac{1}{(\Delta x)^2} \frac{2\varepsilon_r(p-1)}{\varepsilon_r(p) + \varepsilon_r(p-1)}, \quad (3.63)$$

$$\alpha_e = \frac{1}{(\Delta x)^2} \frac{2\varepsilon_r(p+1)}{\varepsilon_r(p) + \varepsilon_r(p+1)}, \quad (3.64)$$

$$\alpha_x = -\frac{4}{(\Delta x)^2} + \alpha_e + \alpha_w. \quad (3.65)$$

3.2.3 Non-Equidistant Discretization Scheme

Until now we assumed equidistant discretization with respect to the x direction. In actual simulations it can be very convenient to discretize non-equidistantly—for example if a waveguide structure is uniform in a specific spatial region it might reduce the overall simulation time significantly if we choose a larger discretization distance only in that region. Regions where a finer spatial granularity is required to model the structure sufficiently accurate can be chosen to have a smaller discretization step size. Figure 3.3 shows the one-dimensional discretization mesh for the two-dimensional semivectorial analysis.

It can be shown that Equation (3.58) can still be used, again just with different coefficients. [9]

TE Mode. E_y and H_x representation:

$$\alpha_w = \frac{2}{w(e+w)} \quad (3.66)$$

$$\alpha_e = \frac{2}{e(e+w)} \quad (3.67)$$

$$\alpha_x = -\alpha_e - \alpha_w \quad (3.68)$$

TM Mode. E_x representation:

$$\alpha_w = \frac{2}{w(e+w)} \frac{2\varepsilon_r(p-1)}{\varepsilon_r(p) + \varepsilon_r(p-1)} \quad (3.69)$$

$$\alpha_e = \frac{w}{e(e+w)} \frac{2\varepsilon_r(p+1)}{\varepsilon_r(p) + \varepsilon_r(p+1)} \quad (3.70)$$

$$\alpha_x = -\frac{4}{ew} + \alpha_e + \alpha_w \quad (3.71)$$

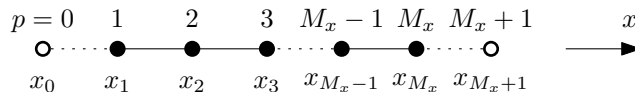


Figure 3.4: Location of the nodes $p = 0$ and $p = M_x + 1$ outside of the actual analysis area.

H_y representation:

$$\alpha_w = \frac{2}{w(e+w)} \frac{2\varepsilon_r(p)}{\varepsilon_r(p) + \varepsilon_r(p-1)} \quad (3.72)$$

$$\alpha_e = \frac{2}{e(e+w)} \frac{2\varepsilon_r(p)}{\varepsilon_r(p) + \varepsilon_r(p+1)} \quad (3.73)$$

$$\alpha_x = -\alpha_e - \alpha_w \quad (3.74)$$

3.2.4 Transparent Boundary Conditions

In actual simulations it is not possible to simulate an infinitely wide area with no spatial analysis boundaries because of memory and computation time limitations. Therefore one has to choose a reasonable large finite simulation area where reflections at the boundaries can occur. Unfortunately, if no countermeasures are taken the beam propagation method is somewhat deficient when it comes to simulating waveguide structures which scatter a significant amount of light power towards these simulation boundaries. The reflections cause unwanted interference effects which can severely impair the overall accuracy.

In this section the so-called *Transparent Boundary Conditions* (TBC) from [17] are presented. The TBC simulate a nonexistent boundary. Radiation is allowed to freely escape the simulation area without appreciable reflections. The huge advantage of the TBC over other boundary conditions such as the Absorbing Boundary Conditions (ABC) [18] is that it employs no adjustable parameters, and is thus problem independent. On the other hand, the ABC inserts artificial absorption regions adjacent to the pertinent boundaries. The thickness of the region, the maximum absorption coefficient, and the functional shape of the absorption coefficient must all be chosen carefully for the method to work properly. Each problem requires the adjustment of these parameters to different values in order to ensure sufficient boundary reflection suppression. If the gradient in the absorption coefficient chosen is too large, that gradient itself will generate reflections.

In Section 3.4.3 the TBC boundary reflectivity is analyzed in more detail. It should be stressed that the TBC is only an approximative method where some residual reflections exist. In principal, it is also possible to calculate complete reflection-free boundary conditions but the computation complexity is very high. [19]

As shown in Figure 3.4, the (one-dimensional) TBC assumes two additional nodes at $p = 0$ and $p = M_x + 1$ which are not in the actual analysis area. The trick of the TBC is to incorporate the influence of these two nodes into their adjacent nodes at $p = 1$ and $p = M_x$.

Left-Hand Boundary. We start the derivation with the wave function of the left-traveling wave with the x -directed wave number k_x

$$\Phi(x, z) = A(z) \exp(jk_x x). \quad (3.75)$$

With fields at the nodes expressed as

$$\Phi_p = A(z) \exp(jk_x x_p), \quad (3.76)$$

it follows from dividing Φ_2 by Φ_1 and Φ_1 by Φ_0

$$\eta_1 = \frac{\Phi_2}{\Phi_1} = \frac{\Phi_1}{\Phi_0} = \exp(jk_x \Delta x), \quad (3.77)$$

where $\Delta x = x_2 - x_1 = x_1 - x_0$. Now

$$\Phi_0 = \frac{1}{\eta_1} \Phi_1 = \Phi_1 \exp(-jk_x \Delta x), \quad (3.78)$$

with

$$k_x = \frac{1}{j\Delta x} \ln(\eta_1). \quad (3.79)$$

In order to prevent radiation flux back into the problem region, it is very important that

$$\boxed{\Re\{k_x\} < 0}. \quad (3.80)$$

If this condition is not fulfilled, the sign of k_x must be changed in the actual simulation software.

Right-Hand Boundary. Analog to the derivation of the left-hand boundary conditions, we get for the right-hand boundary

$$\Phi_{M_x+1} = \eta_{M_x} \Phi_{M_x} = \Phi_{M_x} \exp(-jk_x \Delta x), \quad (3.81)$$

where

$$\eta_{M_x} = \frac{\Phi_{M_x}}{\Phi_{M_x-1}}, \quad (3.82)$$

and

$$k_x = -\frac{1}{j\Delta x} \ln(\eta_{M_x}). \quad (3.83)$$

Here,

$$\boxed{\Re\{k_x\} > 0} \quad (3.84)$$

is necessary for unidirectional radiation flux out of the analysis area.

3.2.5 Implementation in Matlab

Equation (3.58) for all possible values of $p = 1, \dots, M_x$ can conveniently be written as the following matrix equation:

$$\underbrace{\begin{pmatrix} b_1 & c_1 & 0 & 0 & 0 & \dots & 0 \\ a_2 & b_2 & c_2 & 0 & 0 & \dots & 0 \\ 0 & a_3 & b_3 & c_3 & 0 & \dots & 0 \\ \dots & \dots & \dots & \dots & \dots & \dots & \dots \\ 0 & \dots & 0 & a_{M_x-1} & b_{M_x-1} & c_{M_x-1} \\ 0 & \dots & 0 & a_{M_x} & b_{M_x} \end{pmatrix}}_{\mathbf{T}} \underbrace{\begin{pmatrix} \Phi_1^{(l+1)} \\ \Phi_2^{(l+1)} \\ \Phi_3^{(l+1)} \\ \vdots \\ \Phi_{M_x-1}^{(l+1)} \\ \Phi_{M_x}^{(l+1)} \end{pmatrix}}_{\Phi^{(l+1)}} = \underbrace{\begin{pmatrix} d_1 \\ d_2 \\ d_3 \\ \vdots \\ d_{M_x-1} \\ d_{M_x} \end{pmatrix}}_d. \quad (3.85)$$

The variables b_1 , c_1 , and d_1 contain the Transparent Boundary Conditions of the left-hand boundary, while the variables a_{M_x} , b_{M_x} , and d_{M_x} contain the Transparent Boundary Conditions of the right-hand boundary from Subsection 3.2.4. [9] The tridiagonal matrix equation

$$\mathbf{T} \Phi^{(l+1)} = d \quad (3.86)$$

can be solved in MATLAB simply by using the command

$\text{phi} = \mathbb{T} \backslash \underline{d};$

where the variable \mathbb{T} contains the matrix \mathbf{T} , \underline{d} contains the vector \underline{d} , and the result $\underline{\Phi}^{(l+1)}$ is stored in the vector `phi`.

3.3 Three-Dimensional Semivectorial Analysis

In principal the 2D-BPM discussed above can be extended to the 3D-BPM in a rather straightforward manner. BEAMLABBPM implements a much more numerically efficient 3D-BPM technique based on the Alternate Direction Implicit (ADI) method [20]. The ADI-BPM reduces the three-dimensional problem to two two-dimensional problems by dividing one propagation step $z \rightarrow z + \Delta z$ into two separate steps $z \rightarrow z + \Delta z/2$ and $z + \Delta z/2 \rightarrow z + \Delta z$ which are solved successively in the x and y directions. The computation of one large matrix equation is replaced by solving two tridiagonal matrix equations which reduces the required computation time significantly.

In two-dimensional semivectorial analysis in Section 3.2, we assumed $\partial_y = 0$, i.e. the refractive index profile and electric and magnetic fields were invariant with respect to the y direction. In the three-dimensional semivectorial analysis derivatives with respect to the y direction do not vanish and therefore the wave equations to be solved are numerically different. [9]

TE Mode. E_y representation:

$$\partial_z^2 E_y + \partial_x^2 E_y + \partial_y \left[\frac{1}{\varepsilon_r} \partial_y (\varepsilon_r E_y) \right] + k_0^2 \varepsilon_r E_y = 0 \quad (3.87)$$

H_x representation:

$$\partial_z^2 H_x + \partial_x^2 H_x + \varepsilon_r \partial_y \left(\frac{1}{\varepsilon_r} \partial_y H_x \right) + k_0^2 \varepsilon_r H_x = 0 \quad (3.88)$$

TM Mode. E_x representation:

$$\partial_z^2 E_x + \partial_x \left[\frac{1}{\varepsilon_r} \partial_x (\varepsilon_r E_x) \right] + \partial_y^2 E_x + k_0^2 \varepsilon_r E_x = 0 \quad (3.89)$$

H_y representation:

$$\partial_z^2 H_y + \varepsilon_r \partial_x \left(\frac{1}{\varepsilon_r} \partial_x H_y \right) + \partial_y^2 H_y + k_0^2 \varepsilon_r H_y = 0 \quad (3.90)$$

Using the slowly varying envelope approximation from Equation (3.39) and the Fresnel approximation from Equation (3.44), Equations (3.87)–(3.90) simplify to

$$2j\beta \partial_z \Phi = \partial_x^2 \Phi + \partial_y \left[\frac{1}{\varepsilon_r} \partial_y (\varepsilon_r \Phi) \right] + (k_0^2 \varepsilon_r - \beta^2) \Phi, \quad (3.91)$$

with $\Phi = E_y$ for the TE mode E_y representation,

$$2j\beta \partial_z \Phi = \partial_x^2 \Phi + \varepsilon_r \partial_y \left(\frac{1}{\varepsilon_r} \partial_y \Phi \right) + (k_0^2 \varepsilon_r - \beta^2) \Phi, \quad (3.92)$$

with $\Phi = H_x$ for the TE mode H_x representation,

$$2j\beta \partial_z \Phi = \partial_x \left[\frac{1}{\varepsilon_r} \partial_x (\varepsilon_r \Phi) \right] + \partial_y^2 \Phi + (k_0^2 \varepsilon_r - \beta^2) \Phi, \quad (3.93)$$

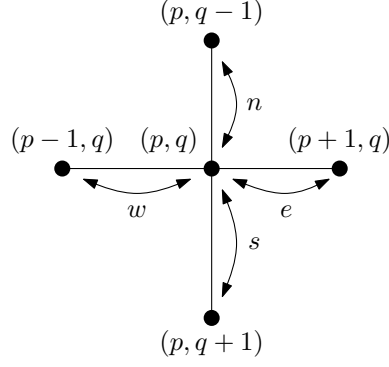


Figure 3.5: Two-dimensional non-equidistant discretization.

with $\Phi = E_x$ for the TM mode E_x representation, and

$$2j\beta\partial_z\Phi = \varepsilon_r\partial_x\left(\frac{1}{\varepsilon_r}\partial_x\Phi\right) + \partial_y^2\Phi + (k_0^2\varepsilon_r - \beta^2)\Phi, \quad (3.94)$$

with $\Phi = H_y$ for the TM mode H_y representation, respectively.

For the discretization, we use the two-dimensional non-equidistant discretization mesh from Figure 3.5. The discretized coordinates for (x, y, z) are (x_p, y_q, z_l) , where p, q, l are integers. The discretized versions of the fields $\Phi(x, y, z)$ and the relative permittivity $\varepsilon_r(x, y, z)$ are notated as

$$\Phi(x_p, y_q, z_l) = \Phi_{p,q}^{(l)}, \quad (3.95)$$

$$\varepsilon_r(x_p, y_q, z_l) = \varepsilon_r^{(l)}(p, q). \quad (3.96)$$

The discretization widths are defined as

$$n = y_q - y_{q-1}, \quad (3.97)$$

$$s = y_{q+1} - y_q, \quad (3.98)$$

$$e = x_{p+1} - x_p, \quad (3.99)$$

$$w = x_p - x_{p-1}. \quad (3.100)$$

Like in Section 3.2.2, Equations (3.91)–(3.94) can be represented by a single difference equation

$$\begin{aligned} 2j\beta\partial_z = & \underbrace{(\alpha_w\Phi_{p-1,q} + \alpha_e\Phi_{p+1,q} + \alpha_x\Phi_{p,q})}_{\text{derivative with respect to } x} \\ & + \underbrace{(\alpha_n\Phi_{p,q-1} + \alpha_s\Phi_{p,q+1} + \alpha_y\Phi_{p,q})}_{\text{derivative with respect to } y} \\ & + k_0^2 [\varepsilon_r(p, q) - n_{\text{eff}}^2] \Phi_{p,q}. \end{aligned} \quad (3.101)$$

TE mode E_y and H_x representation and TM mode E_x and H_y representation are now characterized by the six parameters $\alpha_w, \alpha_e, \alpha_n, \alpha_s, \alpha_x,$ and α_y instead of just the three parameters $\alpha_w, \alpha_e,$ and α_x from Equations (3.66)–(3.74). [9]

TE Mode. E_y representation:

$$\alpha_w = \frac{2}{w(e+w)} \frac{2\varepsilon_r(p-1, q)}{\varepsilon_r(p, q) + \varepsilon_r(p-1, q)} \quad (3.102)$$

$$\alpha_e = \frac{2}{e(e+w)} \frac{2\varepsilon_r(p+1, q)}{\varepsilon_r(p, q) + \varepsilon_r(p+1, q)} \quad (3.103)$$

$$\alpha_n = \frac{2}{n(n+s)} \quad (3.104)$$

$$\alpha_s = \frac{2}{s(n+s)} \quad (3.105)$$

$$\alpha_x = -\frac{4}{ew} + \alpha_e + \alpha_w \quad (3.106)$$

$$\alpha_y = -\alpha_n - \alpha_s \quad (3.107)$$

H_x representation:

$$\alpha_w = \frac{2}{w(e+w)} \frac{2\varepsilon_r(p, q)}{\varepsilon_r(p, q) + \varepsilon_r(p-1, q)} \quad (3.108)$$

$$\alpha_e = \frac{2}{e(e+w)} \frac{2\varepsilon_r(p, q)}{\varepsilon_r(p, q) + \varepsilon_r(p+1, q)} \quad (3.109)$$

$$\alpha_n = \frac{2}{n(n+s)} \quad (3.110)$$

$$\alpha_s = \frac{2}{s(n+s)} \quad (3.111)$$

$$\alpha_x = -\alpha_e - \alpha_w \quad (3.112)$$

$$\alpha_y = -\alpha_n - \alpha_s \quad (3.113)$$

TM Mode. E_x representation:

$$\alpha_w = \frac{2}{w(e+w)} \quad (3.114)$$

$$\alpha_e = \frac{2}{e(e+w)} \quad (3.115)$$

$$\alpha_n = \frac{2}{n(n+s)} \frac{2\varepsilon_r(p, q-1)}{\varepsilon_r(p, q) + \varepsilon_r(p, q-1)} \quad (3.116)$$

$$\alpha_s = \frac{2}{s(n+s)} \frac{2\varepsilon_r(p, q+1)}{\varepsilon_r(p, q) + \varepsilon_r(p, q+1)} \quad (3.117)$$

$$\alpha_x = -\alpha_e - \alpha_w \quad (3.118)$$

$$\alpha_y = -\frac{4}{ns} + \alpha_n + \alpha_s \quad (3.119)$$

H_y representation:

$$\alpha_w = \frac{2}{w(e+w)} \quad (3.120)$$

$$\alpha_e = \frac{2}{e(e+w)} \quad (3.121)$$

$$\alpha_n = \frac{2}{n(n+s)} \frac{2\varepsilon_r(p,q)}{\varepsilon_r(p,q) + \varepsilon_r(p,q-1)} \quad (3.122)$$

$$\alpha_s = \frac{2}{s(n+s)} \frac{2\varepsilon_r(p,q)}{\varepsilon_r(p,q) + \varepsilon_r(p,q+1)} \quad (3.123)$$

$$\alpha_x = -\alpha_e - \alpha_w \quad (3.124)$$

$$\alpha_y = -\alpha_n - \alpha_s \quad (3.125)$$

Scalar Mode.

$$\alpha_w = \frac{2}{w(e+w)} \quad (3.126)$$

$$\alpha_e = \frac{2}{e(e+w)} \quad (3.127)$$

$$\alpha_n = \frac{2}{n(n+s)} \quad (3.128)$$

$$\alpha_s = \frac{2}{s(n+s)} \quad (3.129)$$

$$\alpha_x = -\alpha_e - \alpha_w \quad (3.130)$$

$$\alpha_y = -\alpha_n - \alpha_s \quad (3.131)$$

3.3.1 First ADI Step

The first ADI propagation step is $z \rightarrow z + \Delta z/2$, or equivalently $l \rightarrow l + 1/2$. The derivative with respect to x in Equation (3.101) is expressed by the implicit FD expression using the *unknown fields* at $l + 1/2$, i.e.

$$\alpha_w^{(l+1/2)} \Phi_{p-1,q}^{(l+1/2)} + \alpha_e^{(l+1/2)} \Phi_{p+1,q}^{(l+1/2)} + \alpha_x^{(l+1/2)} \Phi_{p,q}^{(l+1/2)}. \quad (3.132)$$

The derivative with respect to y is written as explicit FD expression using the *known fields* at l , i.e.

$$\alpha_n^{(l)} \Phi_{p,q-1}^{(l)} + \alpha_s^{(l)} \Phi_{p,q+1}^{(l)} + \alpha_y^{(l)} \Phi_{p,q}^{(l)}. \quad (3.133)$$

This leads to the following difference equation which can be solved numerically:

$$\begin{aligned} & \underbrace{-\alpha_w^{(l+1/2)}}_{a'_{p,q}} \Phi_{p-1,q}^{(l+1/2)} + \underbrace{\left\{ -\alpha_x^{(l+1/2)} + \frac{4j\beta}{\Delta z} - \frac{k_0^2}{2} [\varepsilon_r^{(l+1/2)}(p,q) - n_{\text{eff}}^2] \right\}}_{b'_{p,q}} \Phi_{p,q}^{(l+1/2)} \\ & \quad + \underbrace{-\alpha_e^{(l+1/2)}}_{c'_{p,q}} \Phi_{p+1,q}^{(l+1/2)} \\ & = \underbrace{\alpha_n^{(l)} \Phi_{p,q-1}^{(l)} + \left\{ \alpha_y^{(l)} + \frac{4j\beta}{\Delta z} + \frac{k_0^2}{2} [\varepsilon_r^{(l+1/2)}(p,q) - n_{\text{eff}}^2] \right\}}_{d'_{p,q}} \Phi_{p,q}^{(l)} + \alpha_s^{(l)} \Phi_{p,q+1}^{(l)}. \quad (3.134) \end{aligned}$$

Equation (3.134) has the same structure as Equation (3.58), just with different parameters $a_{p,q}$, $b_{p,q}$, $c_{p,q}$, and $d_{p,q}$, which are now functions of p and q , and therefore the first ADI step is

formally equivalent to the two-dimensional semivectorial analysis. Hence, Equation (3.134) can also be represented as a matrix equation similar to Equation (3.85), i.e.

$$\mathbf{T}' \underline{\Phi}^{(l+1/2)} = \underline{d}'. \quad (3.135)$$

The matrix \mathbf{T}' is of size $M_x \times M_x$.

3.3.2 Second ADI Step

The second ADI propagation step is $z + \Delta z/2 \rightarrow z + \Delta z$, or equivalently $l + 1/2 \rightarrow l$. Here, the derivative with respect to y from Equation (3.101) is expressed by the implicit FD expression using the *unknown fields* at $l + 1$, i.e.

$$\alpha_n^{(l+1)} \Phi_{p,q-1}^{(l+1)} + \alpha_s^{(l+1)} \Phi_{p,q+1}^{(l+1)} + \alpha_y^{(l+1)} \Phi_{p,q}^{(l+1)}. \quad (3.136)$$

The derivative with respect to x is written as explicit FD expression using the *known fields* at $l + 1/2$ from the first ADI step, i.e.

$$\alpha_w^{(l+1/2)} \Phi_{p-1,q}^{(l+1/2)} + \alpha_e^{(l+1/2)} \Phi_{p+1,q}^{(l+1/2)} + \alpha_x^{(l+1/2)} \Phi_{p,q}^{(l+1/2)}. \quad (3.137)$$

This results in the following difference equation.

$$\begin{aligned} & \underbrace{-\alpha_n^{(l+1)} \Phi_{p,q-1}^{(l+1)}}_{a''_{p,q}} + \underbrace{\left\{ -\alpha_y^{(l+1)} + \frac{4j\beta}{\Delta z} - \frac{k_0^2}{2} \left[\varepsilon_r^{(l+1/2)}(p,q) - n_{\text{eff}}^2 \right] \right\}}_{b''_{p,q}} \Phi_{p,q}^{(l+1)} - \underbrace{\alpha_s^{(l+1)} \Phi_{p,q+1}^{(l+1)}}_{c''_{p,q}} \\ &= \underbrace{\alpha_w^{(l+1/2)} \Phi_{p-1,q}^{(l+1/2)} + \left\{ \alpha_x^{(l+1/2)} + \frac{4j\beta}{\Delta z} + \frac{k_0^2}{2} \left[\varepsilon_r^{(l+1/2)}(p,q) - n_{\text{eff}}^2 \right] \right\}}_{d''_{p,q}} \Phi_{p,q}^{(l+1/2)} + \alpha_e^{(l+1/2)} \Phi_{p+1,q}^{(l+1/2)}. \end{aligned} \quad (3.138)$$

Like Equation (3.134) from the first ADI step, Equation (3.138) has the same structure as Equation (3.58). Thus, the second ADI step is also equivalent to the two-dimensional semivectorial analysis. Hence, a representation of Equation (3.138) as a tridiagonal matrix equation is also possible, i.e.

$$\mathbf{T}'' \underline{\Phi}^{(l+1)} = \underline{d}''. \quad (3.139)$$

The matrix \mathbf{T}'' is of size $M_y \times M_y$.

3.3.3 Computational Complexity

As already mentioned above, the ADI-BPM splits each propagation step $z \rightarrow z + \Delta z$ into two separate steps $z \rightarrow z + \Delta z/2$ and $z + \Delta z/2 \rightarrow z + \Delta z$. In the first ADI step, the tridiagonal matrix Equation (3.135) of size $M_x \times M_x$ has to be solved M_y times. In the second ADI step Equation (3.139) of size $M_y \times M_y$ has to be solved M_x times.

If the waveguide structure to be analyzed is invariant with respect to the z direction, the so-called Eigenmode Decomposition Method, which will be discussed in Chapter 4, may be more appropriate since it is computational much less complex.

3.4 Accuracy Estimation

3.4.1 Fresnel Approximation

Figure 3.6 shows the relation between wave number k , propagation constant β , and x -directed wave number k_x for a wave travelling with a propagation angle θ_x with respect

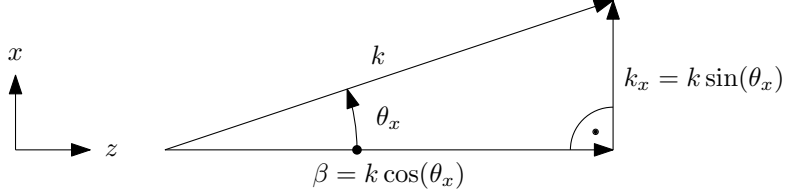


Figure 3.6: Relation between wave number k , z -directed wave number β (propagation constant), x -directed wave number k_x , and propagation angle θ_x with respect to the z direction in the plane $y = 0$.

to the z direction in the plane $y = 0$. According to [9] the Fresnel approximation from Equation (3.44) is a good approximation for the general wide-angle formulation if and only if the propagation angles are so small that

$$\boxed{\cos^2\left(\frac{\theta_x}{2}\right) \approx 1}. \quad (3.140)$$

3.4.2 Spatial Sampling Constraints

In Section 2.3.2 the model for Gaussian beams with some angles θ_x and θ_y with respect to the z direction in the planes $y = 0$ and $x = 0$, respectively, were presented. In the following, $\theta_y = 0$ is assumed without loss of generality, since this can always be achieved by an appropriate rotation of the coordinate system.

The spatial sampling frequency with respect to x is defined as

$$f_s = \frac{M_x}{x_{\max} - x_{\min}}. \quad (3.141)$$

The spatial frequency with respect to x of a beam with an angle θ_x with respect to propagation direction z in the plane $y = 0$ equals

$$f_x = \frac{\sin(\theta_x)}{\lambda}. \quad (3.142)$$

The so-called oversampling factor is defined as

$$\gamma = \frac{f_s}{2f_x} = \frac{\lambda}{2\sin(\theta_x)} \frac{M_x}{x_{\max} - x_{\min}}. \quad (3.143)$$

The spatial sampling frequency has fulfill *Nyquist's sampling criterion* [21]

$$f_s \geq 2f_x, \quad (3.144)$$

or, equivalently, $\gamma \geq 1$.

Figure 3.7 shows the dependency of the spatial period with respect to x on the angle θ_x . It can be seen that the spatial period decreases with increasing θ_x . Figure 3.8 shows which actual angle $\hat{\theta}_x$ a simulated beam has when the angle θ_x is used as setpoint angle. There are two reasons why these two angles are not equal:

- due to a violation of the Fresnel approximation, i.e. the approximation from Equation (3.140) is not fulfilled for the setpoint angle θ_x , and
- due to a small oversampling factor from Equation (3.143).

Figure 3.7 shows that even with a very large oversampling factor of $\gamma = 10$, the actual angle $\hat{\theta}_x$ deviates rather drastically from the setpoint angle if θ_x is large. The conclusion of this figure is, that due to the Fresnel approximation, *beam angles of $\theta_x > 10^\circ$ should be avoided* in BEAMLABBPM simulations because these beams are not approximately paraxial anymore. The Eigenmode Decomposition Method discussed in Chapter 4 does not have this limitation.

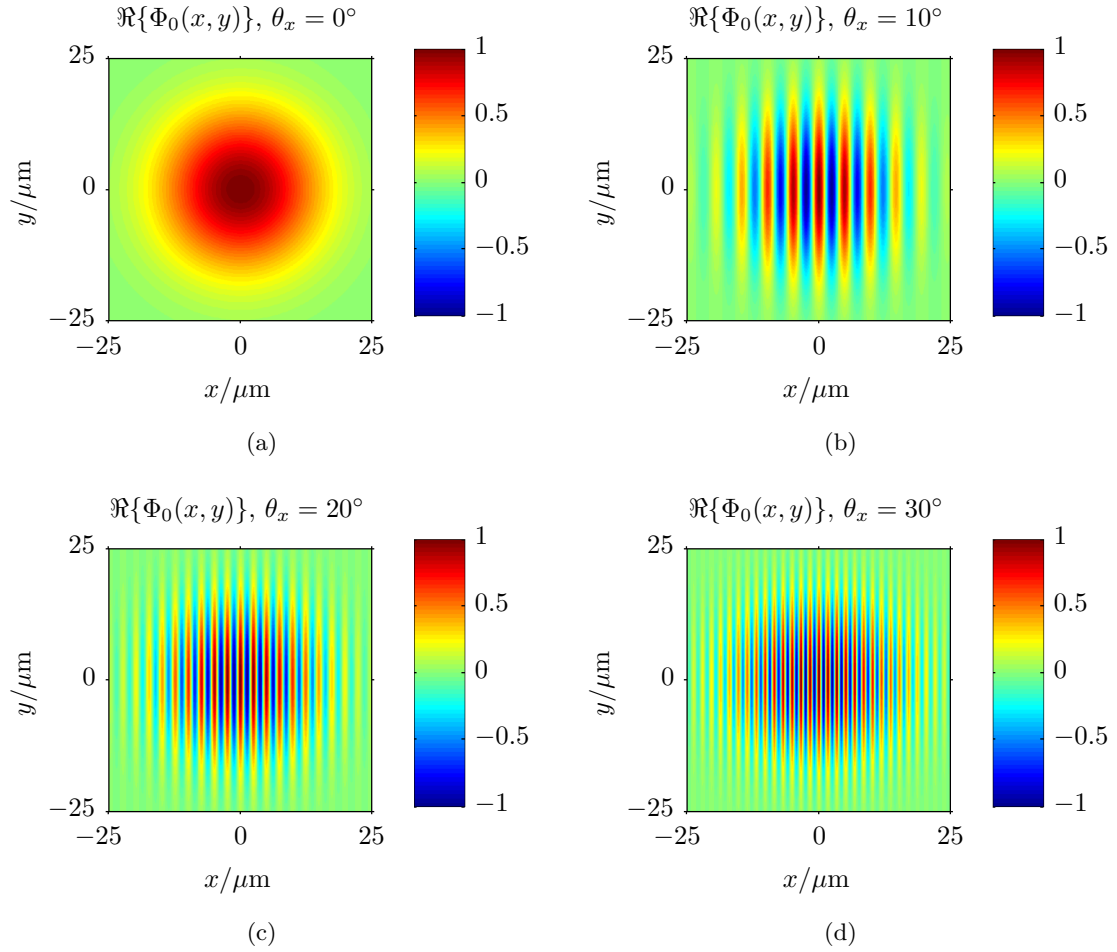


Figure 3.7: $\Re\{\Phi_0(x, y)\}$ for different values of θ_x . The spatial period with respect to x is $1/f_x = \lambda/\sin(\theta_x)$.

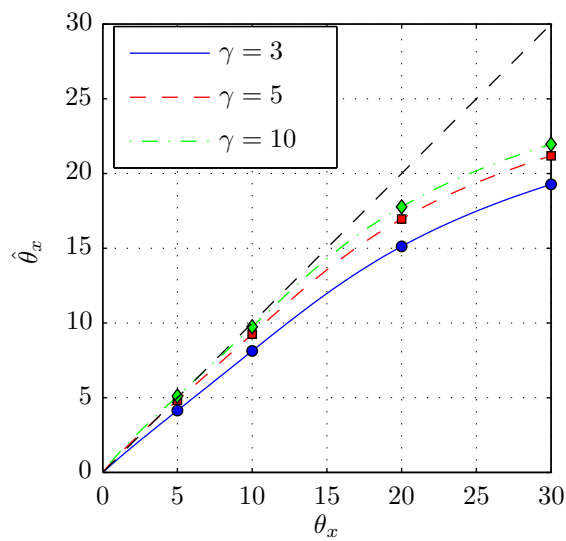


Figure 3.8: Setpoint angles θ_x vs. actual angles $\hat{\theta}_x$ for different oversampling factors γ .

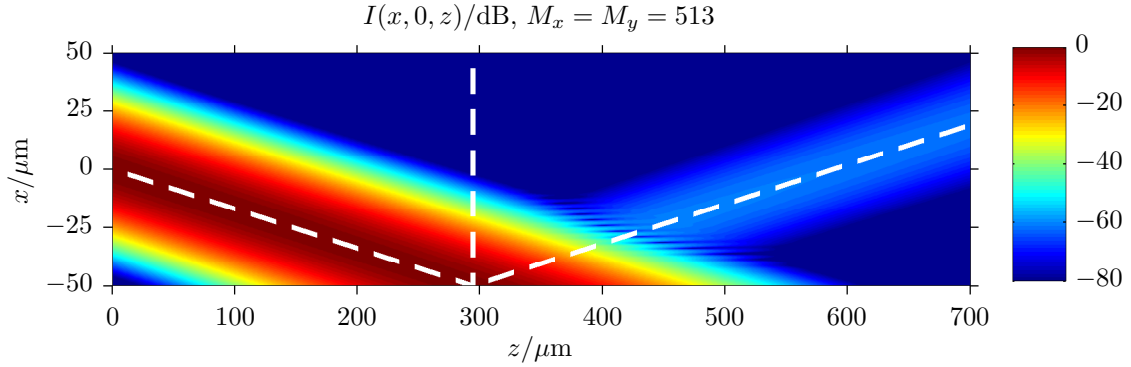


Figure 3.9: Intensity I in the plane $y = 0$ of an incident Gaussian beam ($\theta_x = -10^\circ$, $w_0 = 15 \mu\text{m}$) and the reflected beam.

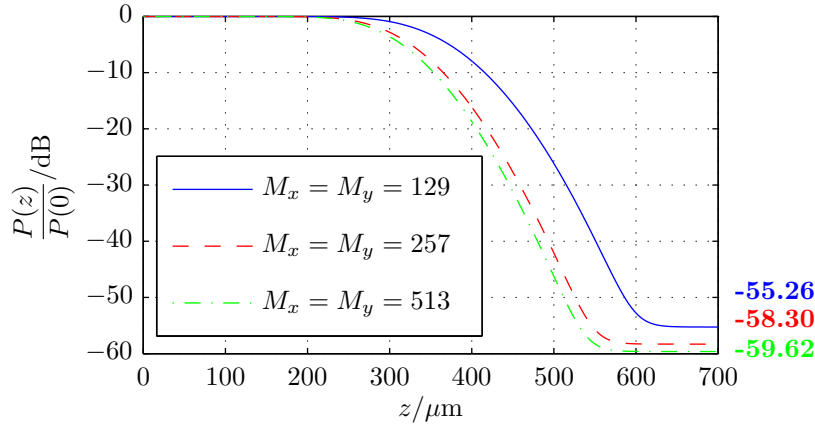


Figure 3.10: Power P in the whole transversal simulation region vs. propagation distance z .

3.4.3 Boundary Reflections

In Figure 3.9 the boundary reflection due to the approximative nature of TBCs from Section 3.2.4 is shown. A Gaussian beam propagates at an angle of $\theta = -10^\circ$ and hits the right simulation boundary at $z = 50 \mu\text{m} / \tan(\theta_x) \approx 284 \mu\text{m}$. Figure 3.10 depicts the power in the whole lateral simulation region as a function of z . For $M_x = M_y = 513$ a total of $P = -59.62 \text{ dB}$ is reflected back into the simulation region. This results in a boundary reflectivity of $R = -59.62 \text{ dB} = 1.09 \cdot 10^{-6}$. This low reflectivity also matches the values found in the literature. [17] Simulations using smaller values of transversal discretization points $M_x = M_y$ show a slightly larger boundary reflectivity. In simulations where most of the input power is guided in a waveguide, these boundary reflections are generally negligible. When waveguide structures are analyzed, in which a large amount of the input power is radiated towards the simulations boundaries, these boundary reflections can reduce the overall simulation accuracy. The Eigenmode Decomposition Method discussed in Chapter 4 does not have this limitation.

3.5 Imaginary Distance Beam Propagation Method

It has been shown that if the paraxial wave equation is modified so that fields travel imaginary distances, the field resulting from an imaginary distance propagation is the fundamental mode of an optical waveguide. [22] Using the FD-BPM the fundamental mode can be obtained within a few propagation steps which shows that the so-called *Imaginary Dis-*

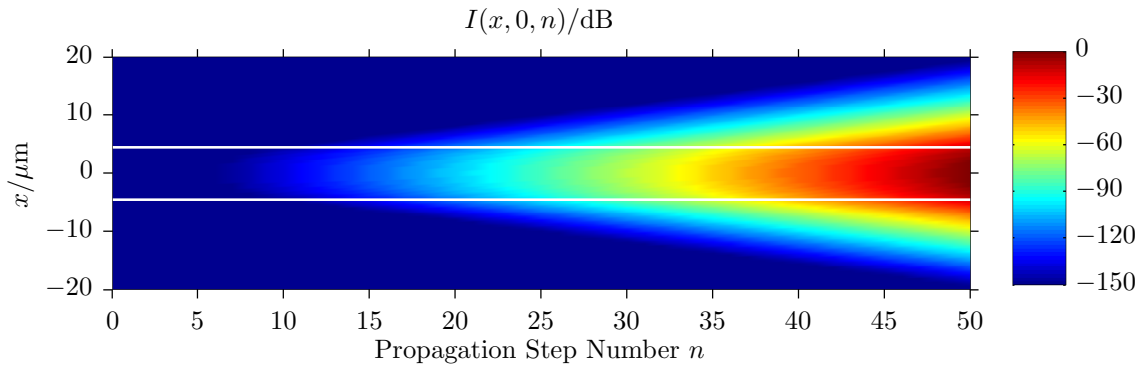


Figure 3.11: Intensity I in the plane $y = 0$ vs. propagation step number n for a step-index circular waveguide using the Imaginary Distance BPM. The input field is a plane wave, i.e. $\Phi_0(x, y) = A_0 = 1$, the initial value of the normalized propagation constant is $B_0 = 0$, and the propagation step size is $\Delta z = 10 \mu\text{m}$.

tance Beam Propagation Method (ID-BPM) is a numerically very efficient way of computing waveguide eigenmodes. Conventional eigenmode calculations require the computation of eigenvalues and eigenvectors of a huge $(M_x M_y) \times (M_x M_y)$ matrix (see Section 4.3). Unfortunately, the simulation result of the ID-BPM usually is the fundamental mode of the waveguide under investigation—higher order modes are difficult to obtain. In principal, it is also possible to compute modes of higher order by using different starting conditions, i.e. input fields $\Phi_0(x, y)$, but the discussion of these techniques is beyond the scope of this text.

The fundamental mode has the largest propagation constant and therefore it sees the most rapid oscillations in phase when traveling down the real axis. The ID-BPM exploits the fact that propagation down the imaginary axis changes these sinusoidal variations in phase into exponential growth in amplitude. A sufficient long imaginary distance propagation gives the fundamental mode—the mode with the most growth. [22]

Figure 3.11 shows the exponential growth in amplitude of the fundamental eigenmode of a circular step-index waveguide with a core radius of $a = 4.5 \mu\text{m}$. Core and cladding refractive index are $n_1 = 1.455$ and $n_2 = 1.450$, respectively. The so-called *normalized propagation constant* of an eigenmode with effective refractive index n_{eff} is defined as [23]

$$B = \frac{n_{\text{eff}}^2 - n_2^2}{n_1^2 - n_2^2}. \quad (3.145)$$

Here, an initial value of the effective refractive index of $n_{\text{eff},0} = n_2 = 1.5$ was chosen, i.e. $B_0 = 0$.

In Figure 3.12 the normalized propagation constant B of the fundamental eigenmode is depicted as a function of the ID-BPM propagation step number. After only $n = 15$ propagation steps, B has already converged sufficiently to its final value—the relative error compared to the exact analytical solution is already smaller than 10^{-6} . For demonstration purposes, the input field of this simulation was a plane wave, i.e. $\Phi_0(x, y) = A_0 = 1$. If a Gaussian field is chosen—which is already very similar to the fundamental Bessel mode of the circular step-index waveguide—the propagating field approaches the fundamental eigenmode even faster. The final value of $B = 0.8412$ is equal to the simulation result using the eigenmode solver BEAMLBEIG (see value of B from eigenmode $V_1(x, y)$ in Figure C.3).

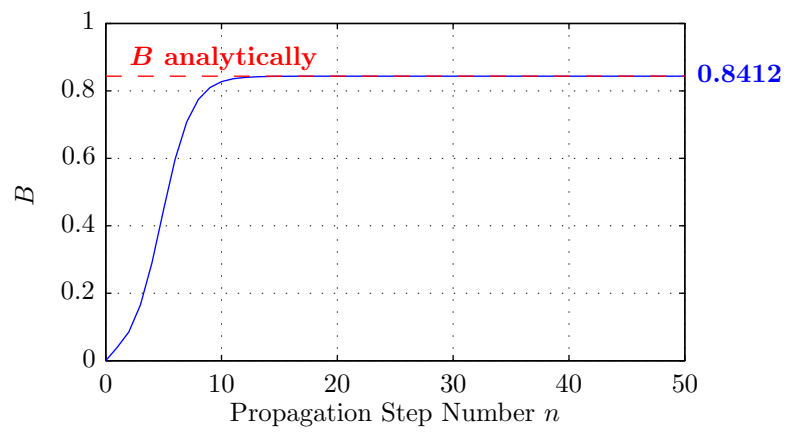


Figure 3.12: Calculated value of the normalized propagation constant B of the fundamental mode at each iteration for the starting conditions $\Phi_0(x, y) = A_0 = 1$ and $B_0 = 0$. The propagation step size is $\Delta z = 10 \mu\text{m}$.

Chapter 4

Eigenmode Decomposition Method

4.1 Introduction and Outline

In this chapter a numerically very efficient method for calculating the throughput of an optical waveguide is presented. This method, called *Eigenmode Decomposition Method*, uses the framework of linear vector spaces to decompose an arbitrary input field into a part which lies within the Hilbert space of eigenmodes and another part which lies in the orthogonal complement of this eigenmode space. Since the throughput of any eigenmode is equal to one and the throughput of any field in the orthogonal complement of the eigenmode space is zero, the throughput can be calculated very efficiently.

This chapter is organized as follows.

- In Section 4.2 the throughput of an optical waveguide is defined.
- In Section 4.3 so-called eigenmodes of optical waveguides are discussed.
- In Section 4.4 the fundamentals of linear vector spaces and orthonormal bases are discussed.
- Section 4.5 combines the concepts of waveguide eigenmodes and linear vector spaces to explain the Eigenmode Decomposition Method.
- Finally, in Section 4.6 two numerical examples of the Eigenmode Decomposition Method are presented.

4.2 Waveguide Throughput

The throughput of an optical waveguide for a given input field $\Phi_0(x, y)$ is defined as the ratio of output power $P_\infty = P(z \rightarrow \infty)$ to input power $P_0 = P(z = 0)$, i.e.

$$\eta(\Phi_0) = \frac{P_\infty}{P_0} = \frac{\int_{-\infty}^{\infty} \int_{-\infty}^{\infty} |\Phi_\infty(x, y)|^2 dx dy}{\int_{-\infty}^{\infty} \int_{-\infty}^{\infty} |\Phi_0(x, y)|^2 dx dy}. \quad (4.1)$$

It is bounded by

$$0 \leq \eta(\Phi_0) \leq 1, \quad (4.2)$$

where when $\eta = 1$ that means all of the input power is guided by the waveguide and when $\eta = 0$ that means all of the input power is radiated.

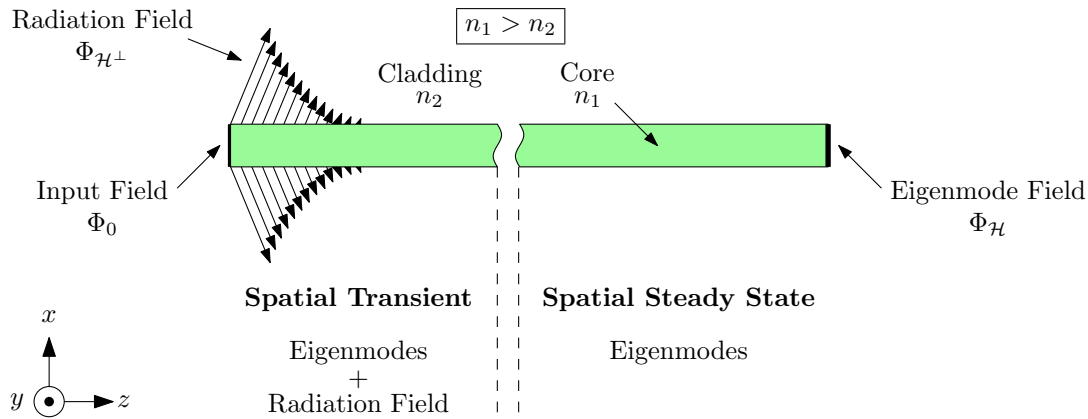


Figure 4.1: Schematic representation of the *spatial transient* and the *spatial steady state*.

One way of computing the throughput numerically is to compute the output power P_{out} at a finite distance $z < \infty$ using the Beam Propagation Method implemented in BEAMLABBPM. This method is not very computationally efficient if the throughput is the only result of interest.

In this chapter a much more efficient method is presented which only requires to compute the waveguide eigenmodes *once* using the eigenmode solver BEAMLAEIG. Once the eigenmodes are known, only N so-called overlap integrals¹ have to be computed, where N is the number of waveguide eigenmodes, in order to compute the throughput.

4.3 Waveguide Eigenmodes

A waveguide eigenmode is a lateral field distribution $V(x, y)$ which does not change during propagation. The number of eigenmodes is finite and depends on the frequency—it generally increases with increasing frequency. The *superposition* of eigenmodes does change during propagation since eigenmodes generally have different propagation constants and therefore different propagation velocities. These different propagation velocities lead to so-called *mode dispersion* which can severely limit the maximum data rates in optical communication systems.

The multi-core waveguide under investigation (see Section 2.2.1) has a total of 51 eigenmodes at a wavelength of $\lambda = 850$ nm which are depicted in Figures A.3–A.5.

In general, not all of the laser output power can be guided by an ideal, i.e. non-absorbing, waveguide—some of the power is radiated within a finite distance from the optical source. This region is called *spatial transient*. Sufficiently far from the optical source, all of the power of the *radiation field* $\Phi_{\mathcal{H}\perp}$ ² is lost to radiation and all of the remaining guided optical power is “contained” within the waveguide eigenmodes. Within this region, the waveguide fields are in a so-called *spatial steady state*. Figure 4.1 depicts this situation schematically. [24] “Spatially steady” does not mean that the field does not change during propagation since, as mentioned above, the superposition of eigenmodes with different propagation constants is not spatially constant. It just means that the power carried by each individual waveguide eigenmode is constant and hence, the total guided power is constant in a non-absorbing waveguide.

¹Overlap integrals will be defined in Section 4.5.

²This nomenclature will be explained in Section 4.5.

4.3.1 Eigenmode Equation

BEAMLABEIG computes the eigenmodes of a waveguide by solving the *eigenmode matrix equation*

$$\mathbf{A}\underline{\Phi} = \beta^2\underline{\Phi}, \quad (4.3)$$

where the scalar quantity β^2 is an eigenvalue of the equation, and the vector $\underline{\Phi}$ is an eigenvector of the equation. The matrix \mathbf{A} has a size of $(M_x M_y) \times (M_x M_y)$, where M_x and M_y are the numbers of lateral discretization points in x and y direction, respectively. The values of the matrix elements of \mathbf{A} depend on the refractive index profile $n(x, y)$, the discretization mesh, and the wavelength λ . A detailed discussion on how to construct the matrix \mathbf{A} is beyond the scope of this text and can be found in [9, 25].

The eigenmode equation is solved in BEAMLABEIG by executing the following MATLAB commands:

```

1 % Compute eigenvalues beta^2 and eigenvectors phi_eigs of matrix A
2 [phi_eigs, beta_square] = eigs(A, k, ...
3     (sqrt(max(max(epsilon_r))) * k0)^2, options);
4
5 % Reshape and permute matrix phi_eigs in order to get correct x and y axes
6 phi_eigs = permute(reshape(phi_eigs, My, Mx, k), [2 1 3]);
7
8 % Effective refractive indices of eigenmodes: neff = beta/k0
9 neff = diag(sqrt(beta_square))/k0;
10 % Normalized propagation constants of eigenmodes
11 B = (neff - n2) / (n1 - n2);

```

Here, in line 2 the variable A contains the matrix \mathbf{A} and k is the number of eigenmodes to be computed. The results of the eigenmode computation are the eigenvectors stored in the columns of the matrix `phi_eigs`, as well as the eigenvalues β^2 stored in the matrix `beta_square`. As already mentioned above, the matrix A has a size of $(M_x M_y) \times (M_x M_y)$, and therefore the execution of the `eigs` function generally requires a rather long computation time. In line 6 the matrix `phi_eigs` is reshaped and permuted in order for the waveguide eigenmodes to be finally stored in a 3-D matrix, which is convenient for further computations.

The eigenmode equation from Equation (4.3) which is solved by BEAMLABEIG has a multitude of solutions, but only some of them are physically meaningful. The necessary condition for a solution of Equation (4.3) to be a waveguide eigenmode is

$$n_2 \leq n_{\text{eff}} \leq n_1, \quad (4.4)$$

where n_{eff} is the effective refractive index which can be computed from the eigenvalues β^2 of the eigenmode equation using Equation (3.40), and n_1 and n_2 are core and cladding refractive index, respectively. The closer n_{eff} is to n_1 , the stronger the spatial confinement of the eigenmode to the core region is. The closer n_{eff} is to n_2 , the more the eigenmode extends into the cladding region.

Using the definition of the normalized propagation constant from Equation (3.145), Equation (4.4) can also be formulated as

$$0 \leq B \leq 1. \quad (4.5)$$

4.3.2 Rotation of Eigenmodes

In general, the solutions of the eigenmode equation from Equation (4.3) are not unique. If the waveguide under investigation is rotationally symmetric, any rotated eigenmode is again an eigenmode.

More generally, if the refractive index profile of the waveguide has a rotational period of $\Delta\varphi$, i.e. $n(r, \varphi) = n(r, \varphi + \Delta\varphi)$, then all rotated eigenmodes $\tilde{V}_n(r, \varphi) = V_n(r, \varphi + \Delta\varphi)$ are again eigenmodes. In order to preserve the orthogonality of the eigenmodes, *all N eigenmodes V_1, \dots, V_N have to be rotated by $\Delta\varphi$* . The rotational period of the multi-core waveguide from Figure 2.1 is $\Delta\varphi = 60^\circ$.

MATLAB's `eigs` function uses a random starting vector for the computation of eigenvalues and corresponding eigenvectors. Hence, the eigenmodes computed by `BEAMLABEIG` are also random, where the randomness lies exactly in the rotation of the eigenmodes. Consecutive eigenmode computation of the same waveguide structure can result in differently rotated eigenmodes each time.

4.4 Linear Vector Spaces and Orthonormal Bases

A linear vector space \mathcal{H} is a set of functions $\Phi(x, y)$ with the following property: If $\Phi_1(x, y) \in \mathcal{H}$ and $\Phi_2(x, y) \in \mathcal{H}$, then $\alpha \Phi_1(x, y) + \beta \Phi_2(x, y) \in \mathcal{H}$. [21]

Inner Product and Norm. The *inner product* of two functions $\Phi_1(x, y)$ and $\Phi_2(x, y)$ is defined as

$$\langle \Phi_1, \Phi_2 \rangle = \int_{-\infty}^{\infty} \int_{-\infty}^{\infty} \Phi_1(x, y) \Phi_2^*(x, y) dx dy. \quad (4.6)$$

The norm³ of a function $\Phi(x, y)$ is defined as

$$\|\Phi\| = \sqrt{\langle \Phi, \Phi \rangle} = \sqrt{\int_{-\infty}^{\infty} \int_{-\infty}^{\infty} |\Phi(x, y)|^2 dx dy}. \quad (4.7)$$

Orthonormal bases. Let $\{V_n(x, y)\}_{n=1,2,\dots,N}$ be a set of orthonormal functions in \mathcal{H} , i.e.

$$\langle V_n, V_m \rangle = \delta_{n,m} = \begin{cases} 1, & n = m \\ 0, & n \neq m \end{cases}, \quad (4.8)$$

where $\delta_{n,m}$ is the so-called *Kronecker delta*. Equation (4.8) implies $\|V_n\| = 1$. A set of orthonormal functions $\{V_n(x, y)\}_{n=1,2,\dots,N}$ is called an *orthonormal basis* for the linear vector space \mathcal{H} , if any function $\Phi(x, y) \in \mathcal{H}$ can be represented as a linear combination of the basis functions V_n . That means that to each $\Phi(x, y) \in \mathcal{H}$ there exist coefficients Φ_n with $n = 1, 2, \dots, N$ such that

$$\Phi(x, y) = \sum_{n=1}^N \Phi_n V_n(x, y) \quad \text{for } \Phi(x, y) \in \mathcal{H}. \quad (4.9)$$

For a given orthonormal basis $\{V_n(x, y)\}_{n=1,2,\dots,N}$ for the vector space \mathcal{H} the coefficients Φ_n from Equation (4.9) are unique for each $\Phi(x, y)$ —they are given by the inner products of $\Phi(x, y)$ with the basis functions $V_n(x, y)$, i.e.

$$\Phi_n = \langle \Phi, V_n \rangle. \quad (4.10)$$

Dimension. The number N of basis functions required is called the *dimension* of the vector space \mathcal{H} . In general, dimension may be infinite. The set of vectors \mathcal{H} that can be reached by all possible linear combinations of basis functions $\{V_n(x, y)\}_{n=1,2,\dots,N}$ is called *span*, i.e.

$$\mathcal{H} = \text{span}\{V_n(x, y)\}_{n=1,2,\dots,N}. \quad (4.11)$$

³A norm which is defined by the inner product as in Equation (4.7) is called *induced norm*.

4.5 Hilbert Space of Eigenmodes

In this section we will discuss waveguide eigenmodes in the framework of linear vector spaces described in the previous section.

All N eigenmodes V_1, V_2, \dots, V_N of an optical waveguide constitute an orthonormal basis of a finite-dimensional Hilbert space \mathcal{H} , i.e.

$$\mathcal{H} = \text{span}(V_1, V_2, \dots, V_N), \quad (4.12)$$

with norm $\|\Phi\|$ and inner product $\langle \Phi_1, \Phi_2 \rangle$ from Equations (4.7) and (4.6), respectively. The waveguide eigenmodes are normalized⁴ in order for the basis to be orthonormal, i.e.

$$\|V_n\|^2 = 1, \quad n = 1, \dots, N. \quad (4.13)$$

The overlap integral of two fields Φ_1 and Φ_2 is defined as

$$\mathcal{O}(\Phi_1, \Phi_2) = \frac{\left| \int_{-\infty}^{\infty} \int_{-\infty}^{\infty} \Phi_1(x, y) \Phi_2^*(x, y) dx dy \right|^2}{\int_{-\infty}^{\infty} \int_{-\infty}^{\infty} |\Phi_1(x, y)|^2 dx dy \int_{-\infty}^{\infty} \int_{-\infty}^{\infty} |\Phi_2(x, y)|^2 dx dy} = \frac{|\langle \Phi_1, \Phi_2 \rangle|^2}{\|\Phi_1\|^2 \|\Phi_2\|^2}. \quad (4.14)$$

Due to the *Cauchy-Schwarz inequality*

$$|\langle \Phi_1, \Phi_2 \rangle| \leq \|\Phi_1\| \|\Phi_2\|, \quad (4.15)$$

the overlap integral from Equation (4.14) is bounded by

$$0 \leq \mathcal{O}(\Phi_1, \Phi_2) \leq 1, \quad (4.16)$$

with $\mathcal{O}(\Phi_1, \Phi_2) = 1$ if and only if the functions $\Phi_1(x, y)$ and $\Phi_2(x, y)$ are “colinear”, i.e. $\Phi_1(x, y) = c \Phi_2(x, y)$ with some constant c .

Theorem 4.5.1 *Any arbitrary input field Φ_0 of an optical waveguide can be decomposed as*

$$\Phi_0 = \Phi_{\mathcal{H}} + \Phi_{\mathcal{H}^\perp}, \quad (4.17)$$

where $\Phi_{\mathcal{H}}$ is the component of Φ_0 which lies in the Hilbert space of eigenmodes \mathcal{H} . $\Phi_{\mathcal{H}}$ can be represented as a linear combination of waveguide eigenmodes V_n , i.e.

$$\Phi_{\mathcal{H}} = \sum_{n=1}^N \langle \Phi_0, V_n \rangle V_n, \quad (4.18)$$

where the analysis relation from Equation (4.10) has been used. $\Phi_{\mathcal{H}^\perp}$ is the component of Φ_0 which lies in \mathcal{H}^\perp , the orthogonal complement of \mathcal{H} and is given by the relation

$$\Phi_{\mathcal{H}^\perp} = \Phi_0 - \Phi_{\mathcal{H}}. \quad (4.19)$$

The field $\Phi_{\mathcal{H}^\perp}$ is orthogonal to all waveguide eigenmodes, i.e.

$$\langle \Phi_{\mathcal{H}^\perp}, V_n \rangle = 0 \quad \text{for } n = 1, \dots, N. \quad (4.20)$$

Figure 4.2 shows the schematic representation of Equation (4.17). $\Phi_{\mathcal{H}}$ lies in the space spanned by the waveguide eigenmodes while $\Phi_{\mathcal{H}^\perp}$ is orthogonal to *any* eigenmode.

⁴The waveguide eigenmode solver BEAMLABEIG internally takes care of this normalization, i.e. Equation (4.13) is always fulfilled for all eigenmodes.

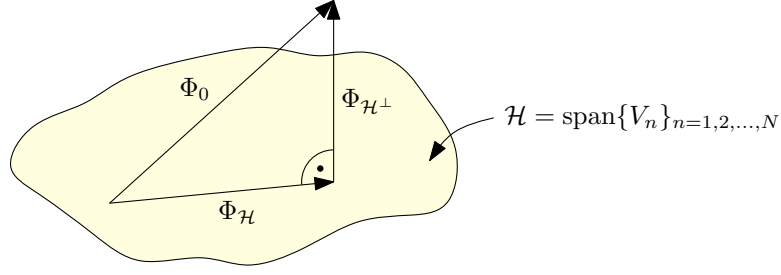


Figure 4.2: Schematic representation of the decomposition $\Phi_0 = \Phi_{\mathcal{H}} + \Phi_{\mathcal{H}^\perp}$.

Theorem 4.5.2 *The throughput of $\Phi_{\mathcal{H}}$ has to be equal to 1 because it is a weighted sum of all eigenmodes of the waveguide, i.e.*

$$\eta(\Phi_{\mathcal{H}}) = \sum_{n=1}^N \mathcal{O}(\Phi_{\mathcal{H}}, V_n) = \sum_{n=1}^N \frac{|\langle \Phi_{\mathcal{H}}, V_n \rangle|^2}{\|\Phi_{\mathcal{H}}\|^2 \|V_n\|^2} = \frac{1}{\|\Phi_{\mathcal{H}}\|^2} \sum_{n=1}^N |\langle \Phi_{\mathcal{H}}, V_n \rangle|^2 = 1, \quad (4.21)$$

where Equation (4.13) has been used. The throughput of $\Phi_{\mathcal{H}^\perp}$ has to be equal to 0 because the inner product of $\Phi_{\mathcal{H}^\perp}$ with any eigenmode vanishes, i.e.

$$\eta(\Phi_{\mathcal{H}^\perp}) = \sum_{n=1}^N \mathcal{O}(\Phi_{\mathcal{H}^\perp}, V_n) = \sum_{n=1}^N \frac{|\langle \Phi_{\mathcal{H}^\perp}, V_n \rangle|^2}{\|\Phi_{\mathcal{H}^\perp}\|^2 \|V_n\|^2} = 0, \quad (4.22)$$

where Equation (4.20) has been used.

Because of Equation (4.22) the throughput of an arbitrary input field can be calculated computationally very efficiently using the following theorem.

Theorem 4.5.3 *The throughput of an arbitrary input field Φ_0 can be calculated by*

$$\boxed{\eta(\Phi_0) = \sum_{n=1}^N \mathcal{O}(\Phi_0, V_n)}. \quad (4.23)$$

Because of Equation (4.16) the throughput bounds from Equation (4.2) are indeed fulfilled.

Theorem 4.5.4 *In a linear waveguide, the output field Φ_{out} at any point in space resulting from the input field $\Phi_0 = \Phi_{\mathcal{H}} + \Phi_{\mathcal{H}^\perp}$ must be equal to the sum of output fields resulting from the separate input fields $\Phi_{\mathcal{H}}$ and $\Phi_{\mathcal{H}^\perp}$, i.e.*

$$\Phi_{\text{out}}(\Phi_0) = \Phi_{\text{out}}(\Phi_{\mathcal{H}}) + \Phi_{\text{out}}(\Phi_{\mathcal{H}^\perp}). \quad (4.24)$$

In the following section Theorems 4.5.1–4.5.4 will be investigated in detail by calculating numerically $\Phi_{\mathcal{H}}$ and $\Phi_{\mathcal{H}^\perp}$ for different input fields Φ_0 and different sets of eigenmodes.

4.6 Examples

4.6.1 Single-Mode Waveguide

In this section a step-index waveguide with a single circular core will be investigated. The so-called *normalized frequency* V is defined as [23]

$$V = ak_0 \text{NA} = ak_0 \sqrt{n_1^2 - n_2^2}, \quad (4.25)$$

Table 4.1: Numerical values of inner products $\langle \Phi_{\text{in}}, V_1 \rangle$ and overlap integrals $\mathcal{O}(\Phi_{\text{in}}, V_1)$ with the only eigenmode V_1 , as well as numerical throughput values $\eta(\Phi_{\text{in}})$ of the fields $\Phi_{\text{in}} = \Phi_0$, $\Phi_{\text{in}} = \Phi_{\mathcal{H}}$, and $\Phi_{\text{in}} = \Phi_{\mathcal{H}^\perp}$.

Φ_{in}	Φ_0	$\Phi_{\mathcal{H}}$	$\Phi_{\mathcal{H}^\perp}$
$\langle \Phi_{\text{in}}, V_1 \rangle$	-2.4076	-2.4076	0.0000
$\mathcal{O}(\Phi_{\text{in}}, V_1)$	0.3275	1.0000	0.0000
$\eta(\Phi_{\text{in}}) = \mathcal{O}(\Phi_{\text{in}}, V_1)$	0.3275	1.0000	0.0000

where NA designates the *numerical aperture* of the waveguide, a is the core radius, and $k_0 = (2\pi)/\lambda_0$ is the wave number in a vacuum. The normalized frequency is chosen to be smaller than the cut-off frequency of the second waveguide eigenmode V_2^5 in order to ensure single-mode operation, i.e. [8]

$$V < V_c = 2.405. \quad (4.26)$$

Here, $V = 2.2$ was chosen.

Simulation Results. Figure 4.3 graphically illustrates the decomposition from Equation (4.17) of a Gaussian LP_{01} input field Φ_0 , as defined in Section 2.3. The radius of the beam waist is $w_0 = 2.10 \mu\text{m}$ and the lateral offset⁶ is $x_{\text{offset}} = 2.5 \mu\text{m}$. Figure 4.4 shows the intensity of the propagating beams for the different input fields Φ_0 , $\Phi_{\mathcal{H}}$, and $\Phi_{\mathcal{H}^\perp}$. Figure 4.4(b) shows that the throughput of $\Phi_{\mathcal{H}}$ is indeed $\eta(\Phi_{\mathcal{H}}) = 1$. Because we have only a single waveguide eigenmode V_1 , the output intensity is moreover *constant* with respect to the z direction. Figure 4.4(c) shows that the throughput of $\Phi_{\mathcal{H}^\perp}$ is $\eta(\Phi_{\mathcal{H}^\perp}) = 0$, i.e. all of the input power is radiated from the waveguide towards the simulation boundaries. Figure 4.4(a) and (d) are virtually identical, which shows that Theorem 4.5.4 holds—Figure 4.4(d) is simply the addition⁷ of the fields from (b) and (c). This sum $\Phi_{\text{out}}(\Phi_{\mathcal{H}}) + \Phi_{\text{out}}(\Phi_{\mathcal{H}^\perp})$ is equal to the field distribution which results from the sum input field $\Phi_0 = \Phi_{\mathcal{H}} + \Phi_{\mathcal{H}^\perp}$.

Figure 4.5 shows the normalized power in the waveguide as a function of z for the input fields Φ_0 , $\Phi_{\mathcal{H}}$, and $\Phi_{\mathcal{H}^\perp}$. Again, it can be seen that Equations (4.21) and (4.22) hold. The throughput of Φ_0 is $\eta(\Phi_0) = 0.33$.

Figure 4.6 depicts the power carried in each waveguide eigenmode as a function of the propagation distance z . Since, per definition, eigenmodes do not change their lateral field distribution during propagation, the power carried in each eigenmode must also be constant with respect to z , i.e.

$$\mathcal{O}(\Phi_z, V_n) = \mathcal{O}(\Phi_0, V_n) \quad \text{for all } z \geq 0. \quad (4.27)$$

Here, we have single-mode operation and therefore all of the power in the eigenmode space \mathcal{H} is contained in the only eigenmode V_1 .

Table 4.1 shows the numerical values of inner products $\langle \Phi_{\text{in}}, V_1 \rangle$ and overlap integrals $\mathcal{O}(\Phi_{\text{in}}, V_1)$ with the only eigenmode V_1 , as well as the numerical throughput values $\eta(\Phi_{\text{in}})$ of the fields $\Phi_{\text{in}} = \Phi_0$, $\Phi_{\text{in}} = \Phi_{\mathcal{H}}$, and $\Phi_{\text{in}} = \Phi_{\mathcal{H}^\perp}$. The field $\Phi_{\mathcal{H}^\perp}$ is orthogonal to the eigenmode V_1 (see Equation (4.20)). Theorems 4.5.1–4.5.3 are all fulfilled by the simulation results.

⁵For a circular step-index waveguide this is the LP_{11} Bessel mode. “Second” refers to a descending ordering of the eigenmodes with respect to the normalized propagation constant B from Equation (3.145).

⁶The definition of the lateral offset is depicted in Figure 5.1.

⁷Please note that Figure 4.4 is represented in a *logarithmic* scale.

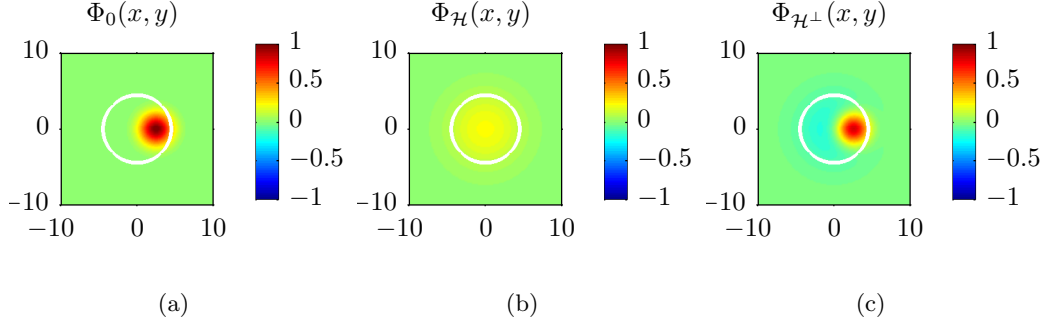


Figure 4.3: Illustration of the decomposition $\Phi_0 = \Phi_{\mathcal{H}} + \Phi_{\mathcal{H}^\perp}$ for a single-mode waveguide with core radius $a = 4.5 \mu\text{m}$ and a Gaussian input field with lateral offset $x_{\text{offset}} = 2.5 \mu\text{m}$. The abscissas and ordinates are all in μm and show x and y coordinates, respectively.

4.6.2 Multi-Mode Waveguide

In this section the same waveguide as in Section 4.6.1 is investigated, but now a normalized frequency of $V = 5$ is used. Hence, $V > V_c = 2.405$ and therefore multiple eigenmodes exist. These eigenmodes are computed in the example in Section C.2 using BEAMLABELIG. There exist a total of $N = 6$ eigenmodes V_1, \dots, V_6 which are depicted in Figure C.3.

Simulation Results. Figure 4.7 graphically illustrates the decomposition from Equation (4.17) for a Gaussian input field Φ_0 . Here, the radius of the beam waist is again $w_0 = 2.10 \mu\text{m}$ and the lateral offset is $x_{\text{offset}} = 4.5 \mu\text{m}$. Figure 4.8 shows the spatial intensity distribution for the beams resulting from the three input fields Φ_0 , $\Phi_{\mathcal{H}}$, and $\Phi_{\mathcal{H}^\perp}$. Like in Subsection 4.6.1, the throughput of $\Phi_{\mathcal{H}}$ is $\eta(\Phi_{\mathcal{H}}) = 1$, while the throughput of $\Phi_{\mathcal{H}^\perp}$ is $\eta(\Phi_{\mathcal{H}^\perp}) = 0$. Figures 4.8(a) and (d) show again that Theorem 4.5.4 is fulfilled for these simulations.

Figure 4.9 depicts the normalized power of the propagating beam as a function of z for the three input fields Φ_0 , $\Phi_{\mathcal{H}}$, and $\Phi_{\mathcal{H}^\perp}$. The throughput of Φ_0 is $\eta(\Phi_0) = 0.57$.

Figure 4.10 shows how the power in the eigenmode space \mathcal{H} is distributed between the $N = 6$ waveguide eigenmodes. Each color represents the power contained in one of the eigenmodes. Again, the overlap integrals $\mathcal{O}(\Phi_z, V_n)$ and therefore the power carried in each of the eigenmodes is constant with respect to z .

Table 4.2 shows the numerical values of inner products and overlap integrals with all eigenmodes V_1, \dots, V_6 , as well as the throughput for the three fields Φ_0 , $\Phi_{\mathcal{H}}$, and $\Phi_{\mathcal{H}^\perp}$. Theorem 4.5.2 is fulfilled, i.e. $\eta(\Phi_{\mathcal{H}}) = 1$ and $\eta(\Phi_{\mathcal{H}^\perp}) = 0$. Equation (4.20) is also fulfilled, i.e. $\Phi_{\mathcal{H}^\perp}$ is orthogonal to all waveguide eigenmodes. $\langle \Phi_{\text{in}}, V_5 \rangle = 0$ since $V_5(x, y)$ is an odd function for a fixed value of x (see Figure C.3) and $\Phi_0(x, y)$ is an even function for a fixed value of x (see Figure 4.7).

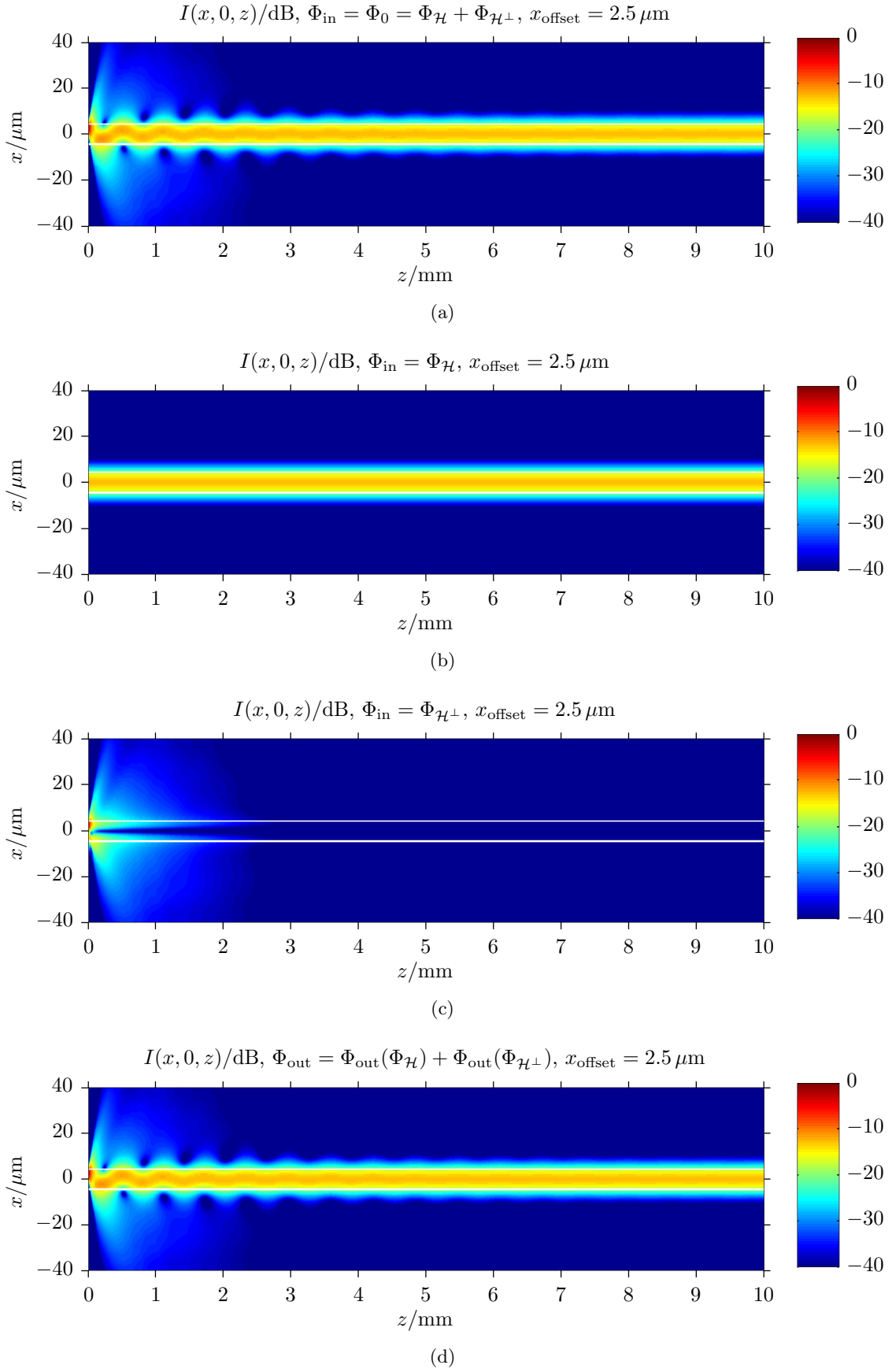


Figure 4.4: Intensity I in the plane $y = 0$ of the beams propagating in a single-mode waveguide for the input fields Φ_0 , $\Phi_{\mathcal{H}}$, and $\Phi_{\mathcal{H}^\perp}$. Here, $x_{\text{offset}} = 2.5 \mu\text{m}$.

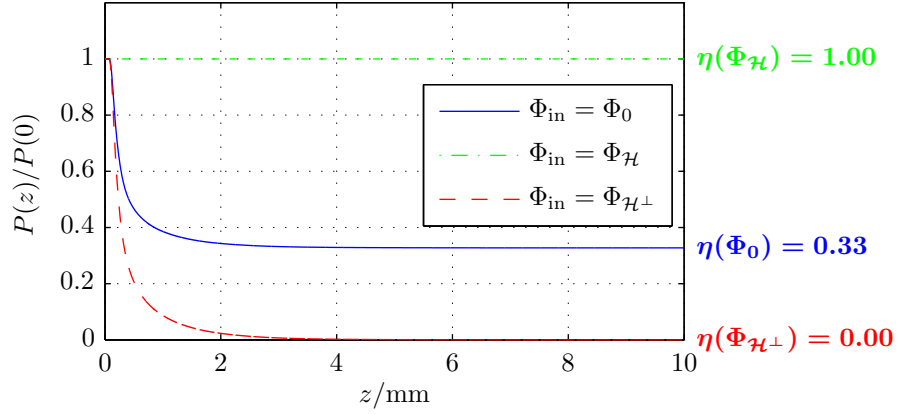


Figure 4.5: Normalized power P in a circular area with radius $20\ \mu\text{m}$ vs. propagation distance z for the input fields Φ_0 , $\Phi_{\mathcal{H}}$, and $\Phi_{\mathcal{H}^\perp}$ and a single-mode waveguide.

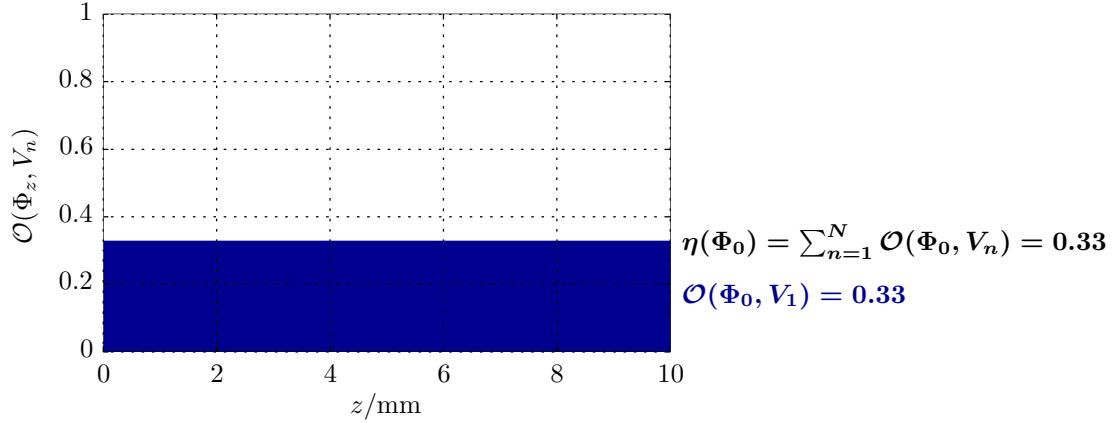


Figure 4.6: The dark blue bar represents the power $\mathcal{O}(\Phi_z, V_1)$ carried in the only waveguide eigenmode V_1 at propagation distance z . Since there is only $N = 1$ eigenmode, this is equal to the throughput, i.e. $\eta(\Phi_0) = \mathcal{O}(\Phi_0, V_n)$ due to Equation (4.27).

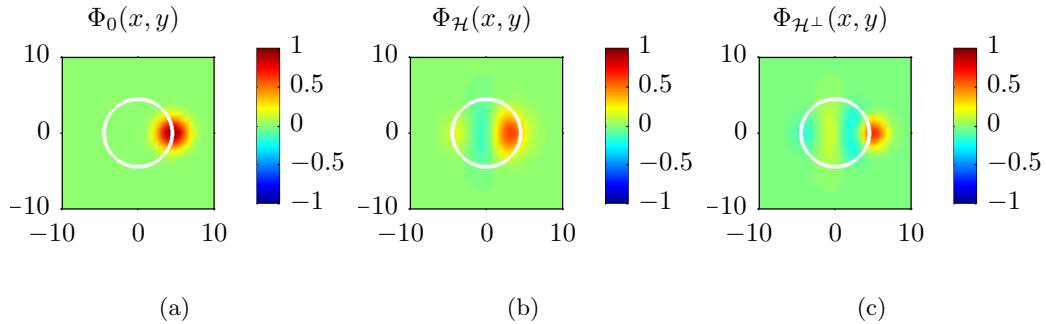


Figure 4.7: Illustration of the decomposition $\Phi_0 = \Phi_{\mathcal{H}} + \Phi_{\mathcal{H}^\perp}$ for a multi-mode waveguide with core radius $a = 4.5\ \mu\text{m}$ and a Gaussian input field with lateral offset $x_{\text{offset}} = 4.5\ \mu\text{m}$. The abscissas and ordinates are all in μm and show x and y coordinates, respectively.

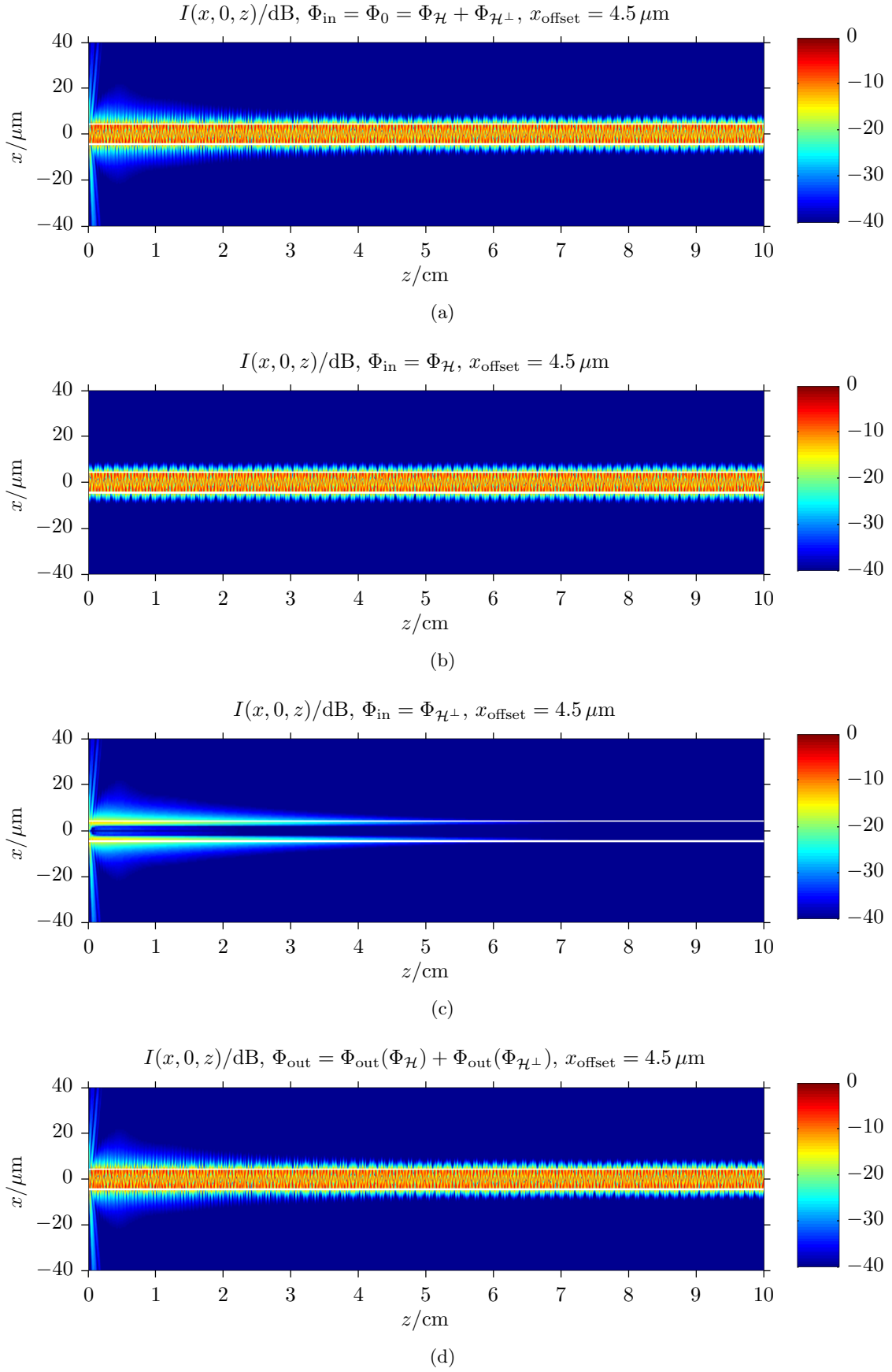


Figure 4.8: Intensity I in the plane $y = 0$ of the beams propagating in a multi-mode waveguide for the input fields Φ_0 , $\Phi_{\mathcal{H}}$, and $\Phi_{\mathcal{H}^\perp}$. Here, $x_{\text{offset}} = 2.5 \mu\text{m}$.

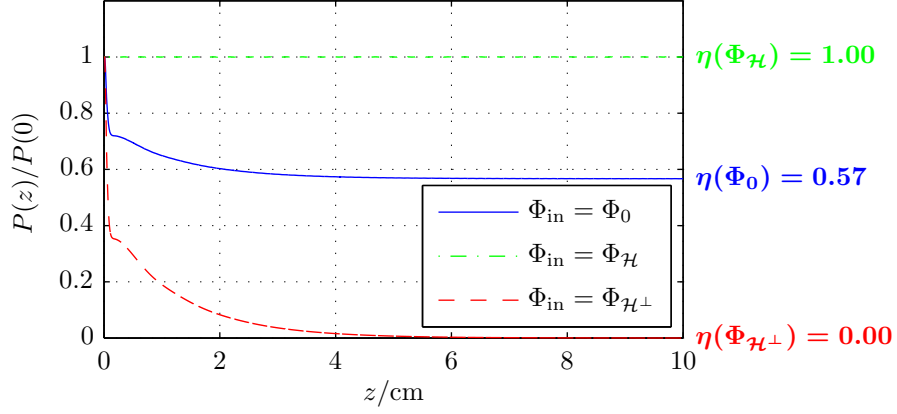


Figure 4.9: Normalized power P in a circular area with radius $20 \mu\text{m}$ vs. propagation distance z for the input fields Φ_0 , $\Phi_{\mathcal{H}}$, and $\Phi_{\mathcal{H}^\perp}$ and a multi-mode waveguide.

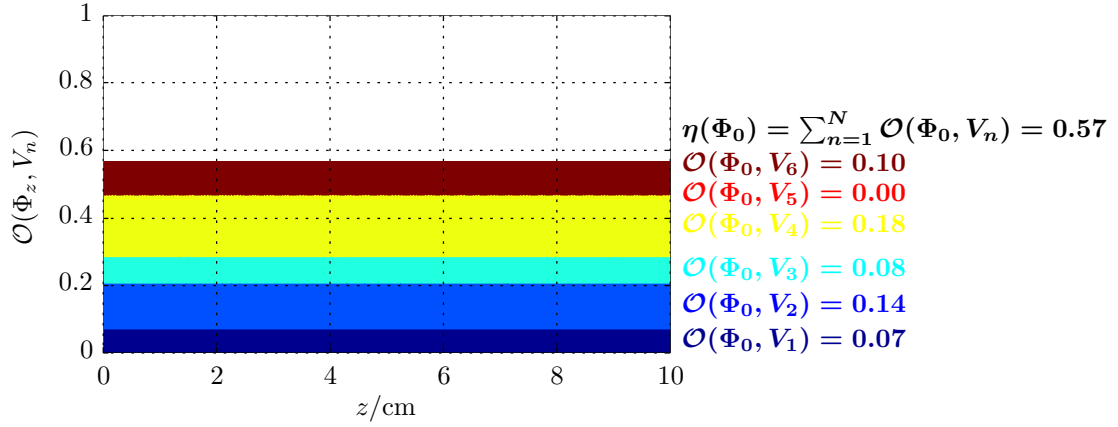


Figure 4.10: Each color represents the power $\mathcal{O}(\Phi_z, V_n)$ carried in one of the $N = 6$ waveguide eigenmodes V_n at propagation distance z . The sum of these powers is the throughput, i.e. $\eta(\Phi_0) = \sum_{n=1}^N \mathcal{O}(\Phi_0, V_n)$ due to Equation (4.27).

Table 4.2: Numerical values of inner products $\langle \Phi_{\text{in}}, V_n \rangle$ and overlap integrals $\mathcal{O}(\Phi_{\text{in}}, V_n)$ with all $N = 6$ eigenmodes V_1, \dots, V_6 , as well as numerical throughput values $\eta(\Phi_{\text{in}})$ of the fields $\Phi_{\text{in}} = \Phi_0$, $\Phi_{\text{in}} = \Phi_{\mathcal{H}}$, and $\Phi_{\text{in}} = \Phi_{\mathcal{H}^\perp}$.

Φ_{in}	Φ_0	$\Phi_{\mathcal{H}}$	$\Phi_{\mathcal{H}^\perp}$
$\langle \Phi_{\text{in}}, V_1 \rangle$	1.1365	1.1365	0.0000
$\langle \Phi_{\text{in}}, V_2 \rangle$	1.5516	1.5516	0.0000
$\langle \Phi_{\text{in}}, V_3 \rangle$	1.1687	1.1687	0.0000
$\langle \Phi_{\text{in}}, V_4 \rangle$	1.7972	1.7972	0.0000
$\langle \Phi_{\text{in}}, V_5 \rangle$	0.0000	0.0000	0.0000
$\langle \Phi_{\text{in}}, V_6 \rangle$	1.3178	1.3178	0.0000
$\mathcal{O}(\Phi_{\text{in}}, V_1)$	0.0730	0.1288	0.0000
$\mathcal{O}(\Phi_{\text{in}}, V_2)$	0.1360	0.2400	0.0000
$\mathcal{O}(\Phi_{\text{in}}, V_3)$	0.0772	0.1361	0.0000
$\mathcal{O}(\Phi_{\text{in}}, V_4)$	0.1825	0.3220	0.0000
$\mathcal{O}(\Phi_{\text{in}}, V_5)$	0.0000	0.0000	0.0000
$\mathcal{O}(\Phi_{\text{in}}, V_6)$	0.0981	0.1731	0.0000
$\eta(\Phi_{\text{in}}) = \sum_{n=1}^6 \mathcal{O}(\Phi_{\text{in}}, V_n)$	0.5668	1.0000	0.0000

Chapter 5

Throughput of Multi-Core Waveguides

5.1 Introduction and Outline

This chapter contains simulation results of the multi-core waveguide structure from Chapter 2. Here, the main parameter of interest is the throughput, i.e. the ratio of output power at $z \rightarrow \infty$ and input power at $z = 0$ defined in Equation (4.1).

The chapter is organized as follows.

- In Section 5.2 the throughput is computed for different lateral misalignments with respect to the the x and y directions.
- In Section 5.3 the dependence of throughput on an angular laser misalignment is investigated.
- Section 5.4 discusses how the throughput is related to the relative refractive index difference between waveguide core and cladding.
- Finally, in Section 5.5 the throughput of different VCSEL modes is investigated.

5.2 Lateral Laser Misalignment

5.2.1 Deterministic Lateral Misalignment

As already mentioned in Section 1, it is very difficult to perfectly align laser and waveguide when inscribing the waveguide using the TPA process—in fact this problem was the main motivation to use multi-core structures in the first place. In this subsection the throughput of the multi-core waveguide structure is analyzed for different lateral misalignments x_{offset} and y_{offset} of the input field $\Phi_0(x, y)$ with respect to the x and y directions. Figure 5.1 shows the definition of these lateral offsets. In this subsection *deterministic* lateral misalignments are investigated. This means that the lateral misalignments of the input fields have deterministic values and the throughput has a deterministic value for each simulation. In the next subsection a *stochastic* lateral misalignment model is discussed, where the *average* throughput for a given probability density function of the lateral laser misalignment is evaluated.

Figure 5.2 shows the spatial intensity distributions of beams with different lateral laser misalignments x_{offset} . For $x_{\text{offset}} = 12.5 \mu\text{m}$ the throughput is much smaller than for $x_{\text{offset}} = 0 \mu\text{m}$ and $x_{\text{offset}} = 25 \mu\text{m}$.

Figure 5.3 depicts the power in a circular area of radius $50 \mu\text{m}$ beam as a function of the propagation distance z . For all three lateral laser misalignments, this power converges

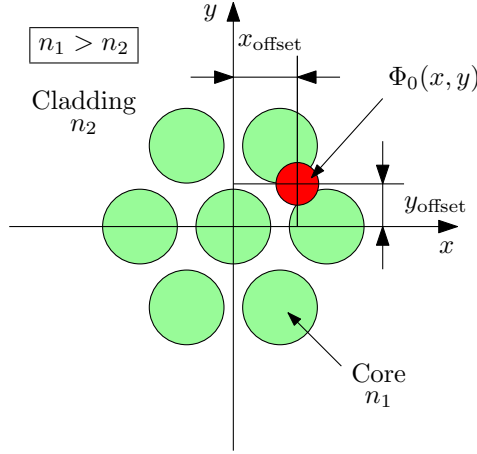


Figure 5.1: Definition of lateral offsets x_{offset} and y_{offset} with respect to the x and y direction, respectively.

to a final value after a sufficient large propagation distance, i.e. the power of the radiation field in the spatial transient from Figure 4.1 has decayed to zero.

Figure 5.4 shows the throughput η as a function of the lateral laser misalignments x_{offset} and y_{offset} . The throughput is much smaller when the lateral misalignment is in y direction, i.e. $x_{\text{offset}} = 0$ and $y_{\text{offset}} \neq 0$. Figure 5.4 also compares the throughput of the multi-core waveguide with the throughput of a single-core waveguide. If the lateral misalignment is in y direction, the difference in throughput between single-core and multi-core waveguide is rather small. On the other hand, if the lateral misalignment is in x direction, i.e. $x_{\text{offset}} \neq 0$ and $y_{\text{offset}} = 0$, this difference is much larger, especially at $x_{\text{offset}} = 25 \mu\text{m}$ where one of the cores of the multi-core waveguide is located.

Figures 5.5 and 5.6 show the throughput of a multi-core waveguide and a single-core waveguide, respectively, as a function of *both* lateral laser misalignment directions x_{offset} and y_{offset} . These simulation results are a prerequisite for the stochastic throughput computations in the next subsection. Figures 5.5 is very similar to Figure 2.1(c), where the refractive index profile of the multi-core waveguide is shown—the throughput indeed has a maximum if the values of the lateral offsets x_{offset} and y_{offset} fulfill the equations

$$x_{\text{offset}} = x_k \quad \text{for } k = 1, \dots, K, \quad (5.1)$$

$$y_{\text{offset}} = y_l \quad \text{for } l = 1, \dots, K, \quad (5.2)$$

where x_k and y_l are the x and y coordinates of the centers of the multi-core waveguide cores from Table 2.1.

5.2.2 Stochastic Lateral Misalignment

Since the actual laser misalignment is unknown, it makes sense to model it as a random variable and calculate the *average throughput* $\bar{\eta}$. Here, we will assume that the lateral offset is a *jointly Gaussian* continuous 2-D real random variable $(X, Y) \sim \mathcal{N}(\mu_X, \mu_Y, \sigma_X^2, \sigma_Y^2, \rho)$. With a slight abuse of notation we use X and Y instead of X_{offset} and Y_{offset} . The probability density function (pdf) of (X, Y) is given by [26]

$$f_{X,Y}(x, y) = \frac{1}{2\pi\sigma_X\sigma_Y\sqrt{1-\rho^2}} \exp \left\{ -\frac{1}{2(1-\rho^2)} \left[\frac{(x-\mu_X)^2}{\sigma_X^2} - 2\rho\frac{(x-\mu_X)(y-\mu_Y)}{\sigma_X\sigma_Y} + \frac{(y-\mu_Y)^2}{\sigma_Y^2} \right] \right\}, \quad (5.3)$$

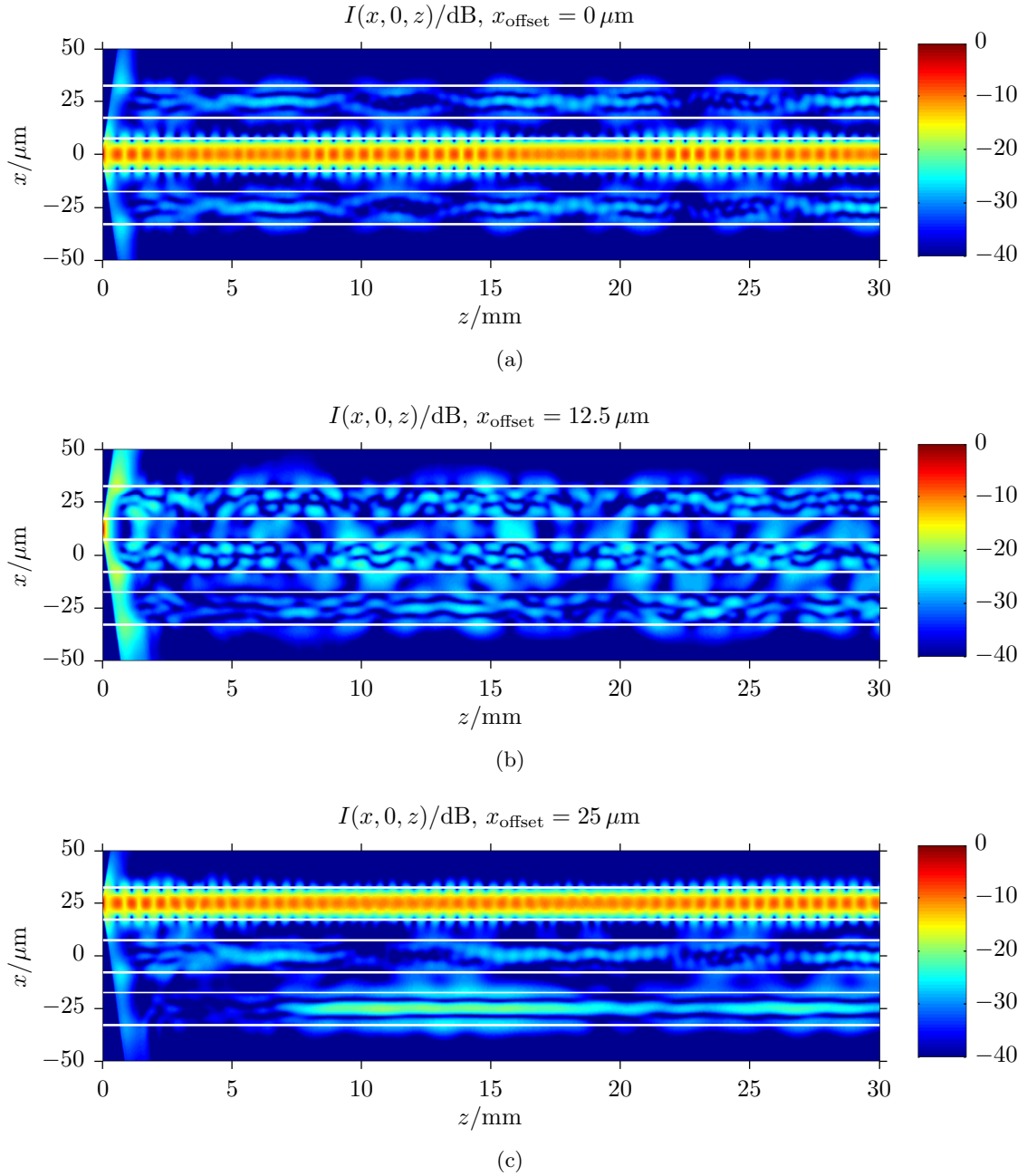


Figure 5.2: Intensity I in the plane $y = 0$ of beams propagating in a multi-core waveguide for different values lateral laser misalignment x_{offset} .

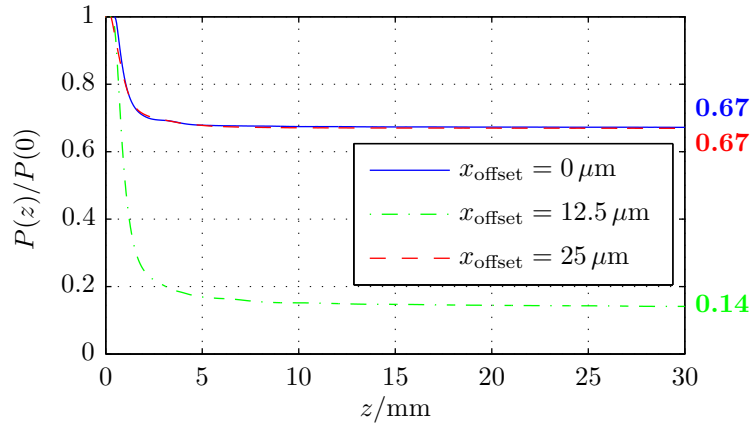


Figure 5.3: Normalized power $P(z)/P(0)$ in a circular area of radius $50 \mu\text{m}$ vs. propagation distance z for different values of lateral laser misalignment x_{offset} .

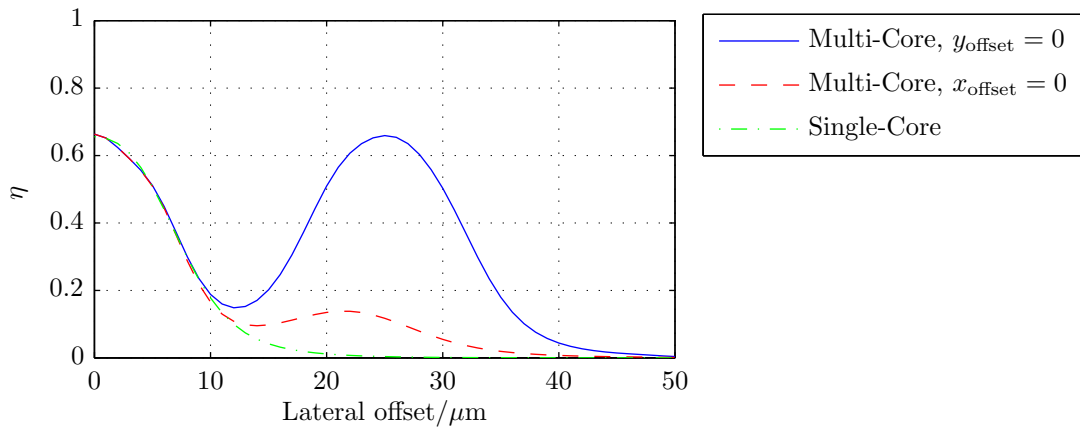


Figure 5.4: Throughput η vs. lateral laser misalignment in x direction ($y_{\text{offset}} = 0$) and in y direction ($x_{\text{offset}} = 0$).

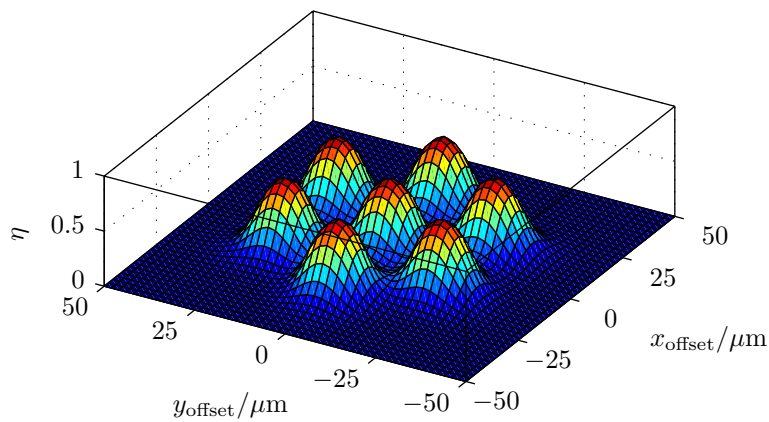


Figure 5.5: Throughput η vs. lateral laser misalignment x_{offset} and y_{offset} in *both* lateral directions x and y for a multi-core waveguide.

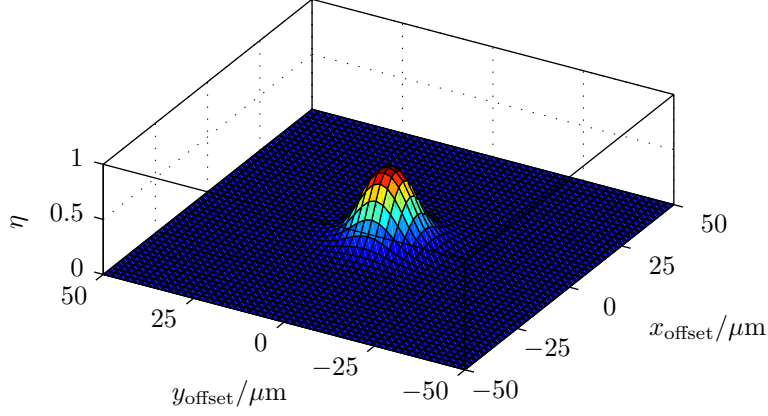


Figure 5.6: Throughput η vs. lateral laser misalignment x_{offset} and y_{offset} in *both* lateral directions x and y for a single-core waveguide.

where $\rho = \rho_{X,Y}$ represents the correlation coefficient and μ_X , μ_Y , σ_X^2 , and σ_Y^2 are the means and variances of the 1-D random variables X and Y . Here, we assume that X and Y are uncorrelated, i.e. $\rho = \rho_{X,Y} = 0$. Equation (5.3) then simplifies to

$$f_{X,Y}(x, y) = \frac{1}{2\pi\sigma_X\sigma_Y} \exp \left\{ -\frac{1}{2} \left[\frac{(x - \mu_X)^2}{\sigma_X^2} + \frac{(y - \mu_Y)^2}{\sigma_Y^2} \right] \right\}. \quad (5.4)$$

If we furthermore assume that X and Y are zero-mean, i.e. $\mu_X = \mu_Y = 0$, and with identical variance $\sigma_X^2 = \sigma_Y^2 = \sigma^2$, Equation (5.4) further simplifies to

$$f_{X,Y}(x, y) = \frac{1}{2\pi\sigma^2} \exp \left(-\frac{x^2 + y^2}{2\sigma^2} \right). \quad (5.5)$$

Here, the only unknown parameter remaining is σ^2 . Figure 5.7 shows the dependence of the average throughput $\bar{\eta}$ on the standard deviation $\sigma = \sqrt{\sigma^2}$. It is evident that for $\sigma \rightarrow 0$ the average throughput equals the *deterministic* throughput with $x_{\text{offset}} = y_{\text{offset}} = 0$, i.e. $\bar{\eta} \rightarrow 0.67$ (see Figures 5.3 and 5.4). Unfortunately, the actual manufacturing tolerances are unknown but realistic state of the art values are somewhere between $\sigma = 10 \mu\text{m}$ and $\sigma = 20 \mu\text{m}$. Therefore the average throughput will be between 20% and 30%. Under these assumptions, the average throughput of a multi-core waveguide is between 10% and 15% larger than the average throughput of a *single-core* waveguide.

The average throughput of a multi-core waveguide is between

$$\boxed{20\% \leq \bar{\eta} \leq 30\%}, \quad (5.6)$$

which is only 10% to 15% larger than the throughput of a single-core waveguide.

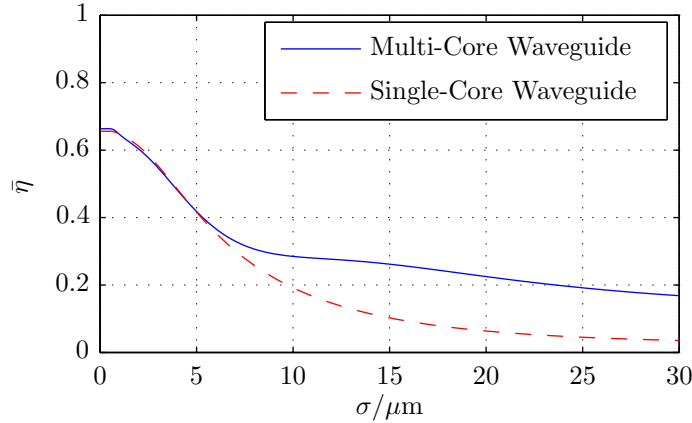


Figure 5.7: Average throughput $\bar{\eta}$ vs. standard deviation σ of the jointly Gaussian random variable (X, Y) .

5.3 Angular Laser Misalignment

In this section we will discuss the influence of the throughput on an angular laser misalignment. Figure 5.8 shows the definition of the angular offset θ_x with respect to the z direction in the plane $y = 0$.

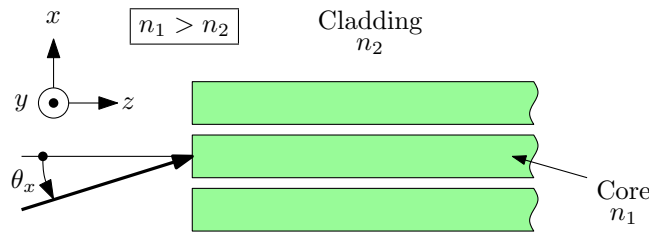


Figure 5.8: Definition of angular offset θ_x with respect to the z direction in the plane $y = 0$.

Figure 5.9 shows the intensity of a propagating beam for the misalignment angles $\theta_x = 5^\circ$ and $\theta_x = 10^\circ$. When comparing Figures 5.9a and 5.9b to Figure 5.2a where $\theta_x = 0^\circ$, it can be seen that there is a significant amount of optical power radiated towards the simulation boundaries within the first few millimeters. Evidently, this is directly related to a reduced throughput. Figure 5.10 shows the normalized power of the propagating beam as a function of the propagation distance z . The normalized power has sufficiently converged to the final throughput value at about $z = 5$ mm.

Figure 5.11 shows the throughput as a function of the misalignment angle θ_x for different additional lateral misalignments x_{offset} and x_{offset} . *Angles of the emitted laser beam should not be larger than $\theta_x > 5^\circ$. A combination of lateral and angular misalignments can severely reduce the throughput.*

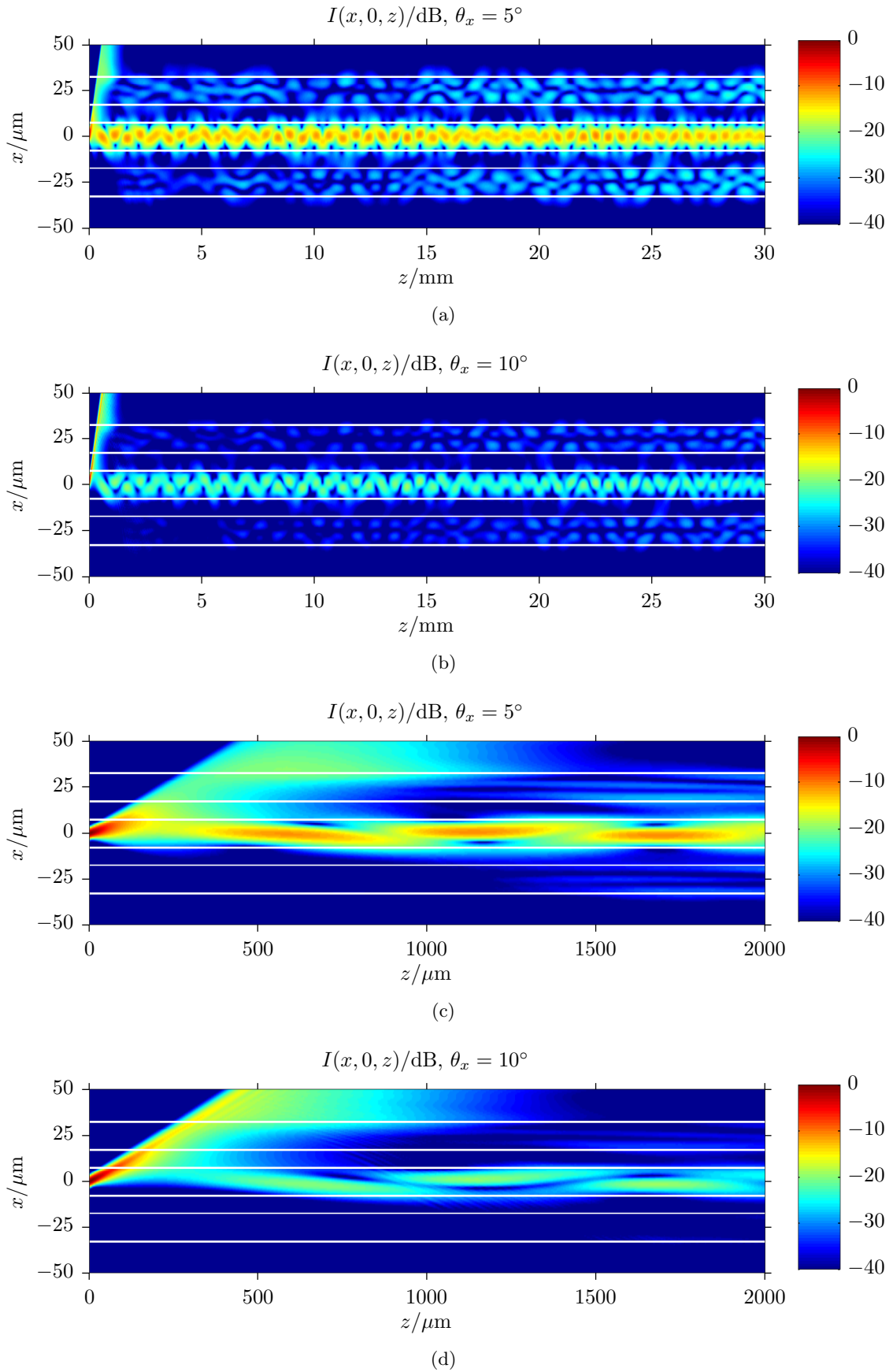


Figure 5.9: Intensity I in the plane $y = 0$ of beams propagating in a multi-core waveguide with $x_{\text{offset}} = 0 \mu\text{m}$ and different values of the misalignment angle θ_x . (c) and (d) show details of (a) and (b), respectively.

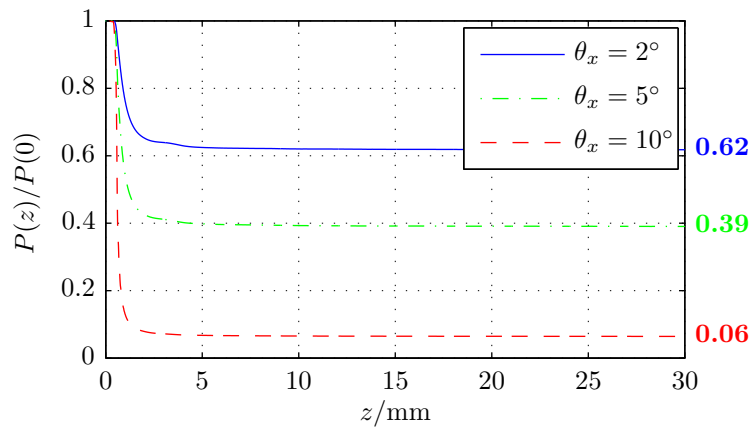


Figure 5.10: Normalized power $P(z)/P(0)$ in a circular area of diameter $50\ \mu\text{m}$ vs. propagation distance z for different values of angular laser misalignment θ_x .

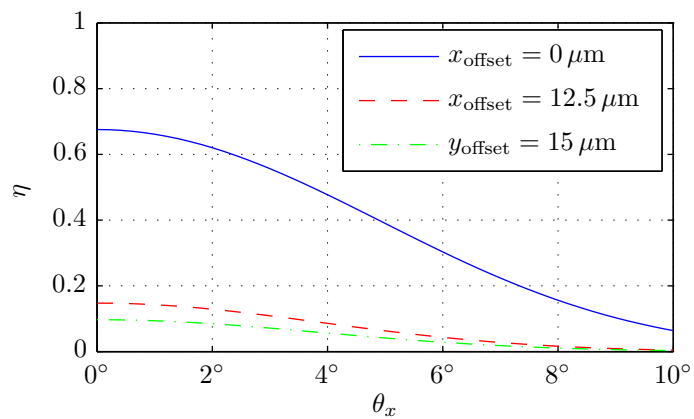


Figure 5.11: Throughput η vs. angular laser misalignment θ_x .

5.4 Dependence of Throughput on Core Refractive Index

In this section the dependence of the throughput on the relative refractive index difference is investigated.

The *relative refractive index difference* is given by [23]

$$\Delta = \frac{n_1^2 - n_2^2}{2n_1^2} \approx \frac{n_1 - n_2}{n_1}. \quad (5.7)$$

The approximation in Equation (5.7) is valid if $n_1 \approx n_2$, i.e. the waveguide structure is *weakly guiding*—then $n_2 \approx n_1(1 - \Delta)$ and $\Delta \ll 1$.

Figure 5.12 shows the refractive index profile of the multi-core waveguide for different values of Δ . The default waveguide considered until now has as core refractive index of $n_1 = 1.5180$ (see Table 2.2), which according to Equation (5.7) corresponds to $\Delta \approx 0.2\%$. In Figure 5.13 the intensity of the propagating beam is depicted for different values of the refractive index difference Δ . The throughput increases with increasing refractive index difference. Figure 5.14 shows that the final output powers are reached after a few millimeters of propagation. A waveguide with a refractive index difference of $\Delta = 1.0\%$ has virtually no losses, i.e. a throughput of $\eta \approx 1$ for an input field with no lateral or angular misalignment.

In Figure 5.15 the throughput as a function of Δ is shown. As already mentioned above, *the throughput increases with increasing refractive index difference. This could explain the temperature dependence of photocurrents measured at the institute—if the refractive index difference increases with increasing temperature, so does the throughput.*

Figure 5.16 shows the dependence of the number of multi-core eigenmodes computed using BEAMLABEL on the relative refractive index difference Δ . The number of eigenmodes increases approximately linear with increasing refractive index difference.

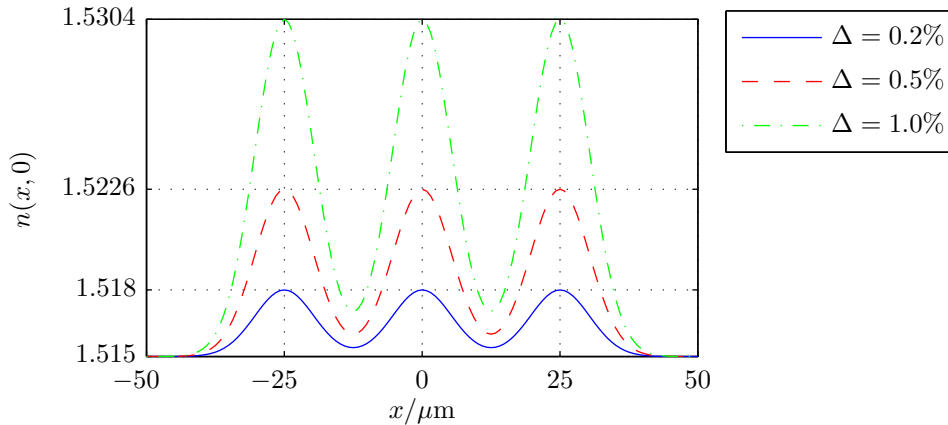


Figure 5.12: Refractive index profile of the multi-core waveguide for different values of the relative refractive index difference Δ .

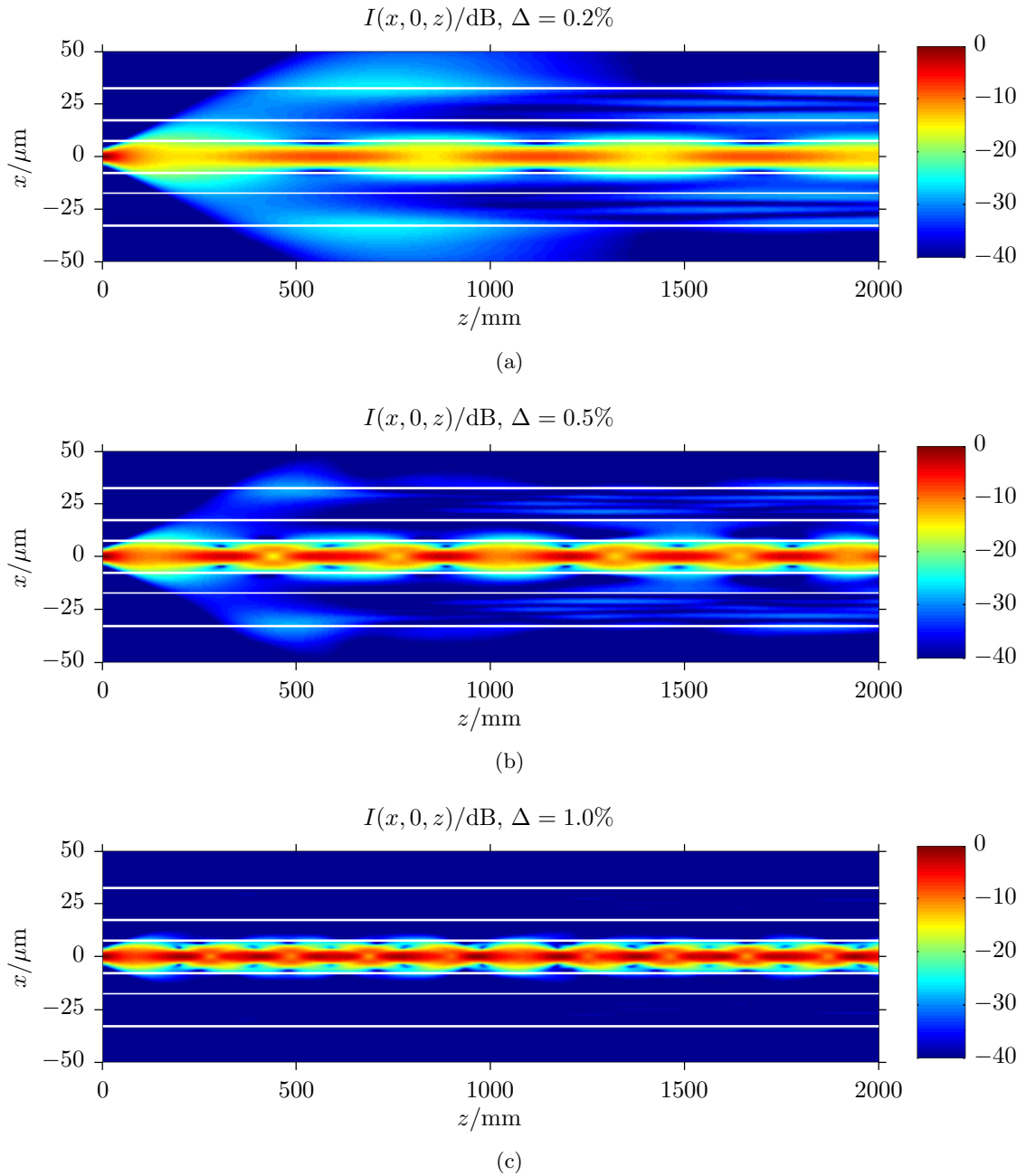


Figure 5.13: Intensity I in the plane $y = 0$ of beams propagating in a multi-core waveguide for different values of the refractive index difference Δ .

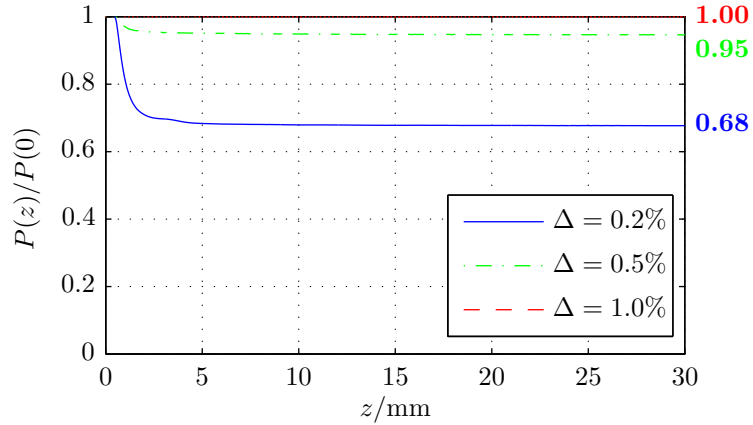


Figure 5.14: Normalized power $P(z)/P(0)$ in a circular area of diameter $50\ \mu\text{m}$ vs. propagation distance z for different values of the refractive index difference Δ .

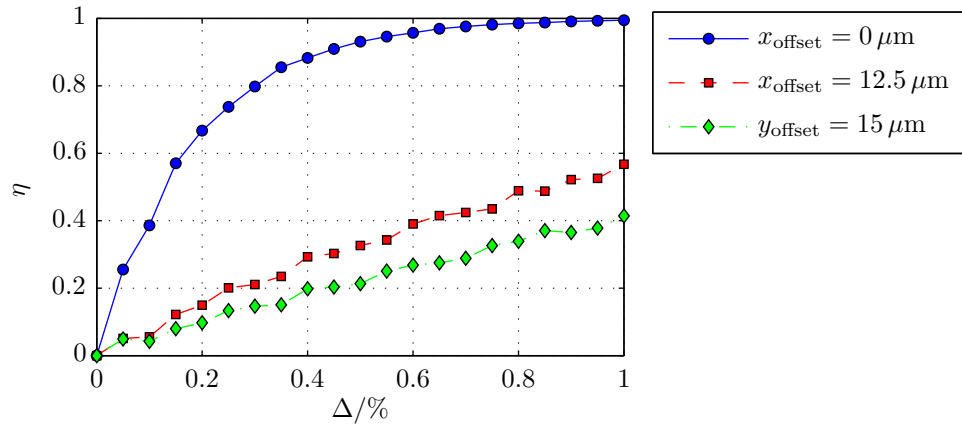


Figure 5.15: Throughput η vs. relative refractive index difference Δ for different lateral laser misalignments x_{offset} and y_{offset} .

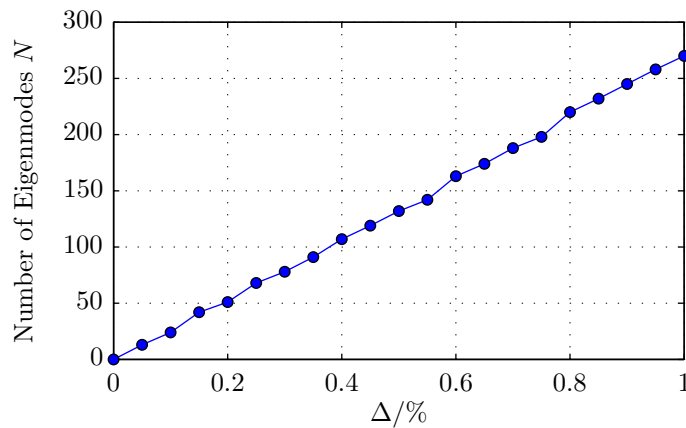


Figure 5.16: Number of multi-core waveguide eigenmodes N vs. relative refractive index difference Δ .

5.5 Throughput of Different VCSEL Modes

In Section 2.3 the VCSEL output field model was presented. Here, we compute the throughput of the Laguerre Gaussian laser modes using the spatial field distribution from Equation (2.6) with the mode radii $w_0(l, p)$ from Table 2.3. In Figure B.1 the normalized intensity distributions of these VCSEL modes are depicted.

Figure 5.17 shows the simulation results for a lateral offset of $x_{\text{offset}} = y_{\text{offset}} = 0 \mu\text{m}$. It can be seen that the LP_{01} mode has the largest throughput of $\eta = 67\%$ while all modes of higher order have a throughput smaller than 30%. The actual output field of a multi-mode VCSEL is generally a *weighted sum* of the eigenmodes with the weights depending on the operating point, i.e. the laser drive current (see [7]).

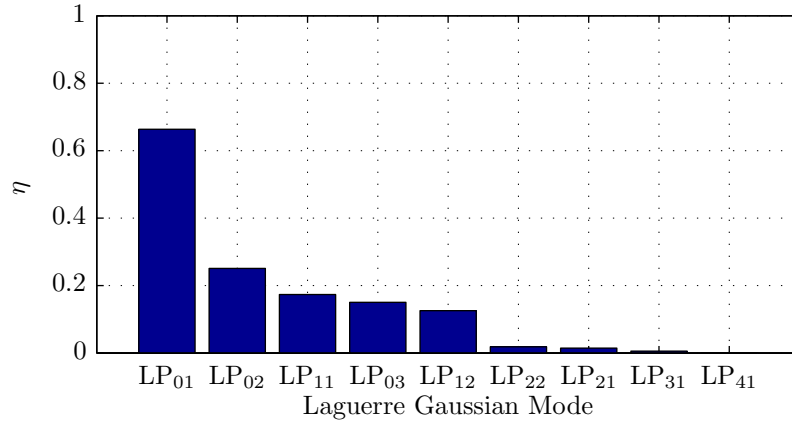


Figure 5.17: Throughput η of different Laguerre Gaussian VCSEL modes.

Chapter 6

Complex Multi-Core Structures

6.1 Introduction and Outline

In this chapter various multi-core structures are investigated, which are *not* invariant with respect to the z direction. Since eigenmodes are only defined for waveguides which are invariant with respect to the propagation direction, these “complex” multi-core structures can only be analyzed using BEAMLABBPM.

In some of the simulations the radiation field $\Phi_{\mathcal{H}\perp}$ in the *spatial transient* from Figure 4.1 is not of interest—we assume that the structure is placed in the *spatial steady state* of the waveguide, i.e. sufficiently far away from the light source. In these simulations the radiation field $\Phi_{\mathcal{H}\perp}$ is “filtered” by using the Eigenmode Decomposition Method. The actual input fields of these simulations are $\Phi_{\text{in}} = \Phi_{\mathcal{H}}$ rather than $\Phi_{\text{in}} = \Phi_0$.

This chapter is organized as follows.

- In Section 6.2 the throughput of bent multi-core waveguides is analyzed for different bend angles.
- In Section 6.3 multi-core waveguide splitters are investigated.
- In Section 6.4 the crosstalk of multi-core waveguides crossing each other is analyzed.
- In Section 6.5 a concept of external modulators using Mach-Zehnder interferometers is discussed.
- In Section 6.6 tapered multi-core waveguides, which could significantly reduce the time required to inscribe a waveguide using TPA, are investigated.
- In Section 6.7 the deformation of multi-core waveguides is investigated. By applying pressure onto the waveguide, the throughput and hence, the photocurrent can be reduced.
- Finally, in Section 6.8 the influence of a pulsed TPA waveguide inscription process on the waveguide throughput is investigated.

6.2 Bent Multi-Core Waveguides

One of the advantages of inscribing waveguides using the TPA process is that it is possible to create virtually any waveguide shape in all three dimensions. On the other hand, lithographically manufactured waveguides are often limited to the x - z -plane from Figure 1.1.

One especially useful shape is a bent waveguide, since it allows to connect a VCSEL and a photodiode which are not located at the same x and y coordinates. It also is the basic

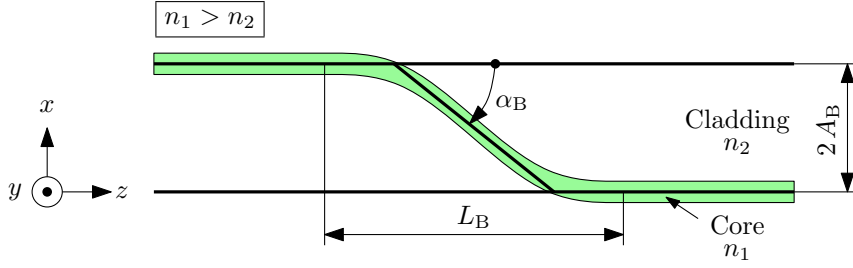


Figure 6.1: Definition of the bend angle α_B .

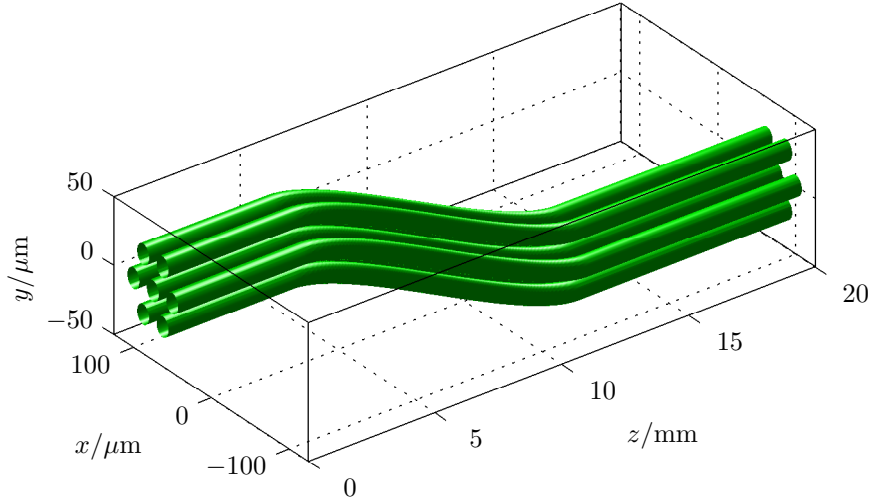


Figure 6.2: Three-dimensional refractive index profile of a bent multi-core waveguide. Here, the bend angle is $\alpha_B = 2^\circ$. The surface shows all points with equal refractive index $n = n_2 + (n_1 - n_2)/e = 1.5161$.

element used in multi-core waveguide splitters (see Section 6.3), crossing multi-core waveguides (see Section 6.4), and multi-core Mach-Zehnder interferometers (see Section 6.5). Using a lithographical manufacturing process, it is very difficult to connect a VCSEL and a photodiode which are located at different y coordinates. On the other hand, such bent waveguides can easily be manufactured using the TPA process.

Waveguide Model. Figure 6.1 shows the definition of the *bend angle* α_B . For the sake of simplicity, here only a single core is depicted. The bend angle is related to the *bend length* L_B and the *bend offset* $2A_B$ ¹ by the simple geometrical relation

$$\alpha_B = \arctan\left(\frac{\pi A_B}{L_B}\right). \quad (6.1)$$

In Figure 6.1 the bend angle is defined as an angle with respect to the z direction in the plane $y = 0$. By an appropriate rotation of the coordinate system any angle with respect to the z direction can be transformed into an angle in the plane $y = 0$. Figure 6.2 shows the three-dimensional refractive index profile of a bent multi-core waveguide with $\alpha_B = 2^\circ$. Here, the bend offset is $2A_B = 150 \mu\text{m}$.

¹ A_B is actually the amplitude of the cosine function connecting the two parts of the waveguide which are invariant with respect to the z direction. This explains why there is a factor of 2 in the definition of the bend offset.

Simulation Results. Figure 6.3 shows the spatial intensity distributions of propagating beams for different values of the bend angle α_B . The input field Φ_0 is decomposed using the Eigenmode Decomposition Method and only $\Phi_{\mathcal{H}}$, the component in the Hilbert space of eigenmodes, is used as actual simulation input field Φ_{in} , i.e. $\Phi_{\text{in}} = \Phi_{\mathcal{H}}$. The reason for using $\Phi_{\mathcal{H}}$ as input field, rather than simply using Φ_0 , is that in these simulations we are not interested in the losses from the laser \rightarrow waveguide coupling, but only in the effects of the waveguide bend. Therefore in the region $0 \text{ mm} \leq z \leq 5 \text{ mm}$ in Figure 6.3 there are *no* losses since, per definition, the throughput of $\Phi_{\mathcal{H}}$ is $\eta(\Phi_{\mathcal{H}}) = 1$. If the input field was $\Phi_{\text{in}} = \Phi_0$, there would be some losses like, for example, in Figure 5.2(a).

Figure 6.4 shows the throughput as a function of the bend angle. The throughput decreases rather fast with increasing bend angle—for $\alpha_B \geq 4.5^\circ$ the throughput is effectively zero.

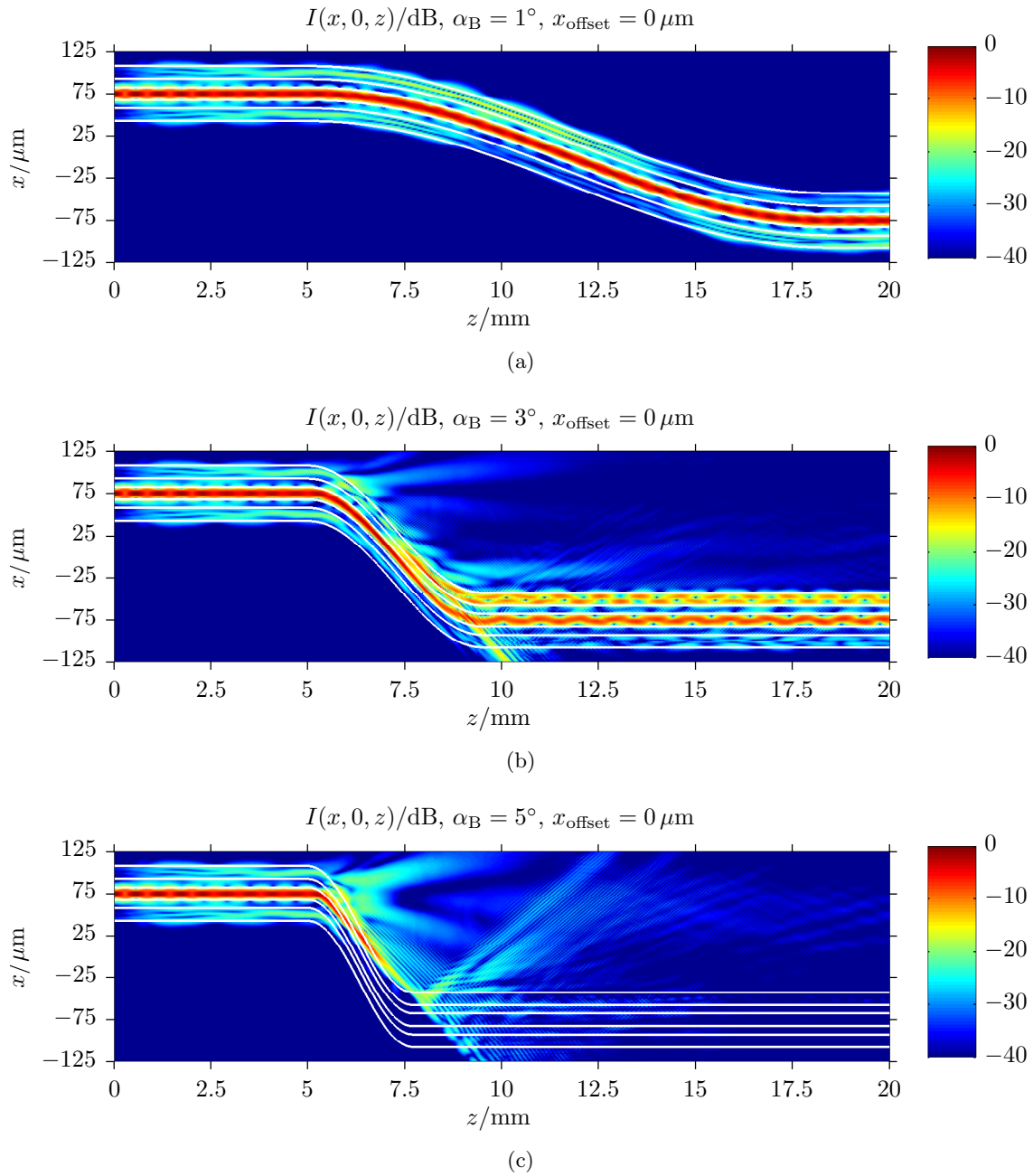


Figure 6.3: Intensity I in the plane $y = 0$ of beams propagating in bent multi-core waveguides for different values of the bend angle α_B .

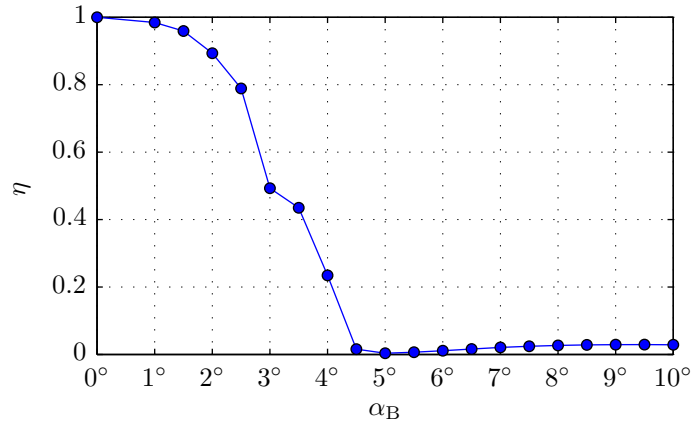


Figure 6.4: Throughput η of a bent multi-core waveguide vs. bend angle α_B . Here, the lateral laser misalignment is $x_{\text{offset}} = y_{\text{offset}} = 0 \mu\text{m}$.

6.3 Multi-Core Waveguide Splitters

In this section we investigate multi-core waveguide splitters. Splitters are very useful to distribute an optical signal from a single VCSEL to multiple photodiodes. An ideal *1:2-splitter*², with one input port and two output ports, would split the input power into equal parts at the two output ports, i.e. the throughputs of the two splitter arms should be $\eta_1 = \eta_2 = 0.5$. It is evident that an ideal splitter furthermore has a total throughput of $\eta_1 + \eta_2 = 1$, i.e. no power is lost in the splitter.

Waveguide Model. Figure 6.5 shows the three-dimensional refractive index profile of the multi-core waveguide splitter model. The bend angles, as defined in Figure 6.1, of the two splitter arms are $\alpha_B = 1.35^\circ$. According to Figure 6.4 this bend angle leads to a very small loss of $1 - \eta < 4\%$ due to the bending.

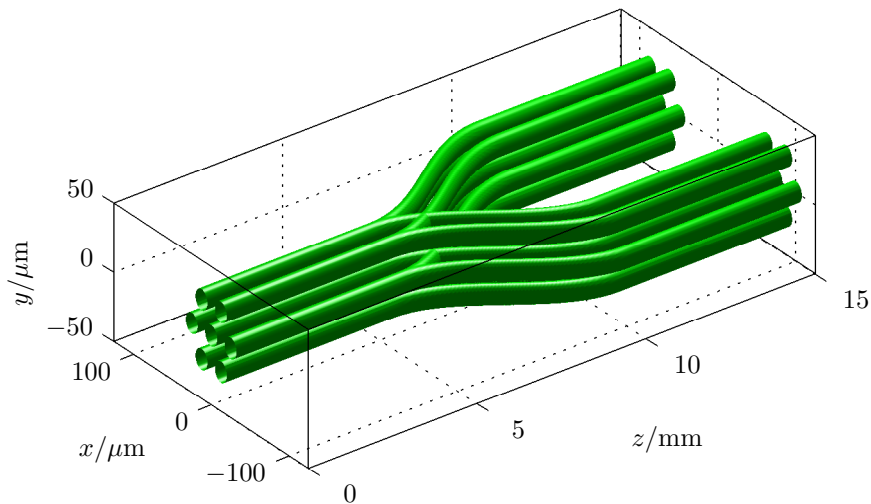


Figure 6.5: Three-dimensional refractive index profile of a multi-core waveguide splitter. The surface shows all points with equal refractive index $n = n_2 + (n_1 - n_2)/e = 1.5161$.

²In this context this type of splitter is also called *Y-splitter*, or *3 dB-splitter*

Simulation Results. Figure 6.6 shows the intensity of the propagating beams in the waveguide splitter for different values of x_{offset} . Here, like in Section 6.2, the simulation input field is $\Phi_{in} = \Phi_{\mathcal{H}}$, rather than $\Phi_{in} = \Phi_0$ in order to “filter” the spatial transient.

In Figure 6.7 the throughput η_1 and η_2 of the two splitter arms, as well as the total throughput $\eta_1 + \eta_2$ is depicted. Due to interference effects the output power of the two arms can be quite different. According to Figure 6.7, a throughput of $\eta_1 > 20\%$ in the upper splitter arm and $\eta_2 > 20\%$ in the lower splitter arm can be guaranteed, independent of the lateral misalignment of the laser at the waveguide input.

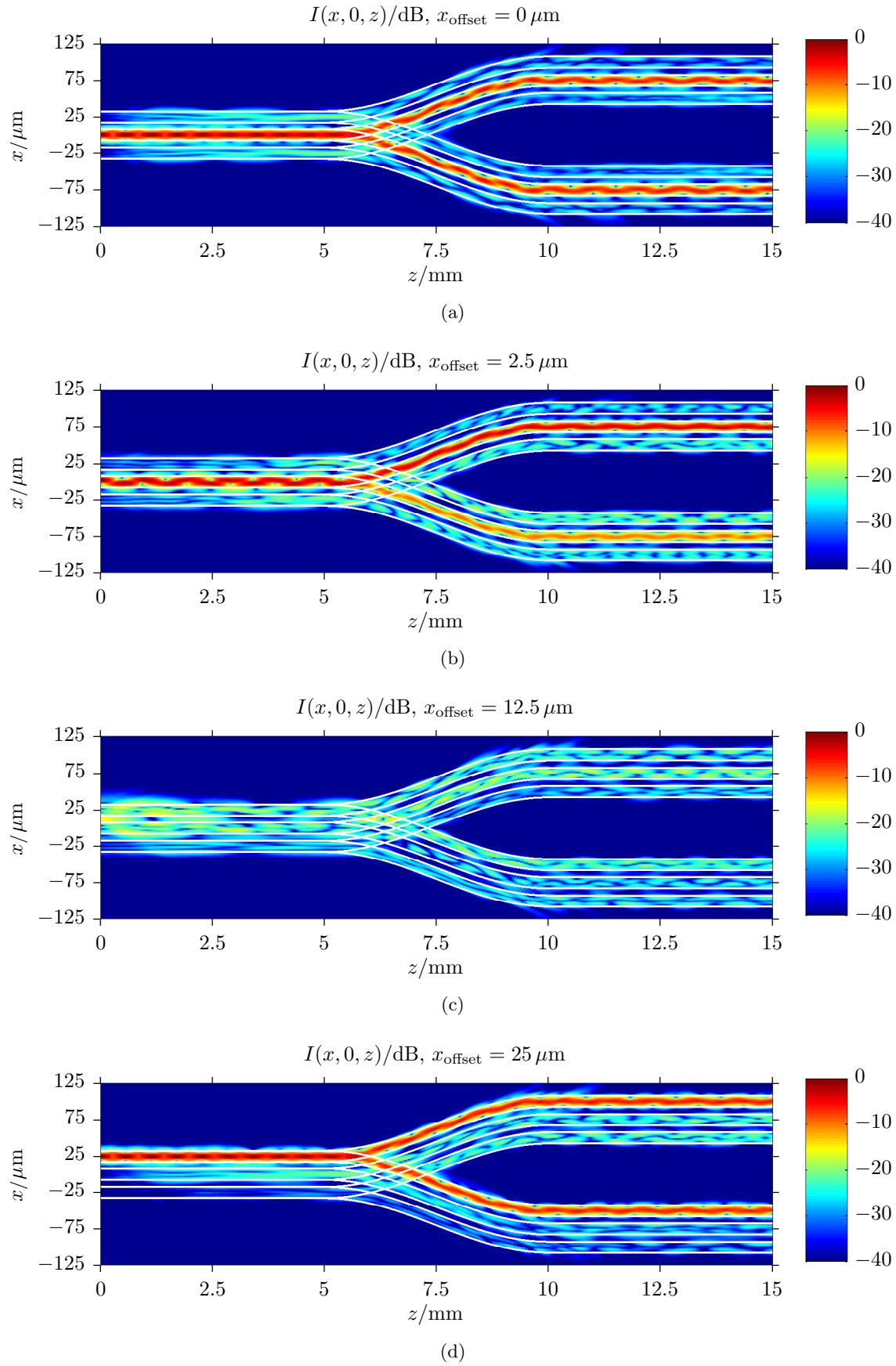


Figure 6.6: Intensity I in the plane $y = 0$ of beams propagating in a multi-core waveguide splitter for different values of the lateral laser misalignment x_{offset} .

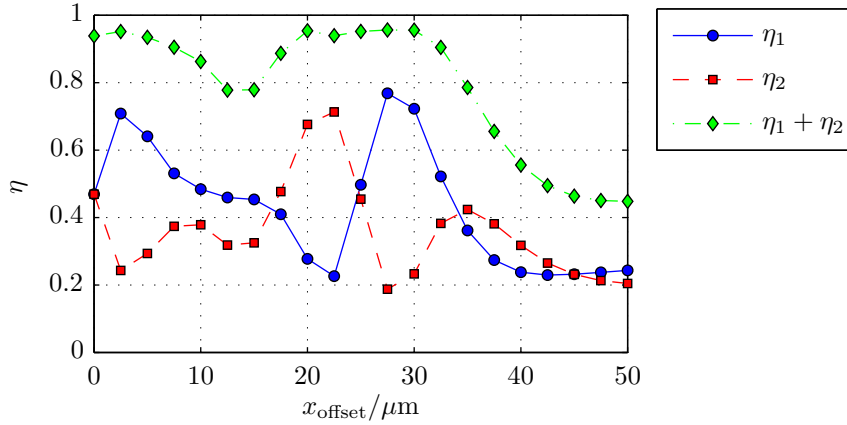


Figure 6.7: Throughputs η_1 and η_2 from the input at $z = 0$ to the upper and lower splitter arm, respectively, as a function of the lateral laser misalignment x_{offset} . $\eta_1 + \eta_2$ is the total throughput.

6.4 Crossing Multi-Core Waveguides

In this section the crosstalk of multi-core waveguides crossing each other is investigated.

Waveguide Model. Figure 6.8 shows the three-dimensional waveguide model of two crossing waveguides. The crosstalk χ is defined as the residual throughput between the two waveguides.

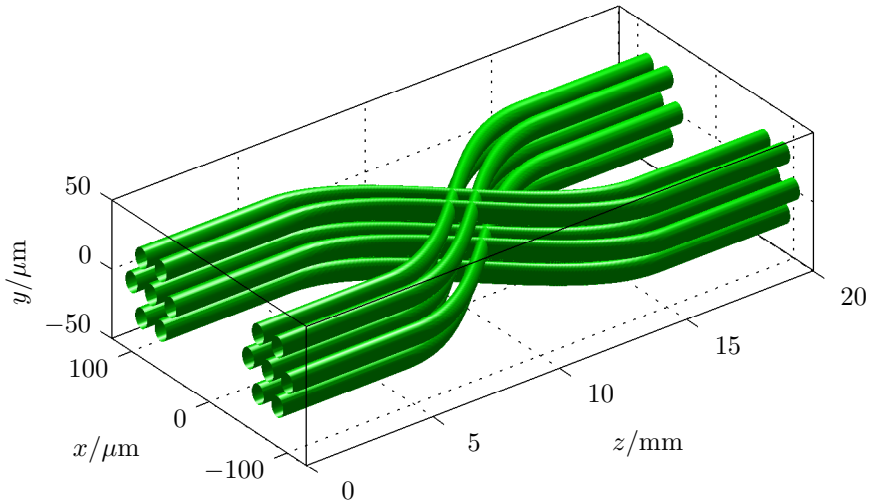


Figure 6.8: Three-dimensional refractive index profile of a two multi-core waveguides crossing each other. The surface shows all points with equal refractive index $n = n_2 + (n_1 - n_2)/e = 1.5161$.

Simulation Results. Figure 6.9 shows the spatial intensity distributions of beams propagating in two multi-core waveguides crossing each other. Here, $x_{\text{offset}} = 0 \mu\text{m}$ means that the input beam is perfectly aligned with respect to the upper waveguide, which has its center at $x = 75 \mu\text{m}$. In these simulations, like in Section 6.2, the simulation input field is $\Phi_{\text{in}} = \Phi_{\mathcal{H}}$, rather than $\Phi_{\text{in}} = \Phi_0$ in order to “filter” the spatial transient.

Figure 6.10 depicts the crosstalk $\chi = \eta_1$ between two multi-core waveguides crossing

each other. The throughput is smaller than

$$\boxed{\chi < 6\%}. \quad (6.2)$$

In practical applications this small crosstalk might be negligible. On the other hand, the losses $1 - \eta_2$ in the waveguide connecting the input in the top left to the output in the bottom right corner of Figure 6.9 might *not* be negligible— η_2 is as low as 34% for a lateral laser misalignment of $x_{\text{offset}} = -12.5 \mu\text{m}$. As mentioned above, the input fields for these simulations are already $\Phi_{\text{in}} = \Phi_{\mathcal{H}}$. That means, that the losses of $1 - \eta_2 = 66\%$ (for $x_{\text{offset}} = -12.5 \mu\text{m}$) are *additional* to the losses from the input coupling laser \rightarrow waveguide.

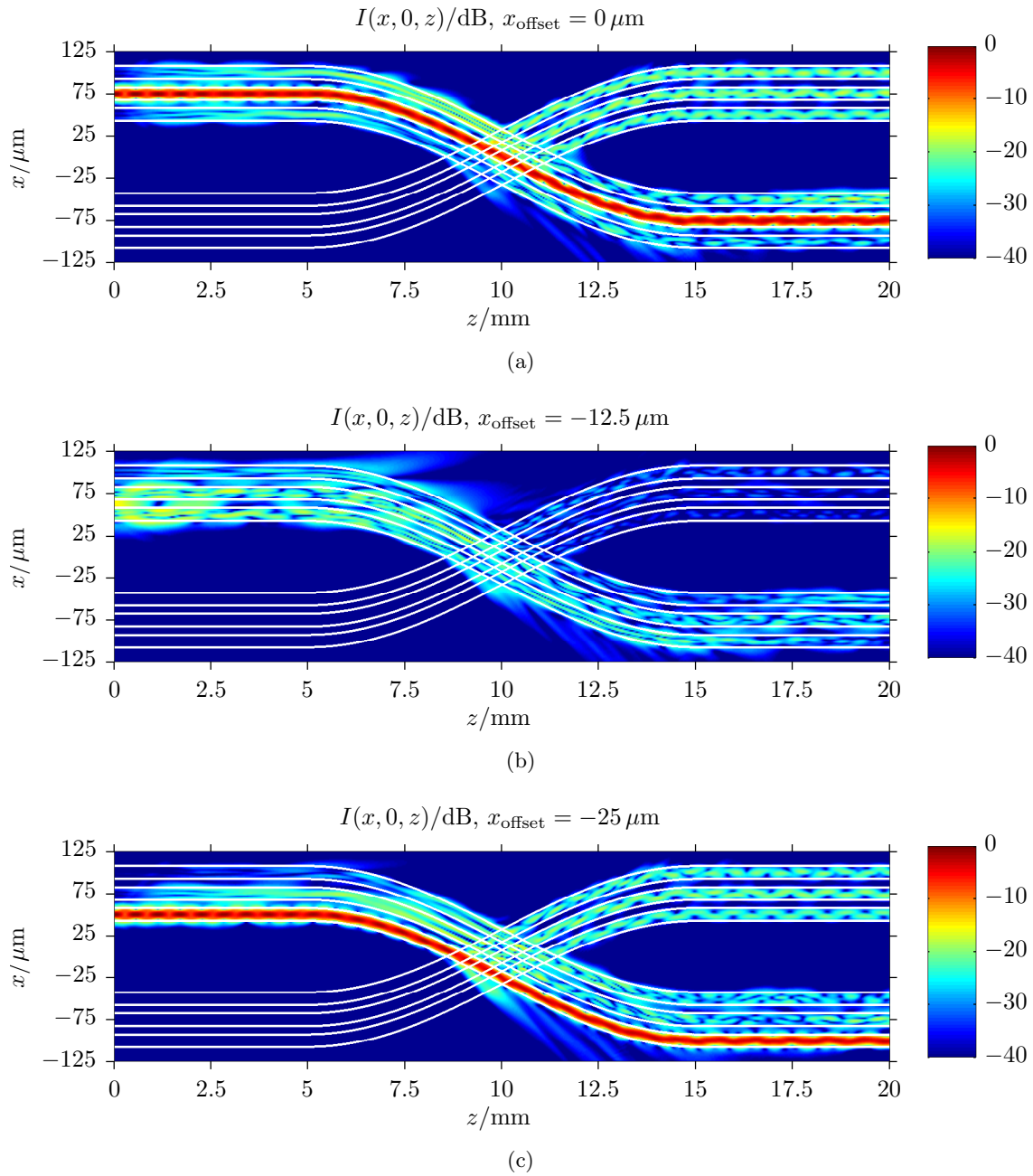


Figure 6.9: Intensity I in the plane $y = 0$ of beams propagating in crossing multi-core waveguides for different values of the lateral laser misalignment x_{offset} .

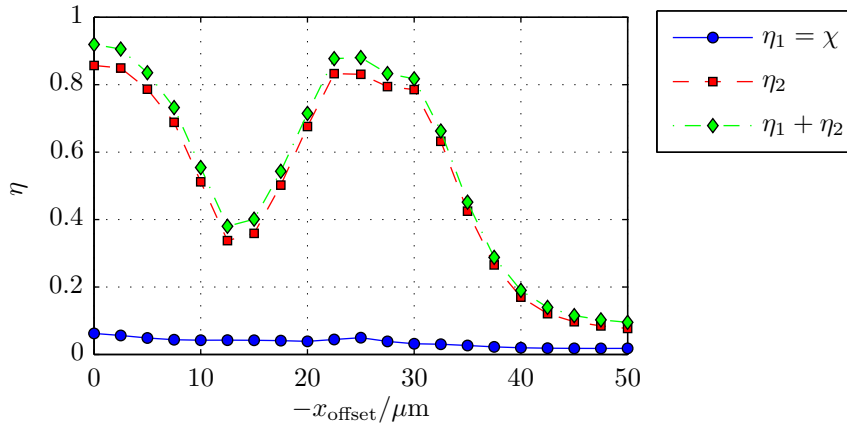


Figure 6.10: Crosstalk $\chi = \eta_1$ between two multi-core waveguides crossing each other as a function of the lateral laser misalignment x_{offset} . η_2 is the throughput from the top left input to the bottom right output in Figure 6.9.

6.5 Multi-Core Mach-Zehnder Interferometers

Integrated Mach-Zehnder interferometers could potentially be used to build fast external modulators for lasers operated in a continuous-wave (CW) mode. If the refractive index is changed in one of the interferometer arms, for example by an electro-optical effect, the output of the interferometer can be switched between “on” (ideally, $\eta = 1$) and “off” (ideally, $\eta = 0$). This is due to either constructive or destructive interference of the fields at the outputs of the two arms, depending on the phase shift induced by the different refractive indices in the two interferometer arms. If no phase shift exists between the fields in the two interferometer arms, there should be constructive interference at the output.

Waveguide Model. Figure 6.11 shows the three-dimensional refractive index profile of the multi-core Mach-Zehnder interferometer. The input at $z = 0$ mm is split into the two interferometer arms at $z = 5$ mm which are combined at $z = 20$ mm to one output port.

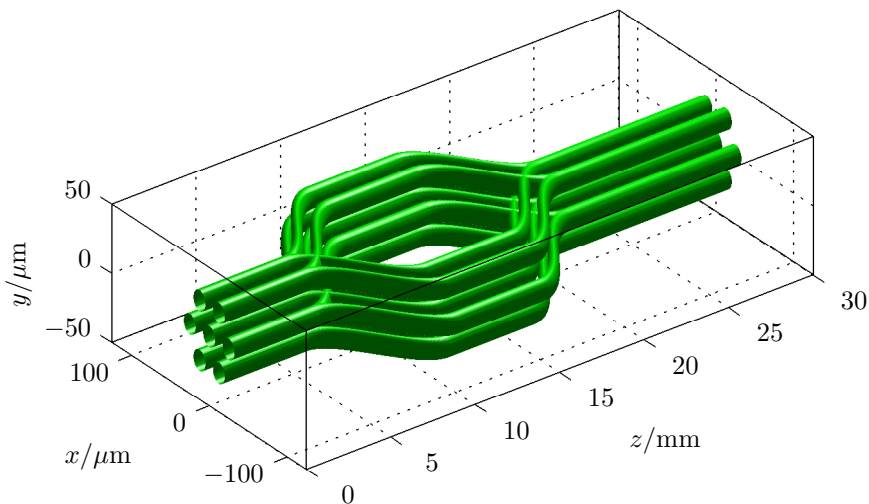


Figure 6.11: Three-dimensional refractive index profile of a multi-core Mach-Zehnder interferometer. The surface shows all points with equal refractive index $n = n_2 + (n_1 - n_2)/e = 1.5161$.

Simulation Results. Figure 6.12 shows the spatial intensity distribution of beams propagating in the Mach-Zehnder interferometer structure without any phase shift between the two arms. In all three subfigures (a)–(c) there is radiated some power when combining the two arms at $z = 20$ mm. Again, like in Section 6.2, the simulation input field is $\Phi_{\text{in}} = \Phi_{\mathcal{H}}$, rather than $\Phi_{\text{in}} = \Phi_0$.

Figure 6.13 depicts the throughput vs. lateral laser misalignment x_{offset} of the multi-core Mach-Zehnder interferometer. Ideally, for no phase shift between the interferometer arms, the throughput should be $\eta = 1$, independent of x_{offset} . This shows that *it is difficult to build a reliable multi-core Mach-Zehnder interferometer* since the throughput heavily depends on the input misalignment. The throughput is as low as $\eta = 43\%$ for $x_{\text{offset}} = 12.5 \mu\text{m}$. The reason for this partially destructive interference, even in the absence of a phase shift between the two interferometer arms, is the large number of $N = 51$ eigenmodes of the multi-core structure.

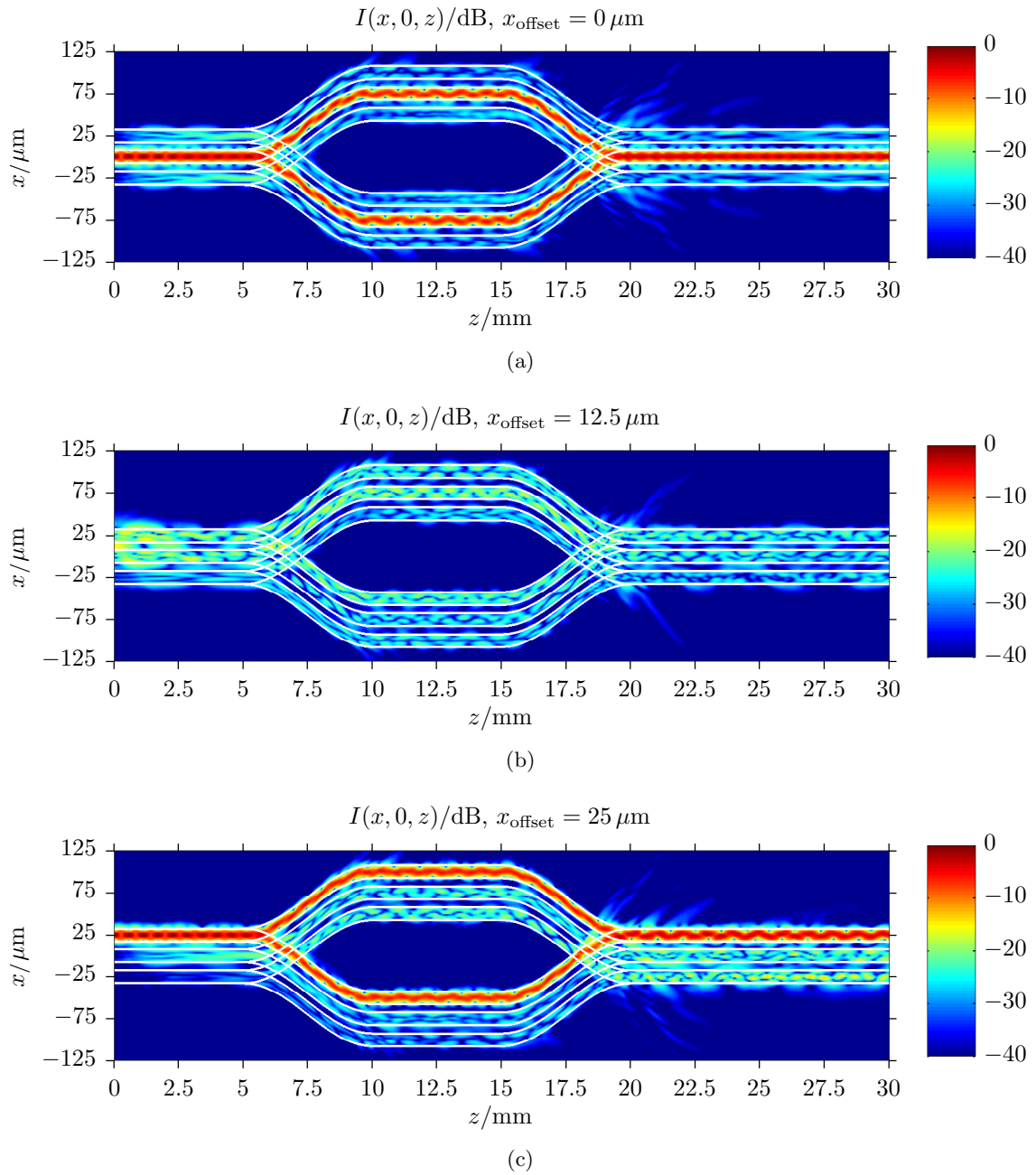


Figure 6.12: Intensity I in the plane $y = 0$ of beams propagating in a multi-core Mach-Zehnder interferometer for different values of the lateral laser misalignment x_{offset} .

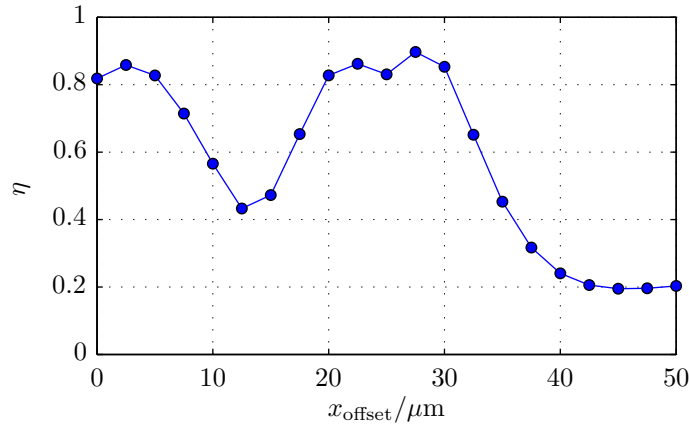


Figure 6.13: Throughput η of a multi-core Mach-Zehnder interferometer vs. lateral laser misalignment x_{offset} .

6.6 Multi-Core Taper Waveguides

In this section single-core waveguides with multi-core waveguide tapers are investigated. Ideally, these structures should have the same low sensitivity to laser misalignment as multi-core waveguides. However, for seven waveguide cores, the time required to inscribe a waveguide into the substrate material is approximately reduced by a factor of 7, since only in the region $0 \leq z \leq L_T$, with L_T as the so-called *taper length*, there have to be inscribed seven cores. More generally, for N waveguide cores, the required manufacturing time is approximately reduced by a factor of N .

Waveguide Model. Figure 6.14 shows the three-dimensional simulation model of the single-core waveguide with a multi-core taper. There are seven cores at the input at $z = 0$ mm, which are merged to a single core in the interval $0 \leq z \leq L_T$.

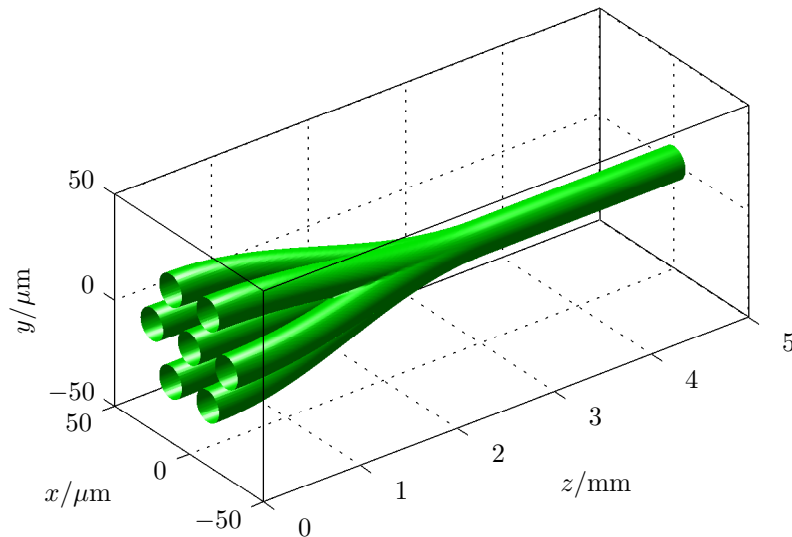


Figure 6.14: Three-dimensional refractive index profile of a single-core waveguide with a multi-core taper. Here, the taper length is $L_T = 3$ mm. The surface shows all points with equal refractive index $n = n_2 + (n_1 - n_2)/e = 1.5161$.

Simulation Results. Figure 6.15 shows spatial intensity distributions of beams propagating in the multi-core taper structure. Figure 6.15(b) shows that for a lateral laser misalignment of $x_{\text{offset}} = 12.5 \mu\text{m}$, effectively all of the input power is radiated, i.e. $\eta = 0$. Comparing this simulation result with the one from Figure 5.2(b), where the standard multi-core waveguide from Section 2.2.1 is used, it can be seen that the throughput of the multi-core taper waveguide is much lower than the one of the standard multi-core waveguide. Comparing Figure 6.15(c), where $L_T = 3 \text{ mm}$, and (d), where $L_T = 1 \text{ mm}$, it can be seen that the throughput also depends on the taper length.

Figure 6.16 depicts the throughput vs. lateral laser misalignment x_{offset} for different values of the taper length L_T . The throughput values of the tapered multi-core waveguides with $L_T = 2 \text{ mm}$, $L_T = 3 \text{ mm}$, and $L_T = 5 \text{ mm}$ are approximately equal, while the throughput of $L_T = 1 \text{ mm}$ at $x_{\text{offset}} = 25 \mu\text{m}$ is almost zero.

Figure 6.17 shows a comparison of the throughput between a multi-core taper waveguide, a standard multi-core waveguide with no taper (see Section 2.2.1), and a single-core waveguide with no taper (see Section 2.2.2). As already discussed in the stochastic lateral misalignment model in Section 5.2, small values of the lateral misalignment x_{offset} occur with a higher probability than large values. Hence, Figure 6.17 shows that *the throughput of a multi-core taper waveguide is actually inferior to the throughput of a single-core waveguide.*

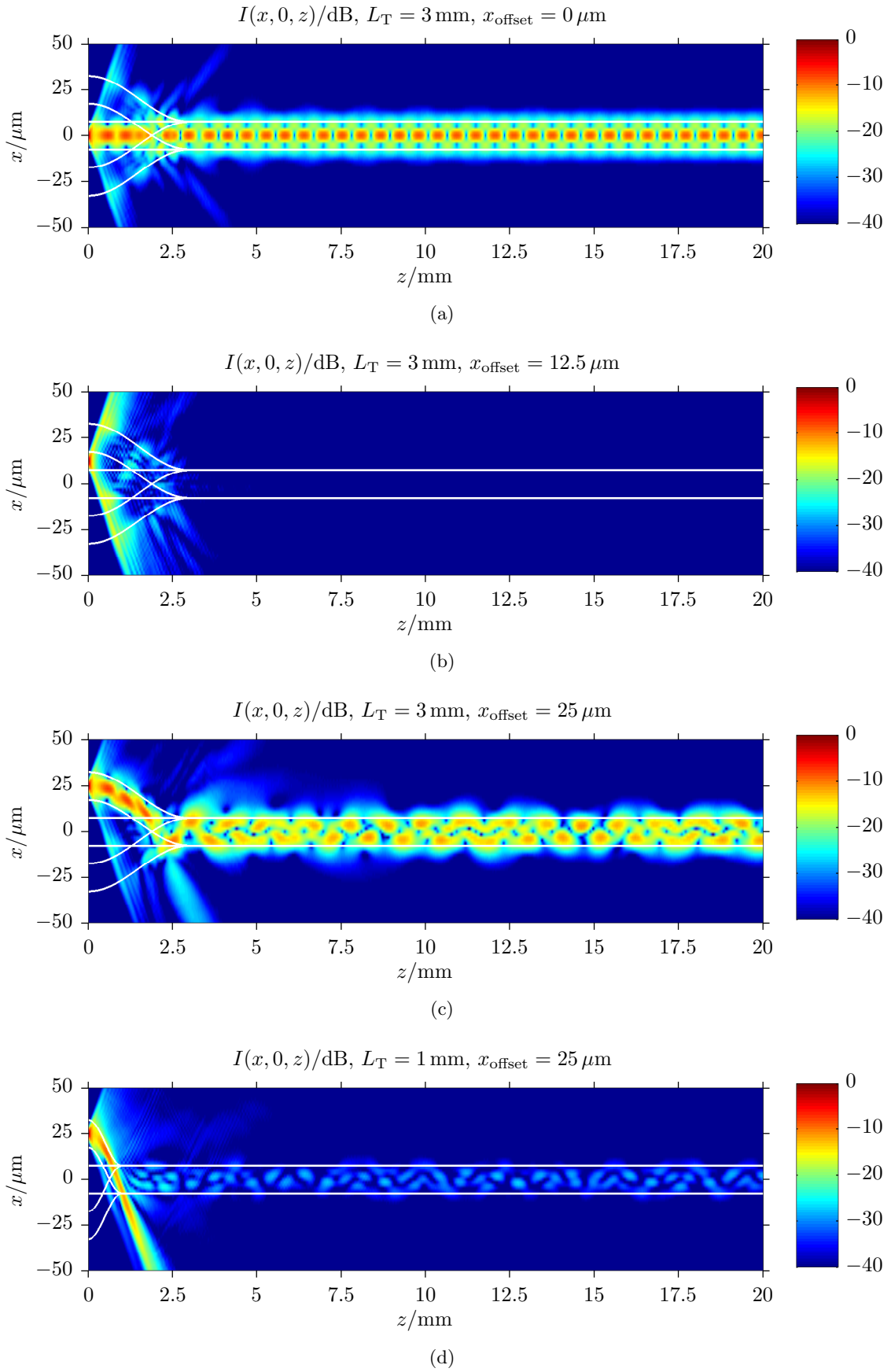


Figure 6.15: Intensity I in the plane $y = 0$ of beams propagating in a multi-core taper waveguide for different values of the taper length L_T and the lateral laser misalignment x_{offset} .

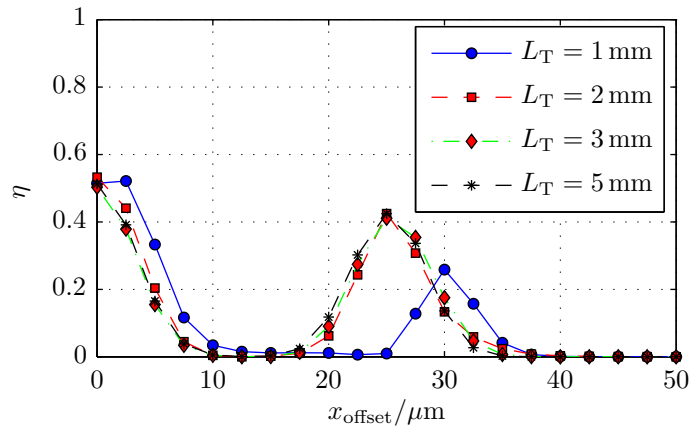


Figure 6.16: Throughput η of a multi-core taper waveguide vs. lateral laser misalignment x_{offset} for different values of the taper length L_T .

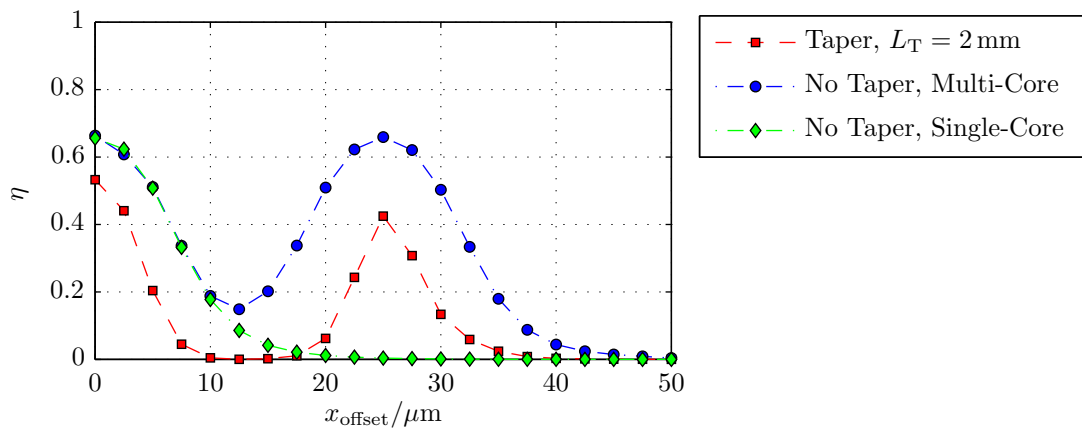


Figure 6.17: Comparison of the throughputs η of a multi-core taper waveguide, a single-core waveguide with no taper, and a multi-core waveguide with no taper.

6.7 Deformation of Multi-Core Waveguides

In this section the deformation of multi-core waveguides, caused by pressure applied onto the waveguide, is investigated. By applying a sufficiently large pressure onto the waveguide, the optical output power—and therefore the photocurrent of the photodiode—can be influenced. This effect is not limited to multi-core waveguides—in fact *any* elastic waveguide has this property to some degree.

Waveguide Model. Figure 6.19 shows a three-dimensional model of the multi-core waveguide, which is deformed by applying pressure onto the center section $10 \text{ mm} \leq z \leq 20 \text{ mm}$. The deformation is modelled as a change of the core radius $w_{0,n,y}$ in y direction with respect to the z direction as

$$w_{0,n,y}(z) = \frac{1}{2}(w_{0,n,\max} - w_{0,n,\min}) \left[1 + \cos \left(2\pi \frac{z - z_1}{z_2 - z_1} \right) \right] + w_{0,n,\min}, \quad (6.3)$$

where $w_{0,n,\max}$ and $w_{0,n,\min}$ are maximum and minimum of the core radius, respectively, and z_1 and z_2 are the locations of start and end of the deformation. In Figure 6.19, $z_1 = 10 \text{ mm}$ and $z_2 = 20 \text{ mm}$. The *compression factor* is defined as

$$\zeta = \frac{w_{0,n,\max}}{w_{0,n,\min}}. \quad (6.4)$$

The core radius $w_{0,n,x}$ in x direction is modelled to be constant with respect to the z direction, i.e. $w_{0,n,x}(z) = w_{0,n,x}$. The centers of the cores are located at

$$\tilde{y}_k = y_k - \frac{1}{2}(w_{0,n,\max} - w_{0,n,\min}) \left[1 - \cos \left(2\pi \frac{z - z_1}{z_2 - z_1} \right) \right] \quad \text{for } k = 1, \dots, 7, \quad (6.5)$$

while the x locations stay constant, i.e. $\tilde{x}_k = x_k$ for $k = 1, \dots, 7$.

Simulation Results. Figures 6.20(a) and (b) show the spatial intensity distribution in the planes $y = 0$ and $x = 0$, respectively, of a beam propagating in a deformed waveguide with compression factor $\zeta = 4$.

Figure 6.21 shows the power $\mathcal{O}(\Phi_z, V_n)$ in each of the waveguide eigenmodes as a function of z . Each color represents one eigenmode. In Figure 6.21(a) the compression factor is $\zeta = 1$, i.e. the waveguide is not deformed at all. The power carried by each waveguide eigenmode is constant with respect to z . In Figure 6.21(b) the waveguide is deformed by a compression factor of $\zeta = 4$. Here, in the middle section $z_1 \leq z \leq z_2$ *mode conversions* can be seen,

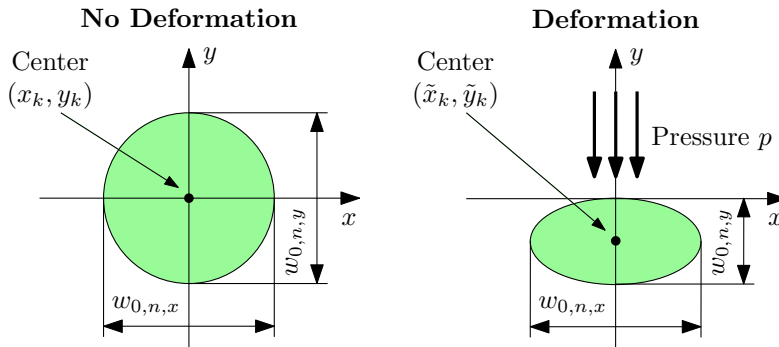


Figure 6.18: Schematic representation of the waveguide deformation model. The pressure p is applied onto the waveguide which causes a reduction of $w_{0,n,y}$ and changes the center of the waveguide to $(\tilde{x}_k, \tilde{y}_k)$.

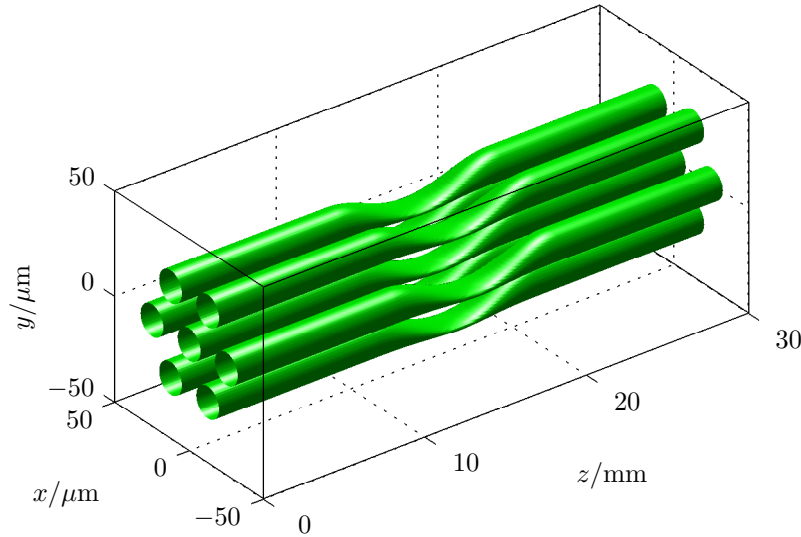


Figure 6.19: Three-dimensional refractive index profile of a multi-core waveguide deformed by applying pressure onto it (compression factor $\zeta = 4$). The surface shows all points with equal refractive index $n = n_2 + (n_1 - n_2)/e = 1.5161$.

resulting in a reduced overall throughput $\tilde{\eta}(\Phi_0)$. This leads to a relative change in output power compared to the undeformed waveguide, which directly relates to a relative change in photocurrent

$$\Delta I_{\text{PD,rel}} = \frac{\tilde{\eta}(\Phi_0)}{\eta(\Phi_0)} - 1. \quad (6.6)$$

Figure 6.21(c) shows the power carried by each waveguide eigenmode for a lateral laser misalignment of $x_{\text{offset}} = 12.5 \mu\text{m}$ and a compression factor of $\zeta = 4$. Here, the *relative* change in photocurrent is larger than for $x_{\text{offset}} = 0 \mu\text{m}$, while the *absolute* change in photocurrent is smaller. In Figures 6.21(a) and (b) most of the power is carried by the fundamental $V_1(x, y)$ mode (see Figure A.3), which has a negligible attenuation in spite of the deformation. In Figure 6.21(c) this fundamental mode is not excited by the input field at $z = 0$, which results in the larger *relative* photocurrent change mentioned above. In order to get a large relative photocurrent change, we must excite waveguide eigenmodes which show a large attenuation due to the deformation of the waveguide.

Figures 6.22 shows the relative photocurrent change as a function of the waveguide compression factor. $|\Delta I_{\text{PD,rel}}|$ increases with increasing compression factor. $|\Delta I_{\text{PD,rel}}|$ can also be increased by exciting only waveguide eigenmodes which show a large attenuation caused by the deformation, which, for example, is the case for $x_{\text{offset}} = 12.5 \mu\text{m}$ (see Figure 6.21). *To guarantee a large relative photocurrent change for any lateral laser misalignment, the compression factor has to be rather large.* In the worst case, i.e. $x_{\text{offset}} = 0 \mu\text{m}$ ³, a waveguide compression factor of $\zeta = 2$ results in a relative photocurrent change of $\Delta I_{\text{PD,rel}} = -7.6\%$.

³Since here, we do not want to excite the waveguide eigenmode $V_1(x, y)$, the absence of a lateral laser misalignment, i.e. $x_{\text{offset}} = 0 \mu\text{m}$, is *not* desirable—in fact, here it is the worst case.

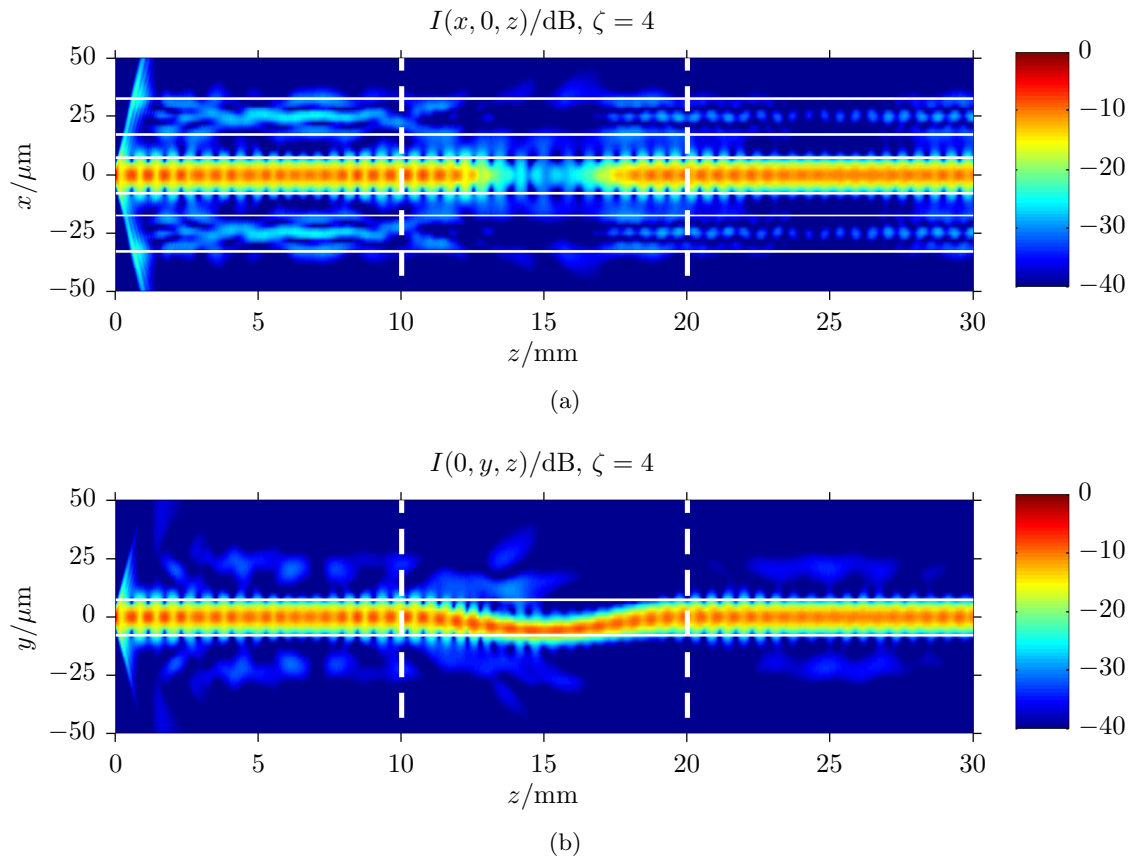
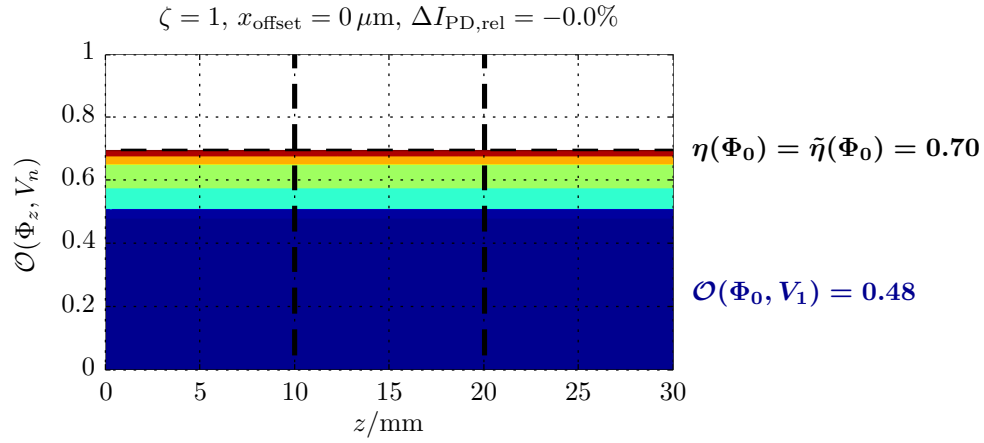
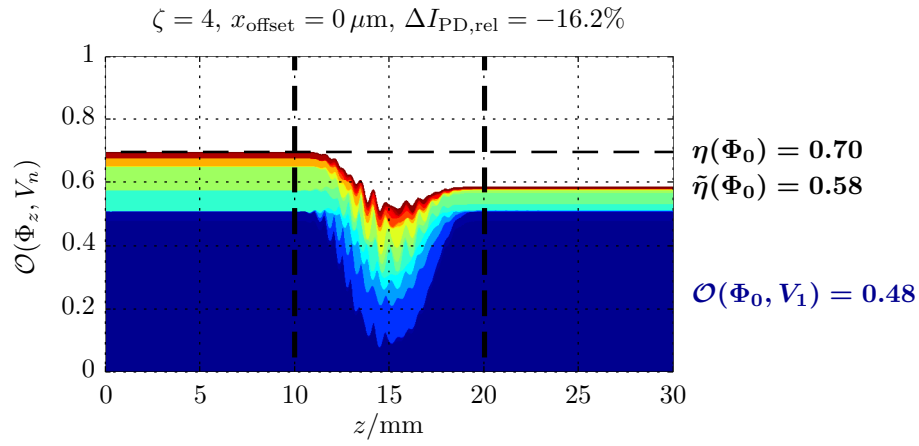


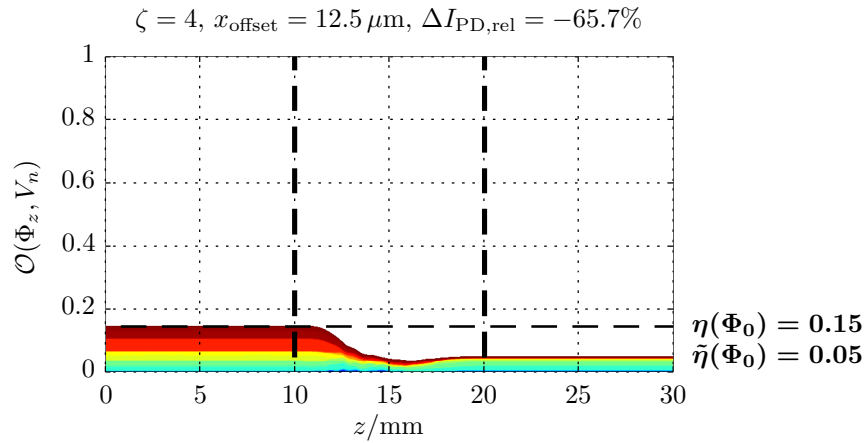
Figure 6.20: Intensity I in (a) the plane $y = 0$ and (b) the plane $x = 0$ of beams propagating in the deformed multi-core waveguide from Figure 6.19. The solid white lines indicate the locations of the cores of the *undeformed* waveguide.



(a)



(b)



(c)

Figure 6.21: Throughput $\sum_{n=1}^N \mathcal{O}(\Phi_z, V_n)$ for different values of the waveguide compression factor ζ and lateral offset x_{offset} . Each color represents the power $\mathcal{O}(\Phi_z, V_n)$ carried in one of the waveguide eigenmodes V_n at propagation distance z .

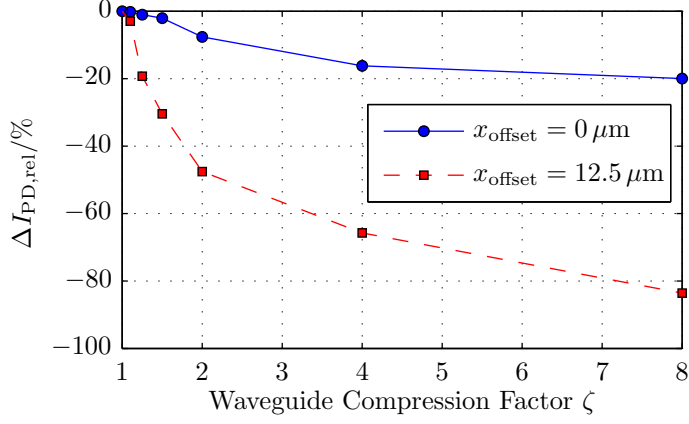


Figure 6.22: Simulated relative photocurrent change $\Delta I_{PD,rel}$ vs. waveguide compression factor ζ .

6.8 Periodic Refractive Index Variation in Propagation Direction

As already explained in the introduction in Section 1.1, the TPA process needs very high laser intensities which, at least today, can only be created using pulsed lasers. The inscription of the waveguides using pulsed lasers results in a refractive index profile, which is *not* invariant with respect to the z direction, but rather shows a periodic structure.

Waveguide Model. Figure 6.23 shows the simulation model of this periodic refractive index variation. Here, Equation (2.1) is replaced by

$$n(x, y, z) = n_2 + n_d \cdot f(x, y, z), \quad (6.7)$$

where

$$f(x, y, z) = \sum_{l=0}^{\lceil L/\Lambda \rceil} \sum_{k=1}^K \exp \left[- \left(\frac{x - x_k}{w_{0,n}} \right)^2 - \left(\frac{y - y_k}{w_{0,n}} \right)^2 - \left(\frac{z - l\Lambda}{w_{0,n}} \right)^2 \right], \quad (6.8)$$

and n_d and $w_{0,n}$ are defined as in Equations (2.2) and (2.4), respectively. Λ is the refractive index period with respect to the z direction and L is the simulation length as defined in Figure 3.1. $\lceil x \rceil$ denotes the smallest integer $\geq x$. The average refractive index \bar{n}_1 with respect to the z direction is defined as

$$\bar{n}_1 = \frac{1}{\Lambda} \int_z^{z+\Lambda} n(0, 0, z) dz. \quad (6.9)$$

Simulation Results. Figure 6.24 shows the throughput of a multi-core waveguide inscribed using a pulsed laser as a function of the refractive index period Λ . The throughput is equal to the throughput of a waveguide which is *invariant* with respect to the z direction, but has a core refractive index of \bar{n}_1 instead of n_1 , i.e.

$$n(x, y) = n_2 + \bar{n}_d \cdot f(x, y), \quad (6.10)$$

where

$$\bar{n}_d = \bar{n}_1 - n_2. \quad (6.11)$$

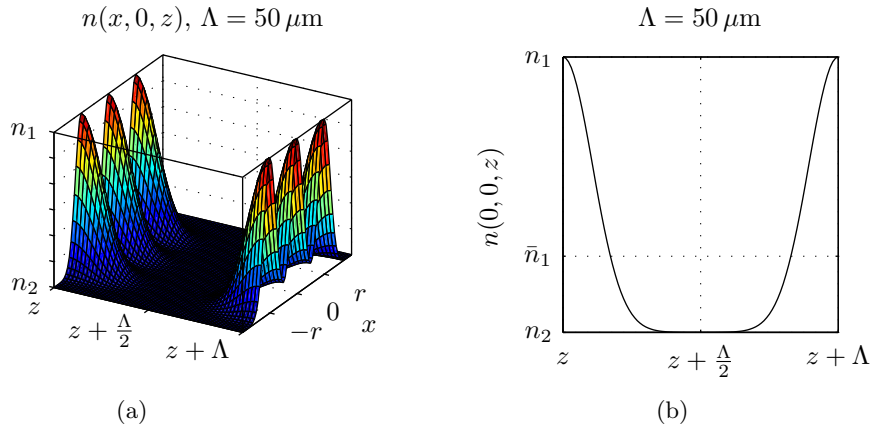


Figure 6.23: Periodic refractive index profile $n(x, y, z)$ (a) in the plane $y = 0$ and (b) in the plane $x = y = 0$. \bar{n}_1 is the average refractive index with respect to the z direction.

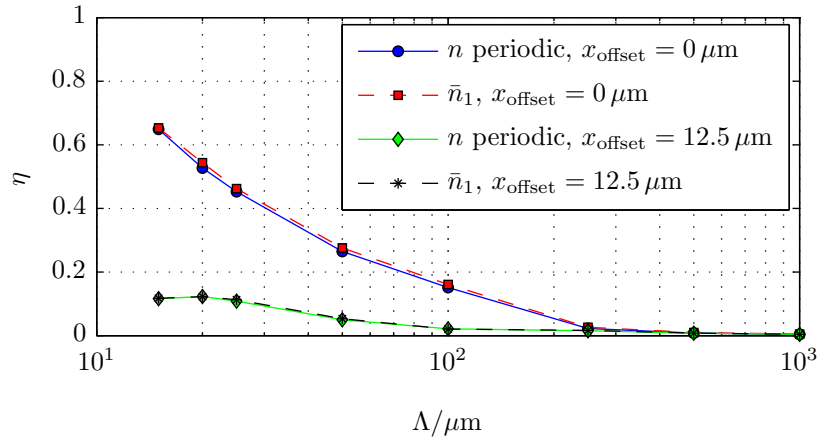


Figure 6.24: Throughput of a multi-core waveguide with periodic refractive index variation according to the model from Equations (6.7)–(6.8) (“ n periodic”). “ \bar{n}_1 ” designates that the waveguide is invariant with respect to the z direction according to the model from Equations (6.10)–(6.11).

In this simulation the approximation from Equation (3.34) might be violated, i.e. the refractive index changes too fast with respect to the z direction. Therefore it is unclear if these simulation results are trustworthy.

Chapter 7

Conclusions and Outlook

In this diploma thesis light propagation in optical multi-core waveguides, which are used in opto-electronic printed circuit boards, has been analyzed numerically. It has been shown that a precise alignment of laser and waveguide is crucial in order to obtain a large throughput and hence, a large photocurrent. Measurements have shown that a large photocurrent more or less directly relates to a large maximum data rate for a given bit error probability. The most important conclusions of the throughput simulations are listed in the following.

- The *average* throughput of a multi-core waveguide is between 20% and 30% if the lateral laser misalignment is modelled stochastically as a jointly Gaussian 2-D real random variable with standard deviations $10 \mu\text{m} \leq \sigma \leq 20 \mu\text{m}$.
- This average throughput is only 10% to 15% larger than the average throughput of a *single-core* waveguide for the same stochastic misalignment model.
- Angular laser misalignment also can reduce the throughput significantly—angles of the emitted laser beam should not be larger than $\theta > 5^\circ$.
- The relative refractive index difference between core and cladding can significantly influence the throughput. This is a possible explanation of the temperature dependence of photocurrents measured at the institute.
- Different laser modes have different throughput values.

Some “complex” multi-core structures, which are not invariant with respect to the propagation direction, have also been investigated. The following list shows the key facts of the simulation results.

- The throughput of bent waveguides is effectively zero if the bend angle is larger than $\alpha_B \geq 4.5^\circ$.
- Multi-core waveguide splitters work reasonably well—regardless of the lateral misalignment at the input of the waveguide, the throughput of each splitter arm is $\geq 20\%$.
- The crosstalk between multi-core waveguides crossing each other is negligible.
- Due to the large number of eigenmodes of multi-core waveguides, integrated Mach-Zehnder interferometers do not allow switching of light by inducing a phase shift between the two interferometer arms. The throughput heavily depends on the laser misalignment.
- Single-core waveguides with a multi-core taper have a throughput which is actually lower than the throughput of a single-core waveguide *without* a taper.

- The throughput and hence, the photocurrent of multi-core waveguides can be influenced by deforming the waveguide by applying pressure onto it. The waveguide compression factor has to be rather large in order to guarantee a large relative photocurrent change for *any* lateral laser misalignment.
- Simulations of periodic refractive index variations due to a TPA writing process using a pulsed laser were inconclusive. The spatially fast refractive index variations might violate an approximation of the Beam Propagation Method.

A novel Eigenmode Decomposition Method has been presented, which is a very computationally efficient method for computing the throughput of a waveguide for a given input field. The mathematical framework of this method is based on a decomposition of the input field into one part which lies in the Hilbert space of waveguide eigenmodes, and another part which lies in the orthogonal complement of this space. The part in the eigenmode space is represented as a linear combination of waveguide eigenmodes and hence, has a throughput equal to one. The part in the orthogonal complement of the eigenmode space is orthogonal to *any* eigenmode and therefore has a throughput equal to zero. This decomposition delivers insight into the more general question of how light propagation in an optical waveguide works.

The software BEAMLAB has shown to be very capable of carrying out all of the above mentioned simulations.

- BEAMLABBPM implements a Finite Difference Alternate Direction Implicit Beam Propagation Method (FD-ADI-BPM). It uses some approximations in the derivation of the discretized wave equation which are irrelevant for most, but not all of the simulations in this work.
- BEAMLABEIG implements a waveguide eigenmode solver, also based on the Finite Difference method. It has been used to calculate the eigenmodes for the Eigenmode Decomposition Method.
- BEAMLABEDM implements the Eigenmode Decomposition Method. It allows to compute waveguide throughputs much faster than BEAMLABBPM and, more importantly, without the restrictions of the approximations of the BPM.

The simulation results indicate that there is potential for optimization of the multi-core waveguides investigated in this work. For example, the throughput would increase if the relative refractive index difference between waveguide core and cladding is increased by improving the ORMOCER[®] substrate material. By adjusting parameters like the number and spatial placement of the cores, the throughput could also be increased to some degree.

Appendix A

Multi-Core Waveguide Eigenmodes

Figure A.1 shows the *dispersion relation* $B(V)$ of the multi-core waveguide. In Figure A.2 the number of eigenmodes as a function of the normalized frequency (see Equation (4.25)) is depicted. The core radius a of the multi-core structure is defined as $a = r + w_{0,n} = 32.5 \mu\text{m}$, where the parameter values from Table 2.2 have been used.

Figures A.3–A.5 show the 51 eigenmodes of the multi-core waveguide from Section 2.2.1 for the wavelength $\lambda = 850 \text{ nm}$. According to Equation (4.25), this wavelength corresponds to a normalized frequency of $V = 22.98$. The eigenmodes in Figures A.3–A.5 are sorted by their effective refractive index n_{eff} in descending order.

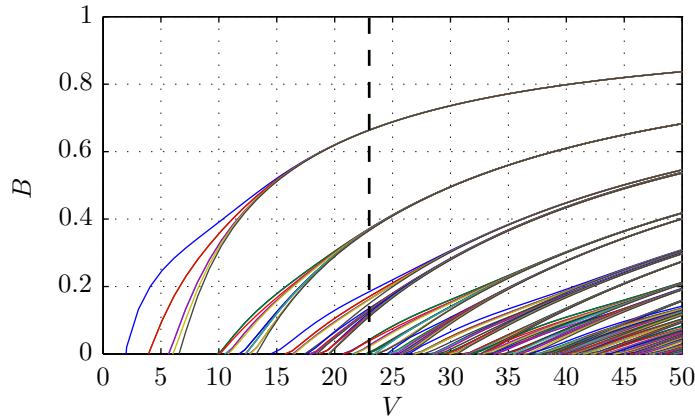


Figure A.1: Dispersion relation $B(V)$ of the multi-core waveguide. The dashed vertical line indicates the normalized frequency V corresponding to the wavelength $\lambda = 850 \text{ nm}$.

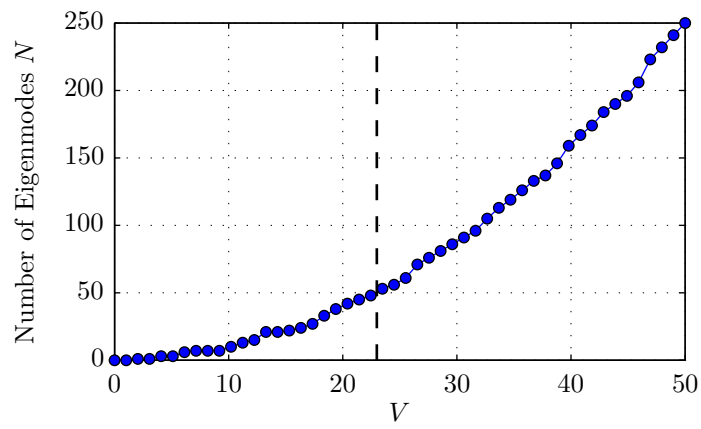


Figure A.2: Number of eigenmodes N vs. normalized frequency V of the multi-core waveguide. The dashed vertical line indicates the normalized frequency V corresponding to the wavelength $\lambda = 850$ nm.

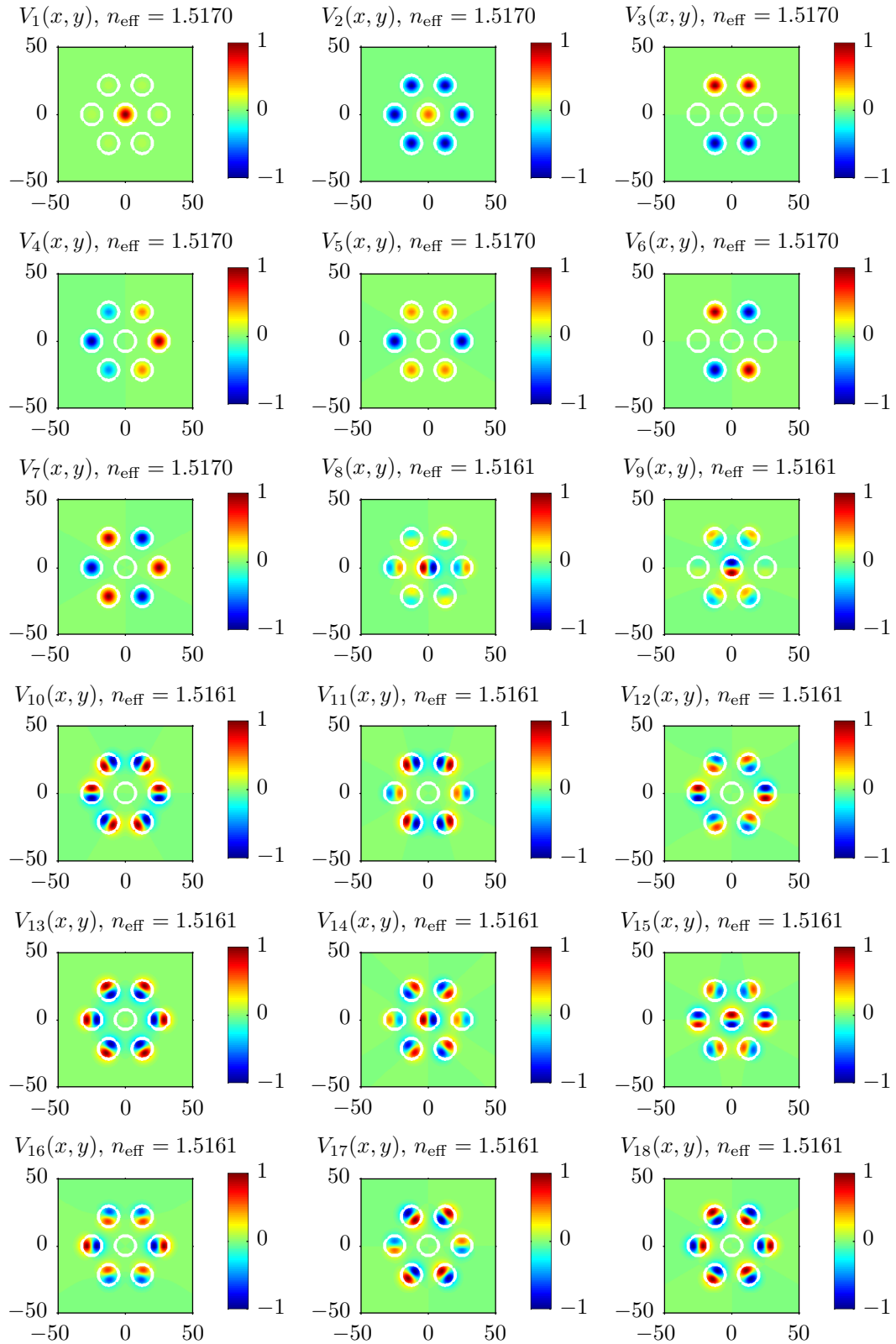


Figure A.3: Eigenmodes 1–18 of the multi-core waveguide. The abscissas and ordinates are all in μm and show x and y coordinates, respectively.

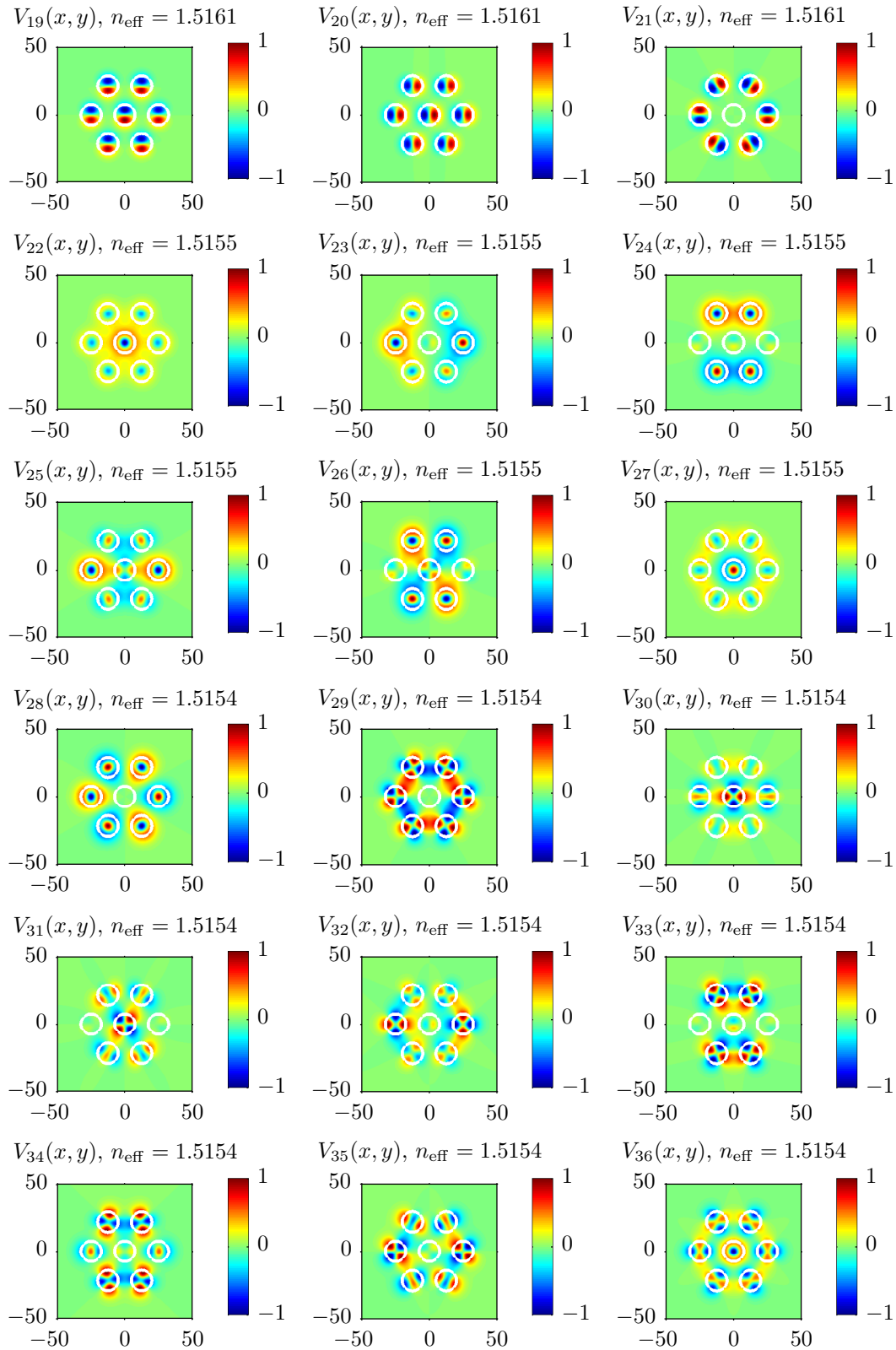


Figure A.4: Eigenmodes 19–36 of the multi-core waveguide. The abscissas and ordinates are all in μm and show x and y coordinates, respectively.

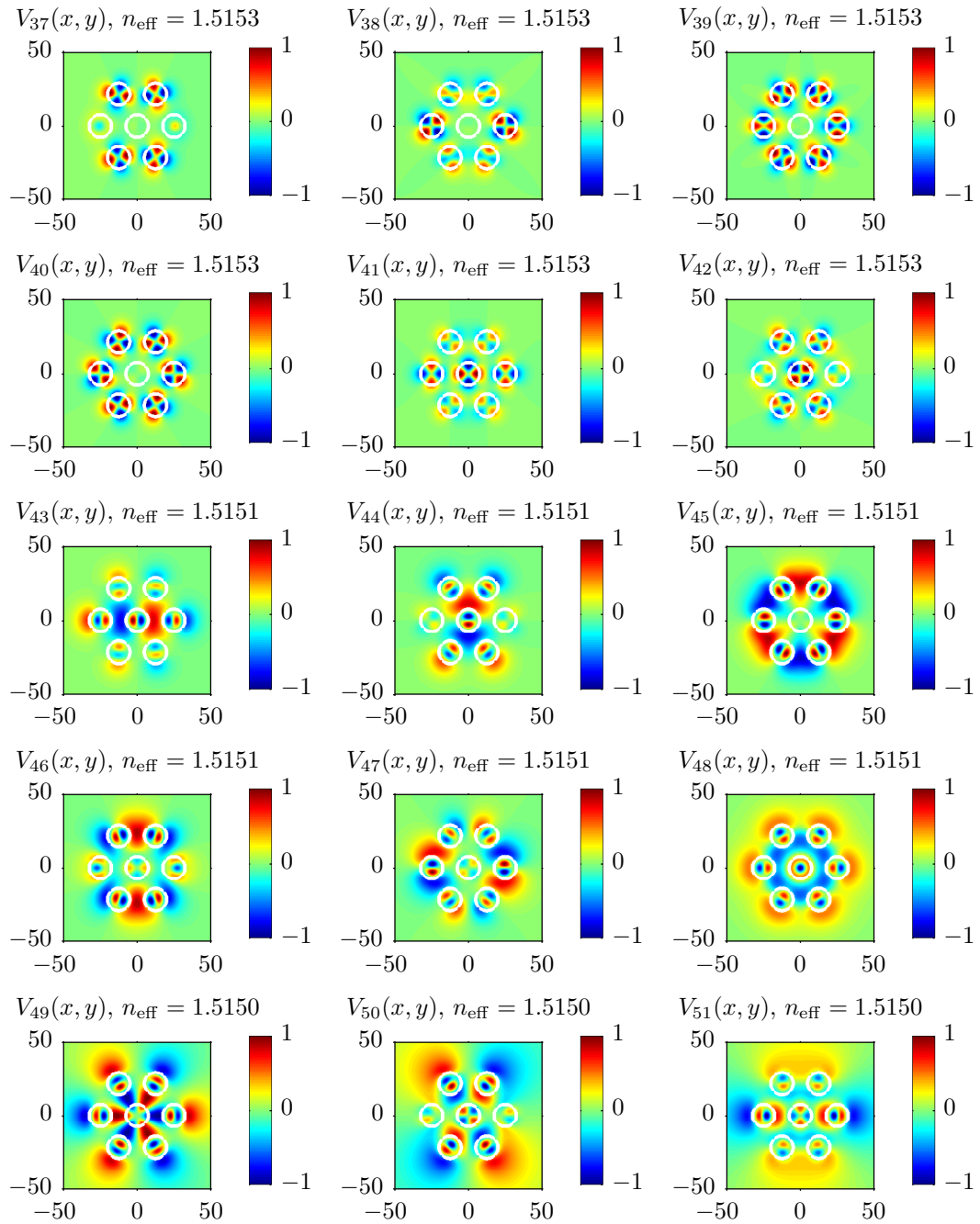


Figure A.5: Eigenmodes 37–51 of the multi-core waveguide. The abscissas and ordinates are all in μm and show x and y coordinates, respectively.

Appendix B

VCSEL Eigenmodes

Figure B.1 shows the normalized intensity distributions of the VCSEL eigenmodes from Equation (2.6). Here, the helical c polarization of the eigenmodes is shown since the intensity distribution of the weighted sum of c and s polarization with equal weights results in an intensity distribution which is azimuthally invariant. The intensity distributions of the s polarizations can be found simply by rotating the intensity distributions from Figure B.1 by $\pi/(2l)$ for $l > 0$ where l is the number of azimuthal zeros in the interval $0 \leq \varphi < \pi$ of mode LP_{lp} . It is evident that the intensity distributions are the same for c and s polarization for $l = 0$.

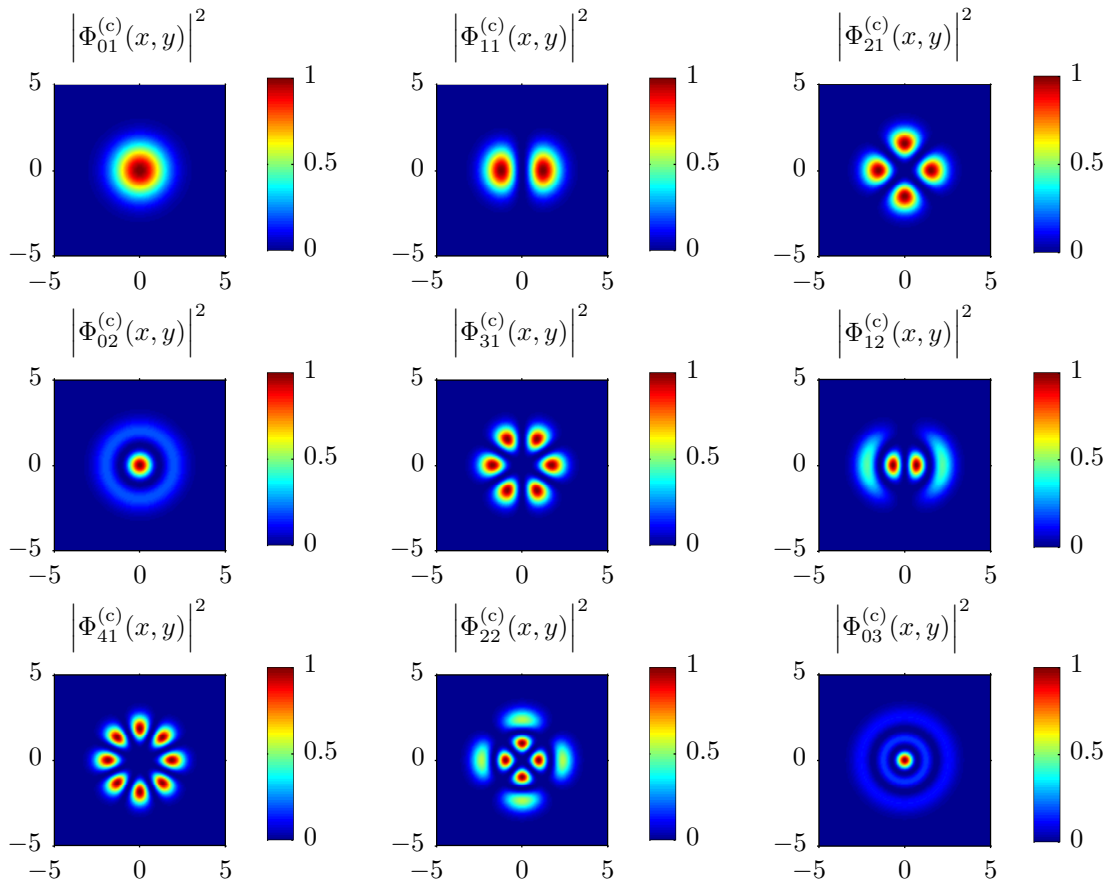


Figure B.1: VCSEL eigenmodes from Equation (2.6). The abscissas and ordinates are all in μm and show x and y coordinates, respectively.

Appendix C

BeamLab Examples

C.1 Beam Propagation Computation Using BeamLabBPM

In this example we will compute the light propagation of a Gaussian beam which couples into a circular step-index single-mode waveguide. The beam has an angle of $\theta_x = 5^\circ$ with respect to the z direction in the plane $y = 0$, the beam mode field radius is $w_0 = 5 \mu\text{m}$ and the beam offset with respect to the x direction at $z = 0$ is $x_{\text{offset}} = 5 \mu\text{m}$. The waveguide core radius is $a = 4.5 \mu\text{m}$ and the core and cladding refractive index are $n_1 = 1.455$ and $n_2 = 1.450$, respectively. The waveguide starts at $z = 100 \mu\text{m}$.

```
1 clear all;
2 close all;
3
4 %% Define general parameters
5 lambda = 850e-9; % wavelength
6 Mx = 129; % number of discretization points in x direction
7 My = Mx; % number of discretization points in y direction
8 dz = 1e-6; % discretization step size
9
10 %% Define mesh grid points
11 mesh_points.x = linspace(-20,20,Mx)*1e-6; % mesh grid points in x direction
12 mesh_points.y = linspace(-20,20,My)*1e-6; % mesh grid points in y direction
13 mesh_points.z = (0:dz/1e-6:2000)*1e-6; % mesh grid points in z direction
14
15 %% Define output "slices" of calculated field
16 compression.z = 1; % compression of slices.x and slices.y in z direction
17 slices.x = [];
18 slices.y = ceil(My/2);
19 slices.z = [];
20
21 %% Define x-y-grid
22 [X,Y] = ndgrid(mesh_points.x, mesh_points.y);
23
24 %% Define waveguide geometry
25 n1 = 1.455; % core refractive index
26 n2 = 1.45; % cladding refractive index
27 neff = n2; % reference index
28 a = 4.5e-6; % core radius
29
30 N_offset.z = 100e-6; % wavguide starts at z = N_offset.z
31
32 mesh_points.Nz = [0 N_offset.z]; % mesh grid points of refractive index
33                                     % in z direction
34 MN = length(mesh_points.Nz);
35
```

```

36 N = n2*ones(Mx,My,MN);
37 N2 = n2*ones(Mx,My);
38 N2((X.^2 + Y.^2) ≤ a^2) = n1; % circular step-index optical waveguide
39 N(:, :, 2) = N2;
40
41 %% Define input field
42 w0 = 5e-6; % mode field radius
43 A0 = 1; % amplitude
44 phi0_offset.x = 5e-6; % offset with respect to the x direction
45 phi0_offset.y = 0e-6; % offset with respect to the y direction
46 phi0_offset.z = 0e-6; % offset with respect to the z direction
47 phi0_theta.x = 5; % angle with respect to the x direction
48 phi0_theta.y = 0; % angle with respect to the y direction
49
50 phi0 = phi_gaussian(mesh_points, lambda, w0, A0, phi0_offset, phi0_theta);
51
52 %% Define BeamLabBPM options
53 index.power = (X.^2 + Y.^2) ≤ 20e-6; % define logical index matrix for
54                                     % area of power integral
55 options.mode = 'scalar'; % use scalar computation mode
56 options.discretization = 'equidistant'; % use equidistant discretization
57
58 %% Start actual computation
59 [phi_slices, ret_params] = beamlab.bpm3d_v62(lambda, neff, phi0, N, ...
60     mesh_points, phi0, slices, compression, index, options);
61
62 P = ret_params.power; % power in area defined by index.power
63
64 %% Plot output field slice
65 plot_slice(phi_slices.y, mesh_points, -40:10:0);
66 % Plot lines indicating the position of the waveguide
67 line([N_offset.z/1e-6, mesh_points.z(end)/1e-6], [a a]/1e-6, ...
68     'Color', 'white', 'LineStyle', '-', 'LineWidth', 1);
69 line([N_offset.z/1e-6, mesh_points.z(end)/1e-6], [-a a]/1e-6, ...
70     'Color', 'white', 'LineStyle', '-', 'LineWidth', 1);
71 line([N_offset.z/1e-6, N_offset.z/1e-6], [-a a]/1e-6, ...
72     'Color', 'white', 'LineStyle', '-', 'LineWidth', 1);
73
74 %% Plot power P in the waveguide vs. propagation distance z
75 figure;
76 plot(mesh_points.z/1e-6, P/P(1));
77 title('Power in the Waveguide');
78 xlabel('z/\mu m');
79 ylabel('P(z)/P(0)');
80 ylim([0 1]);
81 box on;
82 grid on;

```

Figure C.1 shows the first output plot this example, i.e. the spatial intensity distribution of the input beam propagating in the circular step-index waveguide. Figure C.2 shows the second output plot of this simulation, i.e. the power in a circular area of radius $20 \mu\text{m}$ as a function of the propagation distance z .

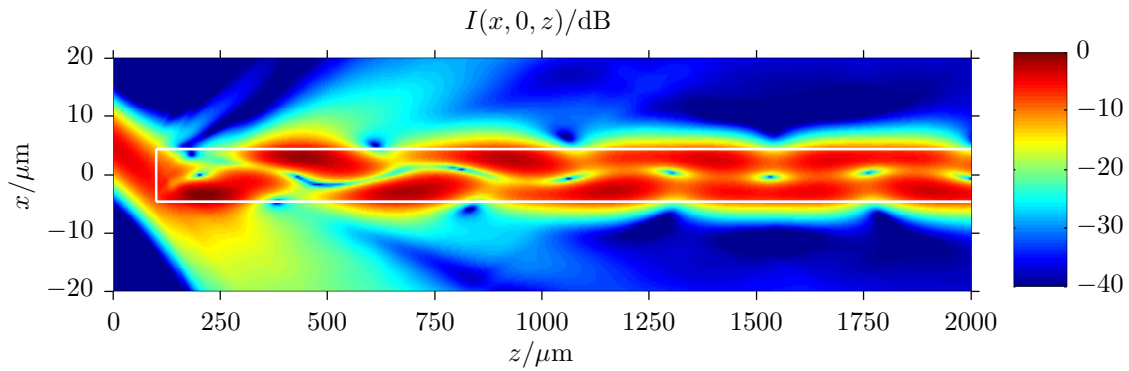


Figure C.1: First output plot of the BEAMLABBPM example showing the intensity I in the plane $y = 0$ of a beam propagating in a circular step-index waveguide.

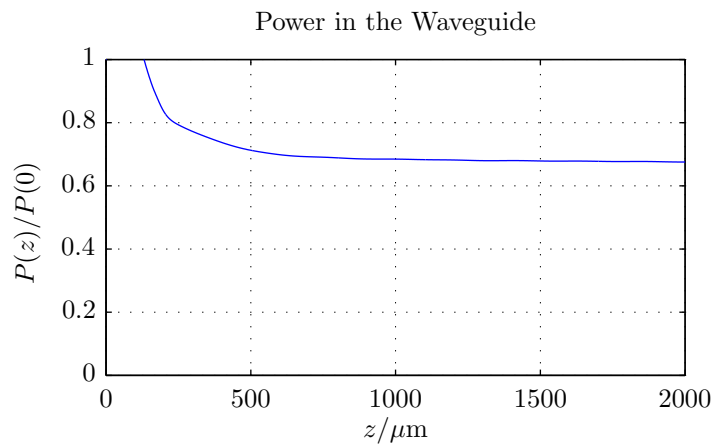


Figure C.2: Second output plot of the BEAMLABBPM example showing the power in a circular area of radius $20 \mu\text{m}$ vs. propagation distance z .

C.2 Eigenmode Computation Using BeamLabEIG

In this example we will compute and plot the eigenmodes as well as the dispersion relation $B(V)$ of a circular step-index waveguide. B is the normalized propagation constant defined in Equation (3.145) and V is the normalized frequency defined in Equation (4.25). The simulation parameters used are $a = 4.5 \mu\text{m}$ for the core radius, and $n_1 = 1.455$ and $n_2 = 1.450$ for core and cladding refractive index, respectively.

```

1 clear all;
2 close all;
3
4 %% Define general parameters
5 Mx = 129; % number of discretization points in x direction
6 My = Mx; % number of discretization points in y direction
7
8 %% Define mesh grid points
9 mesh_points.x = linspace(-10,10,Mx)*1e-6; % mesh grid points in x direction
10 mesh_points.y = linspace(-10,10,My)*1e-6; % mesh grid points in y direction
11
12 %% Define x-y-grid
13 [X,Y] = ndgrid(mesh_points.x, mesh_points.y);
14
15 %% Define waveguide geometry
16 n1 = 1.455; % core refractive index
17 n2 = 1.45; % cladding refractive index
18 a = 4.5e-6; % core radius
19
20 N = n2*ones(Mx,My);
21 N((X.^2 + Y.^2) <= a^2) = n1; % circular step-index optical waveguide
22
23 %% Define BeamLabEIG options
24 options.mode = 'scalar'; % use scalar computation mode
25 options.discretization = 'equidistant'; % use equidistant discretization
26
27 %% Compute eigenmodes for V=5
28 k = 50; % maximum number of eigenmodes to be computed
29 V = 5; % normalized frequency
30 lambda = (2*pi*a*sqrt(n1^2-n2^2))./V;
31 [phi_eigs, neff] = beamlab_eig_v11(lambda, N, mesh_points, k, options);
32
33 mode_count = sum(neff > n2); % number of eigenmodes
34 B = (real(neff.')-n2)/(n1-n2); % normalized propagation constant
35
36 %% Save workspace variables
37 % The eigenmodes will be used in the BeamLabEDM example the calculate the
38 % throughput using the Eigenmode Decomposition Method
39 filename = 'beamlab_eig_demo.mat';
40 save(filename, 'phi_eigs', 'mesh_points', 'neff', 'mode_count', 'lambda');
41 disp_msg(['Results saved in file: ' filename]);
42
43 %% Plot eigenmodes
44 subplot_dim = [3 2]; % rows and columns of subplots
45
46 plot_eigenmodes(X, Y, phi_eigs, neff, mode_count, subplot_dim, ...
47     [1 1.5]*500, B);
48
49 %% Define BeamLabEIG options
50 options.mode = 'scalar'; % use scalar computation mode
51 options.discretization = 'equidistant'; % use equidistant discretization
52 options.display = 'none'; % suppress command line output
53

```



```

54 %% Compute dispersion relation B(V)
55 k = 30; % maximum number of eigenmodes to be computed
56 V_vec = linspace(0,10,50); % vector of normalized frequencies
57 lambda_vec = (2*pi*a*sqrt(n1^2-n2^2))./V_vec;
58
59 neff_matrix = zeros(k, length(lambda_vec)); % allocate matrix for neff
60 % values
61
62 % If you own a license of Matlab Parallel Computing Toolbox and/or Matlab
63 % Distributed Computing Server, this for loop can be replaced by a parfor
64 % loop to enable parallel computation of independent loop iterations.
65 for i = 1:length(lambda_vec)
66     disp_msg(['Iteration: ' num2str(i) '/' num2str(length(lambda_vec))]);
67     lambda = lambda_vec(i);
68     [phi_eigs, neff] = beamlab_eig.v11(lambda, N, mesh.points, k, options);
69     neff_matrix(:,i) = neff;
70 end
71
72 B = (real(neff_matrix.')-n2)/(n1-n2); % normalized propagation constant
73
74 %% Plot dispersion relation diagram
75 figure;
76 plot(V_vec,B);
77 xlim([min(V_vec) max(V_vec)]);
78 ylim([0 1]);
79 title('Dispersion Relation of a Circular Step-Index Waveguide');
80 xlabel('V');
81 ylabel('B');

```

Figure C.3 shows the first output plot of this simulation. Here, the six eigenmodes of the circular step-index waveguide at $V = 5$, which relates to $\lambda = 605.8$ nm by Equation (4.25), are shown. These eigenmodes $\Phi_1, \Phi_2, \dots, \Phi_6$ are the well-known Bessel modes $LP_{01}, LP_{11}, LP_{11}, LP_{21}, LP_{21},$ and LP_{02} , respectively. It can be seen that Φ_2 and Φ_3 and also Φ_4 and Φ_5 are degenerated, i.e. they have the same normalized propagation constant B since they are just rotated versions of each other.

Figure C.4 shows the second output plot of this example, i.e. the dispersion relation $B(V)$. The results obtained from the simulation using BEAMLABELIG match the corresponding analytical results very good (see [8]).

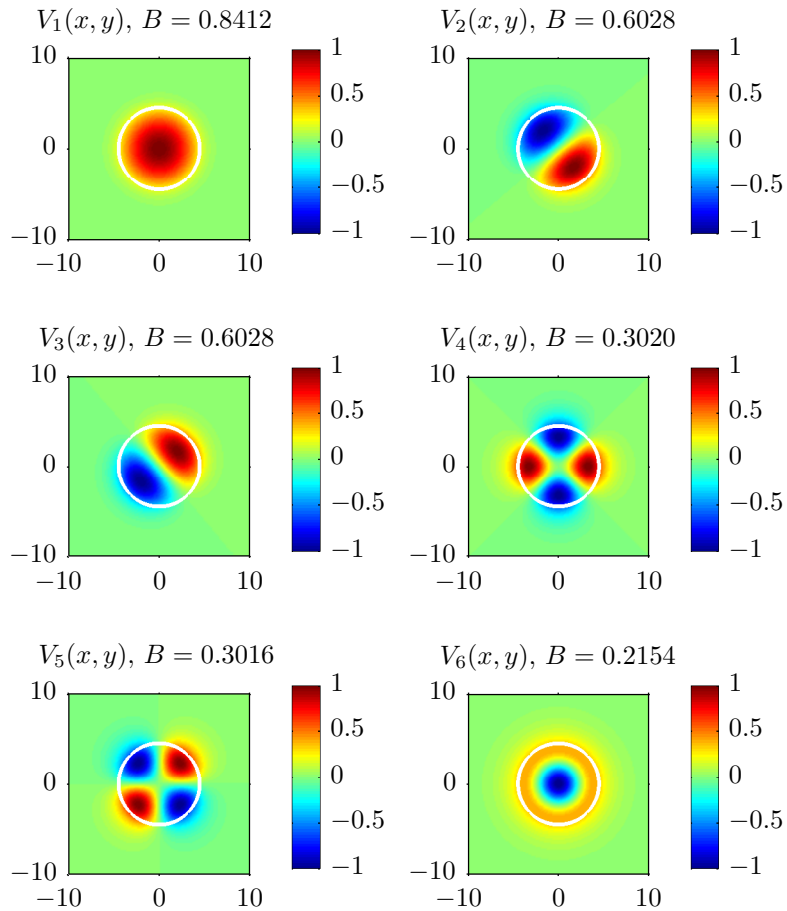


Figure C.3: First output plot of the BEAMLABELIG example showing the six eigenmodes V_1, \dots, V_6 of the circular step-index waveguides at $V = 5$. The abscissas and ordinates are all in μm and show x and y coordinates, respectively.

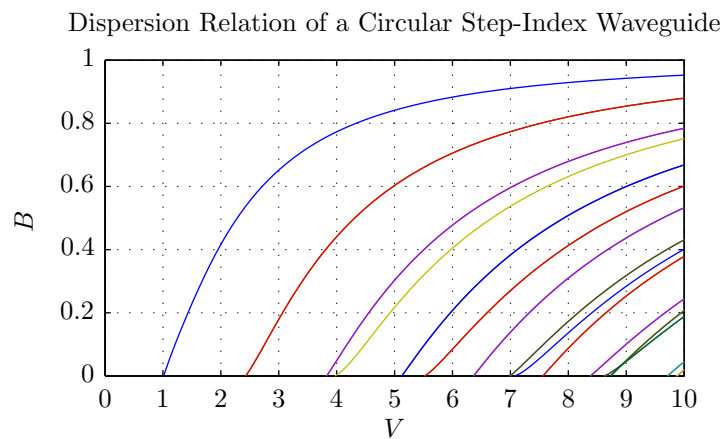


Figure C.4: Second output plot of the BEAMLABELIG example showing the dispersion relation $B(V)$ of a circular step-index waveguide.

C.3 Throughput Computation Using BeamLabEDM

In this example the throughput of the circular step-index waveguide from Section C.2 will be investigated in detail using the Eigenmode Decomposition Method from BEAMLABEDM.

The input field Φ_0 is a Gaussian LP_{01} field, as defined in Section 2.3, with $w_0 = 2.10 \mu\text{m}$ and a lateral offset of $x_{\text{offset}} = 2.5 \mu\text{m}$. The waveguide has a circular step-index refractive index profile with $a = 4.5 \mu\text{m}$ core radius and $n_1 = 1.455$ and $n_2 = 1.450$ core and cladding refractive index, respectively. The normalized frequency is $V = 5$ which results in the 6 different Eigenmodes V_1, \dots, V_6 from Figure C.3.

```

1 clear all;
2 close all;
3
4 %% Load eigenmodes from the BeamLabEIG example
5 load 'beamlab.eig_demo.mat';
6
7 %% Define input field
8 w0 = 2.098e-6;
9 A0 = 1;
10 phi0_offset.x = 4.5e-6;
11 phi0_offset.y = 0e-6;
12 phi0_offset.z = 0e-6;
13 phi0_alpha.x = 0;
14 phi0_alpha.y = 0;
15
16 phi0 = phi_gaussian(mesh_points, lambda, w0, A0, phi0_offset, phi0_alpha);
17
18 %% Compute overlap integrals and inner products with all eigenmodes, as
19 %% well as the throughput of phi0
20 [throughput_phi0, overlap_vec_phi0, inner_product_vec_phi0] = ...
21     beamlab_edm.v11(phi0, phi_eigs, mode_count)
22
23 phi_H = zeros(size(phi0));
24 for k = 1:mode_count
25     phi_H(:, :, k) = phi_eigs(:, :, k) * inner_product_vec_phi0(k);
26 end
27 phi_H = sum(phi_H, 3);
28 phi_H_comp = phi0 - phi_H;
29
30 %% Compute overlap integrals and inner products with all eigenmodes, as
31 %% well as the throughput of phi_H
32 [throughput_phi_H, overlap_vec_phi_H, inner_product_vec_phi_H] = ...
33     beamlab_edm.v11(phi_H, phi_eigs, mode_count)
34
35 %% Compute overlap integrals and inner products with all eigenmodes as
36 %% well as the throughput of phi_H_comp
37 [throughput_phi_H_comp, overlap_vec_phi_H_comp, ...
38     inner_product_vec_phi_H_comp] = ...
39     beamlab_edm.v11(phi_H_comp, phi_eigs, mode_count)

```

Bibliography

- [1] S. Uhlig, L. Fröhlich, M. Chen, N. Arndt-Staufenbiel, G. Lang, H. Schröder, R. Houbertz, M. Popall, and M. Robertsson, “Polymer optical interconnects - a scalable large-area panel processing approach,” *IEEE Transactions on Advanced Packaging*, vol. 29, 2006.
- [2] V. Schmidt, L. Kuna, V. Satzinger, R. Houbertz, G. Jakopic, and G. Leising, “Application of two-photon 3D lithography for the fabrication of embedded ORMOCER waveguides,” *Proceedings of SPIE*, vol. 6476, 2007.
- [3] J. Reitterer. <http://www.beamlab.net/>, June 2010.
- [4] M. X. Jungo, “Spatiotemporal VCSEL model for advanced simulations of optical links,” *Series in Quantum Electronics*, vol. 30, 2003.
- [5] H. Li and K. Iga, *Vertical-Cavity Surface-Emitting Laser Devices*. Springer, 2003.
- [6] F. Mederer, *Optische Datenübertragung mit Vertikal-Laserdioden im Wellenlängenbereich von 650 bis 1550 nm*. Cuvillier Verlag Göttingen, 2004.
- [7] S. Schwarz, “Impact of waveguide input coupling on vertical cavity surface emitting laser diodes,” Master’s thesis, Technische Universität Wien, 2009.
- [8] G. Reider, *Photonik — Eine Einführung in die Grundlagen*. Springer, 2005.
- [9] K. Kawano and T. Kitoh, *Introduction to Optical Waveguide Analysis*. John Wiley & Sons, Inc., 2001.
- [10] M. D. Feit and J. A. Freck, “Light propagation in graded-index optical fibers,” *Applied Optics*, vol. 17, pp. 3990–3998, 1978.
- [11] Y. Chung and N. Dagli, “An assessment of Finite Difference Beam Propagation Method,” *IEEE Journal of Quantum Electronics*, vol. 26, pp. 1335–1339, 1990.
- [12] M. Koshihara and Y. Tsuji, “A wide-angle Finite Element Beam Propagation Method,” *IEEE Photonics Technology Letters*, vol. 8, pp. 1208–1210, 1996.
- [13] G. R. Hadley, “Multistep method for wide-angle beam propagation,” *Optics Letters*, vol. 17, pp. 1743–1745, 1992.
- [14] A. Prechtel, “Elektrodynamik.” Lecture Notes, 2005.
- [15] G. Fasching, *Werkstoffe für die Elektrotechnik — Mikrophysik, Struktur, Eigenschaften*. Springer, 2005.
- [16] W. Y. Yang, W. Cao, T.-S. Chung, and J. Morris, *Applied Numerical Methods Using Matlab*. John Wiley & Sons, Inc., 2005.

- [17] G. R. Hadley, “Transparent Boundary Condition for the Beam Propagation Method,” *IEEE Journal of Quantum Electronics*, vol. 28, 1992.
- [18] D. Yevick and B. Hermansson, “New formulations of the Matrix Beam Propagation Method: Application to rib waveguides,” *IEEE Journal of Quantum Electronics*, vol. 25, pp. 221–229, 1989.
- [19] F. Schmidt and P. Deuffhard, “Discrete Transparent Boundary Conditions for the numerical solution of Fresnel’s equation,” *Computers & Mathematics with Applications*, vol. 29, pp. 53–76, 1995.
- [20] J. Yamauchi, T. Ando, and H. Nakano, “Beam-Propagation analysis of optical fibres by Alternating Direction Implicit method,” *Electronics Letters*, vol. 27, pp. 1663–1665, 1991.
- [21] F. Hlawatsch, “Modulation and detection techniques.” Lecture Notes, 2008.
- [22] S. Jüngling, “A study and optimization of eigenmode calculations using the Imaginary-distance Beam-Propagation Method,” *IEEE Journal of Quantum Electronics*, vol. 30, 1994.
- [23] W. Leeb, “Optische Nachrichtentechnik.” Lecture Notes, 2007.
- [24] A. W. Snyder and J. D. Love, *Optical Waveguide Theory*. London: Chapman & Hall, 1991.
- [25] G. Schmid, “Rechnerische Analyse der Eigenschaften von Polymerlichtwellenleitern,” Master’s thesis, Technische Universität Wien, 2005.
- [26] F. Hlawatsch, “Processing of stochastic signals.” Lecture Notes, 2008.